Dielectric and Piezoelectric Properties of Reduced-Graphite-Oxide/Poly(vinylidene fluoride) Nanocomposite and its Related Devices

Ye Zhang

Submitted in partial fulfilment of the requirements of

the Degree of Doctor of Philosophy

School of Metallurgy and Materials,

University of Birmingham

Birmingham, United Kingdom

September 2018

UNIVERSITY OF
BIRMINGHAM

University of Birmingham Research Archive

e-theses repository

This unpublished thesis/dissertation is copyright of the author and/or third parties. The intellectual property rights of the author or third parties in respect of this work are as defined by The Copyright Designs and Patents Act 1988 or as modified by any successor legislation.

Any use made of information contained in this thesis/dissertation must be in accordance with that legislation and must be properly acknowledged. Further distribution or reproduction in any format is prohibited without the permission of the copyright holder.

Declaration

I, Ye Zhang, confirm that the research included within this thesis is my own work or that where it has been carried out in collaboration with, or supported by others, that this is duly acknowledged below and my contribution indicated. Previously published material is also acknowledged below.

I attest that I have exercised reasonable care to ensure that the work is original, and does not to the best of my knowledge break any UK law, infringe any third party's copyright or other Intellectual Property Right, or contain any confidential material.

I accept that the College has the right to use plagiarism detection software to check the electronic version of the thesis.

I confirm that this thesis has not been previously submitted for the award of a degree by this or any other university.

The copyright of this thesis rests with the author and no quotation from it or information derived from it may be published without the prior written consent of the author.

Ye Zhang

09/2018

Acknowledgement

Firstly, I would like to thank my supervisor Professor Tim Button for guiding me through my PhD project in the past four years. Tim has always been nice and patient to discuss with me on my projects and gave me caring support when I got difficulties. Secondly, I would like to thank my second supervisors Dr. Yun Jiang and Dr. Daniel Rodriguez Sanmartin, for their kindly help and support. And I also want to express my appreciation to Mr. Carl Meggs, who assisted me a lot in the lab. Furthermore, I would like to thank my colleagues and friends for their help and support in my research. I would like to thank the Chinese Scholarship Council for providing me with financial support for my PhD program.

My greatest thanks go to my grandparents Ms. Shuhe Lin, Mr Chunhai Hao, my parents Ms. Yueguang Hao and Mr. Beicheng Zhang for their all-time support in my life and career. Special thanks go to my wife Ms. Yaqiong Wang, who is a studying PhD in Queen Mary, University of London, not only for her understanding, love and care, but also for being the most important person in my life.

Abstract

There is an increasing demand of smart devices with light-weight, flexible, and scalable nature. Functional polymers and the related composites are suitable candidates that can fulfil the requirements in flexible device applications. Poly(vinylidene fluoride) (PVDF) is one kind of the functional polymers possessing a large dielectric strength as well as a permanent molecular electrical dipole (for all-trans and semi-trans conformation). Hence, it has the potential to be applied to capacitive energy storage devices as well as piezoelectric sensors and actuators. One route to improve the dielectric and piezoelectric of the PVDF polymer is to hybridize the pure polymer with an inorganic inclusion phase, usually submicron-sized ferroelectric ceramic particles or nano-sized low-dimensional carbons. As these composites always suffer poor dispersion and exhibit high leakage, majority of attentions have been focused on fabrication-structure relation to solve the processing issues. In this project, we focused more on the structure-property relation of the PVDF related composites. The aim of this project is to give deeper understandings in the potential and limitations for PVDF related composites and provide a guidance on optimizing the dielectric and piezoelectric properties these composites for flexible devices.

The reduced-graphite-oxide (rGO) was chosen as the inclusion particles, and the rGO/PVDF nanocomposites were fabricated via an in-situ thermal reduction method. To start, we studied the role of rGO on the dielectric properties of the nanocomposites. With a conductor-insulator heterostructure model, we found an ‘expanding’ effect of rGO particles that improves the system dielectric response. We also found a pseudo-leakage in nanocomposites due to charge carrier recombination. These findings established a quantitative method to evaluate the energy storage performance for capacitors with composite dielectrics, which fits well with the experimental data.

We also studied the molecular and crystal structure of the PVDF polymer with respect to the rGO addition. It was found that the addition of rGO can induce the nucleating of a thermodynamically instable β phase, which makes the nanocomposites ferroelectric. This β phase formation was found to occur in the melting-recrystallization procedure, which is accompanied by the thermal reduction of rGO. Based on the experimental data, a β phase formation mechanism was proposed, which suggests the nanocomposites is piezoelectric with PVDF molecular dipole mirrored by the rGO plane forming local bimorph structure. According to this, two types of piezoelectric devices with the rGO/PVDF nanocomposites were fabricated and tested, and the results are in good agreement with the models proposed in this research.

Table of Contents

Declaration i

Acknowledgement ii

Abstract iii

Table of Contents v

List of Figures ix

Nomenclature and Acronyms xv

Chapter 1 Introduction 1

Chapter 2 Fundamentals of Ferroelectricity 4

- 2.1 Non-centrosymmetric Crystals 4
- 2.2 Piezoelectric Materials 5
- 2.3 Pyroelectric Materials 8
- 2.4 Ferroelectric Materials 10

Chapter 3 Poly(vinylidene fluoride) Ferroelectric Polymers 16

- 3.1 Conformational and Crystal Structure 16
- 3.2 Ferroelectricity in PVDF Polymers 22
- 3.3 PVDF Composites with Inorganic Inclusions 23
- 3.4 β-Phase Formation in PVDF Composites 31

Chapter 4 Aim and Objectives 35

Chapter 5 Experimental and Measurement Methods 36

5.1 Solution-casting of Pure PVDF film 36

5.2 Solution-casting of the GO/PVDF Nanocomposites 36

5.3 In-situ Thermal Reduction of the GO Particles 38

5.4 In-situ Thermal Reduction of the GO/PVDF Nanocomposites 38

5.5 Lapping and Electrode-Sputtering the rGO/PVDF Nanocomposites 39

5.6 Measurement Techniques 40

Chapter 6 Modelling the Dielectric Behaviour of a Composite 45

6.1 Introduction 45

6.2 Schottky Junction Theory and Device Capacitance 45

6.3 Modelling of the rGO/PVDF heterointerface 49

6.4 Morphology and Structure of rGO and rGO/PVDF Nanocomposites 55

6.5 I-V Characteristics of the rGO/PVDF Nanocomposites 59

6.6 Equivalent Circuit of the rGO/PVDF Nanocomposites 62

6.7 Summary 65

Chapter 7 Dielectric Behaviour of the rGO/PVDF Nanocomposites 66

7.1 Introduction 66

7.2 Dielectric Responses of the rGO/PVDF Nanocomposites 66

7.3 Energy Storage Performances of the rGO/PVDF Nanocomposites 70

7.4 Modifying the rGO/PVDF Heterojunction for Achieving Large Discharge Energy Density 75

7.5 Relation Between Dielectric Permittivity and Discharge Energy Density 78

7.6 Summary 80

Chapter 8 β-Phase Formation in the rGO/PVDF Nanocomposites 82

8.1 Introduction 82

8.2 Molecular Conformation in the rGO/PVDF Nanocomposites 83

8.3 Crystalline Structure of the rGO/PVDF Nanocomposites 88

8.4 Morphology and Local Piezoelectric Response of the rGO/PVDF Nanocomposites 93

8.5 Formation Mechanism of β Phase in the rGO/PVDF Nanocomposites 94

8.6 Summary 98

Chapter 9 rGO/PVDF Nanocomposite Related Devices 100

9.1 Introduction 100

9.2 Actuator Assembly and Measurement Configuration 100

9.3 Vibrational Characteristics of the Nanocomposite 104

9.4 Energy Harvester Assembly and Measurement Configuration 106

9.5 Output Characteristics of the Energy Harvesters 112

9.6 Summary 116

Chapter 10 Conclusion and future work 118

10.1 Conclusion 118

10.2 Future work 121

Reference 123

Publications 131

Appendix 132

List of Figures

Figure 2.1 The relationship of ferroelectric, pyroelectric and piezoelectric materials 5

Figure 2.2 Crystal structure of ZnO showing an unswitchable dipole moment due to alternating Zn^{2+} (black sphere) and O^{2-} (grey sphere) planes[1] 7

Figure 2.3 Illustration of the pyroelectric effect. An increase in temperature T reduces the spontaneous polarization Ps causing change in surface charge. This will induce a current flow to composite the change in surface charge.[12] 10

Figure 2.4 Schematic view of the structure of the different phases of $BaTiO_3$. The Ba^{2+} ions (large sphere) are located at the corners, the Ti^{4+} ions (medium sphere) at the centre, and the O^{2-} (small sphere) ions at the face centres. The arrows show the polar direction along the cubic [001] direction for the tetragonal phase, the [011] direction for the orthorhombic phase, and the [111] direction for the rhombohedral phase.[16] 12

Figure 2.5 P-E hysteresis loop parameters for ferroelectric material[18] 13

Figure 2.6 Electric displacement-electric field (D-E) loop measurement of NKN850 ceramics at 1Hz and 25°C. (a) Electric field versus time and current versus time (b) current-electric field (I-E) hysteresis loop, (c) electric displacement-electric field (D-E) loop.[19] 15

Figure 3.1 Molecular packing and crystal structure. (a), (b), Schematic packing of two polymer chains with the TGT**G** configuration in the unit cell of the α-phase and the δ-phase. The symbols present the in- and out-of-plane components of the dipole moment. In the α-phase all contributions cancel out. In the δ-phase the in-plane components cancel out but the out-of-plane ones yield a net microscopic dipole moment. (c), (d), The crystal structures and molecular packing of α-PVDF and δ-PVDF viewed along the c axis. The polymer chain is projected onto the ab-plane. (e), (f), Crystal structure of α-

PVDF and δ-PVDF viewed along the a axis. The drawn inner lines represent the unit cells. Grey circles represent carbon atoms, red circles fluorine atoms and blue circles hydrogen atoms[25] 18

Figure 3.2 Comparison of the unit cell of the (a) α phase and (b) β phases. The yellow sphere is the carbon, the red sphere is fluorine, and the white sphere is hydrogen, (c) and (d) are the molecular structure of α phase and β phase.[28] 19

Figure 3.3 Molecular conformation and chain packing for γ-PVDF[30]....................... 20

Figure 3.4 Relation between PVDF phase and processing conditions, DMA is short for dimethylacetamide while HMPTA is short for hexamethylphosphoramide [33] 22

Figure 3.5 Schematic illustration for the preparation of fluoro-polymer@$BaTiO_3$ nanoparticles and P(VDF-HFP) nanocomposite films[48] 25

Figure 3.6 (a) Image of the graphene oxide and nanocomposite: (a) the in situ reduced process for the single layer reduced-graphene oxide nanocomposite, (b) digital image of graphene oxide and in situ reduced-graphene oxide nanocomposite[57] 26

Figure 3.7 A metal electrode-dielectric interface showing (a), positive metal cores; (b), the outer electron cloud of the metal; (c), the structured inner Helmholtz layer of molecules and ions; (d), the outer Helmholtz layer and (e), the Gouy-Chapman diffuse space charge layer. The arrow indicate the orientation of polar molecules, and the molecules at the inner Helmholtz layer is highly ordered compared to those at the diffusion layer. [63].. 30

Figure 3.8 Finite element model of two phase composites with varying volume fraction of the conducting phase. Upper images show example random distributions of the conductor (gray) in a dielectric matrix (cyan), and lower images are corresponding contour plots after application of a normalized external electric field ($E_{applied}$=1). For a filler-free matrix, E_{local}=1 at all locations.[66] 31

Figure 3.9 Simulation model describing (a), (b) TGT$\bar{G}$ and (c), (d) TTTT chains absorbed on the armchair CNT tube, (e), (f) TGT$\bar{G}$ and (g), (h) TTTT chains absorbed on the zig-zag CNT tube[71] 33

Figure 3.10 Schematic representation of the interaction between $CoFe_2O_4$ nanoparticles and PVDF chains in the nanocomposite: the partially positive C–H bonds of the polymer are attracted by the negatively charged ferrite surface due to the static electric force. This leads to the all-trans conformation of the polymer phase[67] 34

Figure 5.1 Photograph comparing the dispersity of (a) GO and (b) xGnP in DMF solvents after sonication for 12h and 4 days of sedimentation 38

Figure 5.2 Photograph comparing the (A) PVDF film annealed at 200°C for 1h, (B) GO/PVDF film annealed at 100°C for 1h and (C) rGO/PVDF film annealed at 200°C for 1h 39

Figure 5.3 The route of IR beam in ATR-IR spectroscopy[78] 41

Figure 5.4 Illustration of the AFM/PFM method, with the sample deforms to respond to the applied voltage [79,80] 43

Figure 6.1 Electrical structure of a metal and a semiconductor (a) before contact and (b) after contact 47

Figure 6.2 (a) a diode model resembles a conductor/insulator type composite and (b) illustration for the effective expansion of composite system electrode by the addition of inclusion particles 51

Figure 6.3 Illustration of carrier recombination induced pseudo-leakage. 54

Figure 6.4 (a) X-ray diffractions for raw graphite and graphite-oxide prepared via Harmmer's method, and Morphology of (b) GO particles and (c) rGO particles reduced at 200°C for 1h in N_2 atmosphere 56

Figure 6.5 ATR-IR spectra for GO and rGO particles reduced at 200°C for 1h. 58

Figure 6.6 (a) SEM image of (a) as-casted GO/PVDF nanocomposites, (b) rGO/PVDF nanocomposites reduced at 200°C for 1h, and (c) pure PVDF annealed at 200°C for 1h. 59

Figure 6.7 I-V curve of 50μm rGO/PVDF nanocomposites coated with φ1mm chrome/gold electrode with different rGO content, in comparison with a pure PVDF, the insert figure shows the fitted results of I_0 and R_s 62

Figure 6.8 Nyquist plot of pure PVDF and rGO/PVDF nanocomposites, and their corresponding equivalent circuits 64

Figure 7.1 Frequency domain of (a) relative dielectric permittivity and (b) tanδ of 0.015-rGO-PVDF nanocomposites reduced at the temperature range from 100°C to 200°C for 1h 68

Figure 7.2 Frequency domain of (a) relative dielectric permittivity and (b) tanδ of rGO-PVDF nanocomposites reduced at 200°C for 1h 70

Figure 7.3 (a) discharging energy density J_d, (b) dielectric strength, and (c) efficiency η vs. field strength E for nanocomposites reduced at 200°C with varies of rGO content . 73

Figure 7.4 (a) D-E loops of 1.5-rGO@200 showing field-gated leakage and carrier recombination induced overcharging effect, and (b) band distortion between rGO particles illustrating the kinetics of carrier recombination 75

Figure 7.5 D-E hysteresis loops measured at 50MV/m at 10Hz for 1.5-rGO nanocomposites reduced in the temperature range between 100°C and 160°C 76

Figure 7.6 Effect of reduction temperature on the (a) dielectric strength, (b) discharging energy density J_d and (c) efficiency η of 0.015-rGO 78

Figure 7.7 Plots of discrete efficiency-charge displacement pairs measured from both pure PVDF and nanocomposite devices with varies reduction temperature and rGO content, the solid curve is the fitting result of the PVDF device, which fits well with the nanocomposites data, insert figure compares the experimental and calculated discharge energy density for two nanocomposite devices. 80

Figure 8.1 ATR-IR spectra of pure PVDF and rGO/PVDF nanocomposites 84

Figure 8.2 ATR-IR spectra comparing pure PVDF and rGO/PVDF nanocomposites at annealing temperatures ranging from 100°C to 200°C, with IR wavenumber between (a) 775cm^{-1} to 950cm^{-1}, and (b) 975cm^{-1} to 1350cm^{-1}........ 86

Figure 8.3 Dielectric permittivity vs. temperature plots for an as-casted 1.5-rGO and an as-casted pure PVDF........ 87

Figure 8.4 XRD spectra for PVDF and nanocomposites annealed at 200°C, the peaks marked by * is assigned to the substrate 89

Figure 8.5 Fitting curves with Lorenz peak function for (a) pure PVDF and (b) to (e) the nanocomposites reduced at 200°C 90

Figure 8.6 (a) content of β(110)/(200) and α(100) in the crystalline forms, (b) content of α(100) in the α phase and its FWHM changes with respect to the rGO volume fraction, and (c) illustration of the β(110)/α(100) stack structure in the nanocomposite sample.. 92

Figure 8.7 AFM images for (a) 1.0-rGO@200 and (b) pure PVDF indicate the nanocomposite possess rougher surface of agglomerated spherulites, PFM images for (c) 1.0-rGO@200 and (d) pure PVDF show cross-talk signal from morphology fluctuation, therefore we applied a -30V to 30V DC sweep to individual points to test the local electromechanical response, which are plotted in (e) to (g)... 94

Figure 8.8 (a) Comparison of the homogeneous nucleation (N(homo)) in pure PVDF and heterogeneous nucleation (N(hetero)) in the nanocomposite, (b) β phase formation due to TTTT molecule absorption and packaging at the rGO surface forming electrical double layer structure in the PVDF melt, assuming rGO is positively charged, the build-in field of PVDF dipole (indicated as an arrow) will counter-balance the static field of the rGO surface charge and (c) illustration of symmetrical PVDF dipole (white arrow) on the rGO (black line) surface forming a self-bimorph in the nanocomposite 98

Figure 9.1 (a) Vibration regime of a bi-clamped actuator device with respect to the electric field and (b) the vibration measurement configuration 103

Figure 9.2 Strain responses of BCAs assembled with (a) commercial PVDF film and (b) 0.015-rGO@200 nanocomposite operating at 100V/mm 20kHz 105

Figure 9.3 (a) Structure of a cantilever type energy harvester with rGO/PVDF nanocomposite and (b) the voltage output measurement configuration 108

Figure 9.4 Voltage output of a single-end-clamped energy harvester driven by finger tapping under (a) forward connection and (b) reverse connection 110

Figure 9.5 Relation between cantilever shape and the voltage output for the energy harvester with 1.5-rGO@200 111

Figure 9.6 Open circuit voltage output vs. load mass for 1.5-rGO-TCEH 112

Figure 9.7 Illustration of the internal screening effect in a capacitive device. 116

Nomenclature and Acronyms

$\tan\delta$	dissipation factor
Φ_b	Schottky barrier
ψ	Fermi level equalization energy
ε_0	vacuum dielectric permittivity
ε	dielectric permittivity
ε_r	relative dielectric permittivity
η	energy efficiency
θ	angle
κ	Debye-Huckel parameter
λ	wavelength
ν	magnification coefficient
ζ	damping ratio
σ	charge density
τ	relaxation time
φ	surface potential
ω	angular frequency
A	junction area
A^*	Richardson constant
C	capacitance
D	electrical displacement
E	electric field
E^*	local electric field
F	texture quality

G	Gibbs free energy
I	current
J	energy density
J_d	discharge energy density
N	density of states
Q	constant phase element
R	resistance
S	strain
T	temperature
T_m	melting temperature
U	volume
V	surface bias
V_{oc}	open circuit voltage
X	phase content
Z	PFM amplitude
a, b, c	lattice parameter
d_{33}	longitudinal piezoelectric constant
d_{31}	transverse piezoelectric constant
e	charge of an electron
f	volume fraction
k	Boltzmann constant
n	number density of charge carriers
p	polarization density
t	thickness

w	width of the depletion/accumulation layer
GO	graphite oxide
rGO	reduced graphite oxide
CNT	carbon nanotube
PVDF	poly(vinylidene fluoride)
DMF	N, N-dimethylformamide
MFC	microfibre composite
1.0-rGO@200	nanocomposite with 1.0 vol.% rGO reduced at 200°C
EDL	electrical double layer
TCEH	triangular cantilever energy harvester
BCA	bi-clamped cantilever actuator
SEM	scanning electron microscope
XRD	X-ray diffraction
FTIR	Fourier transformation infrared
ATR-IR	attenuated total reflection-infrared
AFM	atomic force microscope
PFM	piezoforce microscope
TTTT	all trans PVDF molecular chain
TTT$\bar{G}$	semi-trans PVDF molecular chain
TGT$\bar{G}$	trans-gauche PVDF molecular chain

Chapter 1 Introduction

Recent developments in aerospace and civil industries call for high performance ferroelectric materials that are durable, lightweight, and flexible to fulfil the application demands. The most widely reported solution is to incorporate the brittle ferroelectric ceramic into a soft polymer environment in hoping to combine the advantages of both materials. For instance, NASA used a macro fibre composite (MFC) as a sensor for ground vibration testing of their inflatable satellites. The MFCs are composed of PZT fibre and epoxy matrix and are highly flexible and lightweight, which can be integrated unobtrusively into the skin of a torus or space device forming an attractive testing arrangement. In addition, the functional material group (FMG) in University of Birmingham developed a needle-shape ultrasound transducer based on fine-scaled 1-3 PZT/epoxy composites for image guided neurosurgery. The enhanced durability and scalability of 1-3 composites make them possible to fit a Φ1.8mm transducer head while the composite structure also results in an increased electrical mechanical coupling and reduced the overall acoustic impedance that lead to a promising signal to noise ratio. However, the fabrication of ceramic/polymer composites, particularly those with fine-scaled structure, is still quite challenging, which can make them expensive solutions for practical uses. Besides, the relatively high solid loading of ceramic fillers also reduces flexibility of the composites.

Another solution that naturally existed is the polar polymers, and good examples can be poly(vinylidene fluoride) (PVDF) and its bi- and tri-polymer derivatives. The PVDF polymer possess at least 4 crystal structures, and three of these possess spontaneous polarizations due to the inter- and intramolecular dipole moment. This is to say, PVDF can simultaneously possess ferroelectric properties and the polymeric advantages such as lightweight and flexibility. However, the relatively low ferroelectric properties compared to the ceramic counterparts hinders their application potential. For instance, the relative dielectric permittivity of the pure PVDF, which originates from the dipole polarization in ferroelectrics, is merely 8~19 (at 1kHz), compared to that of over 1000 in pure ferroelectric ceramics. The piezoelectric constant d_{33} 17~50 pC/N, which is also significantly lower than that of the pure ferroelectric-ceramics. The most up-to-date approaches in enhancing the ferroelectric performance of the pure PVDF polymers is to incorporate conductive nano particles into the PVDF matrix, with carbon nanotube (CNT) and graphene (or a-few-layer graphite) being the most reported. Unlike the ceramic/polymer composites, the addition of CNT or graphene not only enhances the dielectric and piezoelectric performances of the pure polymer, but also leads to a higher mechanical strength. The conductive-nano-particle/polymer composites have been a popular topic for a decade, but there are still issues pending to be addressed. One major issue is the high dielectric loss associating to the addition of conductive particles. As these carbon nano particles typically possess a low percolation threshold, loss is very significant even at small solid loadings, which hinders their ferroelectric properties particularly at strong electric fields.

This thesis investigates the theoretical aspects of the reduced-graphite-oxide (rGO)/PVDF nanocomposites, with attention being focused on the impact of the heterointerfaces on the ferroelectric properties. Chapter 2 is a review of the fundamentals of ferroelectrics while Chapter 3 introduces the most up-to-date results reported in the theory and application of PVDF polymers and their composites. The aim and scope of the work are listed in detail in Chapter 4. Chapter 5 focuses on the experimental procedure for fabricating and characterizing the rGO/PVDF nanocomposites. A general model concerning the dielectric behaviour of a conductor/insulator composite is established in Chapter 6, which serves as the fundamentals for this project. Chapter 7 studies the energy storage capability of the rGO/PVDF composites and discussed with the model in Chapter 6. Chapter 8 focuses on the origin of polar conformation transition for PVDF molecule with respect to the rGO addition in the melting-recrystallization procedure. A unique symmetrical molecular dipole configuration to the rGO plane is also indicated. Chapter 9 assess the potential of rGO/PVDF nanocomposites in piezoelectric devices. Two devices were fabricated and tested, with one being a cantilever unimorph and the other being a flexible energy harvester. The findings of this project as well as the future work are summarized in chapter 10.

Chapter 2 Fundamentals of Ferroelectricity

2.1 Non-centrosymmetric Crystals

The symmetry of crystal can be described by 32 point groups. Any point in the unit cell can be defined by coordinates x, y, and z, with respect to the origin of symmetry. If the movement of this point from position (x,y,z) to position (-x, -y, -z) does not induce any difference, then the crystal can be called as a centrosymmetric crystal. Otherwise, the crystal is a non-centrosymmetric crystal. In terms of the centrosymmetric crystals, the centre of positive and negative charges will coincide, resulting in a zero net charge in the unit cell. While in terms of the non-centrosymmetric crystals, the separation of the centre of positive and negative charges produces a dipole moment with a built-in electric field opposite to the dipole orientation. This built-in potential will result in a charged state on the boundary of the unit cell. Due to this dipole moment, non-centrosymmetric crystals can respond to external stimuli such as electric field or heat, thus materials assembled with non-centrosymmetric crystals can possess unique functional properties for active device applications.

Out of 32 point groups, 21 point groups possess the non-centrosymmetric nature and exhibit piezoelectricity, in which the crystal can generate a strain response to the applied electric field and vice versa. 10 out of these 21 point groups possess spontaneous polarization (permanent dipole moment) in the absence of an electric field, which are classed as ferroelectric. If the spontaneous polarization changes with respect to temperature, then the crystal is pyroelectric. While if the spontaneous polarization can be permanently reoriented by the electric field, the crystal is then ferroelectric. Figure 2.1 shows the relationship of piezoelectric, pyroelectric, and ferroelectric materials. As seen, all ferroelectric materials are pyroelectric and piezoelectric. Good examples can be perovskite ceramics such as Barium-Titanite ($BaTiO_3$) and Lead-Zirconite-Titanite ($PbTi_xZr_{(1-x)}O_3$) which possess polarization switching characteristics with respect to the electric field. Polar crystals without the switching behaviour is pyroelectric but not ferroelectric. Examples of this kind of material can be found in ZnO in which the dipole moment is aligned with the crystal orientations and is non-switchable.[1] Non-centrosymmetric crystals with non-polar structure can generate an instantaneous dipole moment with respect to the stress or electric field, which is solely piezoelectric. Examples can be found in SiO_2 and GaAs crystals, in which there is no net dipole moment in static conditions.[2,3]

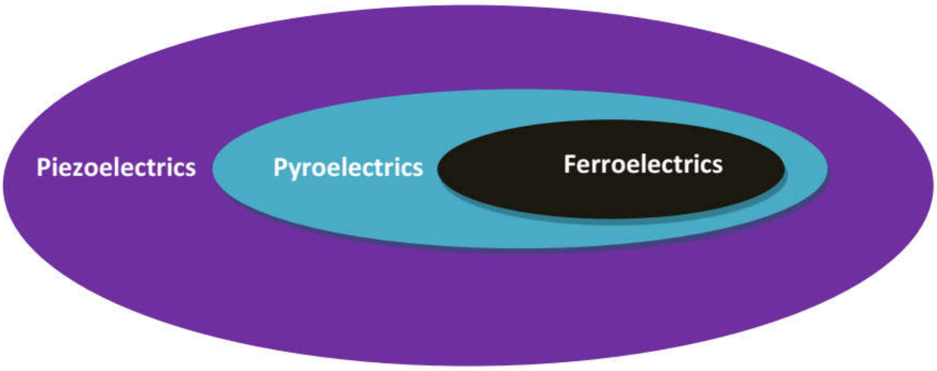

Figure 2.1 The relationship of ferroelectric, pyroelectric and piezoelectric materials

2.2 Piezoelectric Materials

The pre-fix piezo- is derived from the Greek word, which means to squeeze or press. Therefore, piezoelectricity defines the electric field induced strain (reverse piezoelectric effect) or strain induced charge displacement (direct piezoelectric effect) phenomena in a material. The history of piezoelectricity can be dated back to 1880, when Jacques and

Pierre Curie demonstrated the direct piezoelectric effect in the research of quartz and Rochelle salt ($KNaC_4H_4O_6 \cdot 4H_2O$).[4] Later, the reverse piezoelectric effect was also mathematically demonstrated by Gabriel Lippmann in 1881.[5] In the next few decades, piezoelectricity was only something of laboratory curiosity until the invention of Barium Titanite ($BaTiO_3$), which is a milestone in piezoelectricity.[6] Till now, piezoelectric materials have been used in a wide variety of applications such as sensors (direct piezoelectric effect) and actuators (converse piezoelectric effect), which are crucial components in modern industry.

The piezoelectric effect can be attributed to the dipole moment within the unit cell of the material, which originates from the non-centrosymmetric nature of the crystal structure. Figure 2.2 shows the crystal structure of Zinc Oxide (ZnO), which can be used to interpret the relationship between the piezoelectric effect and crystal structure. ZnO possess a hexagonal lattice structure and belongs to the $P6_3mc$ space group without a centre of symmetry.[7] This is because the alternating Zn^{2+} and O^{2-} planes in the c-axis, which induce the termination of [0001] planes at Zn atoms but $[000\bar{1}]$ planes at O atoms. Besides, the contrasting negativity on the top and bottom end of the unit cell also induces a dipole moment along the c-axis, thus making ZnO piezoelectric.[1] When stressed, the relative displacement between the Zn^{2+} and O^{2-} planes changes the dipole moment, hence screening charges to this dipole moment appear on the boundary of the unit cell resulting in a measurable charge displacement known as the direct piezoelectric effect. While when an electric field is applied, the dipole moment can respond by a displacement of the Zn^{2+}- and O^{2-}- planes, hence a strain is observable in the unit cell, which is known as converse piezoelectric effect.

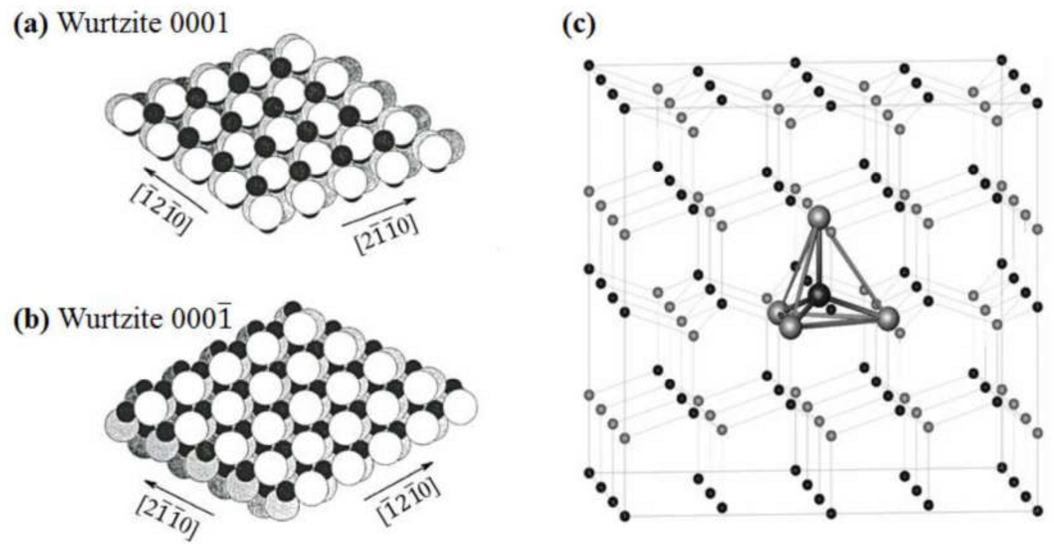

Figure 2.2 Crystal structure of ZnO showing an unswitchable dipole moment due to alternating Zn^{2+} (black sphere) and O^{2-} (grey sphere) planes[1]

The piezoelectric effect can be mathematically described by constitutive equations. In the orthorhombic coordinate system, if the plan of isotropy is defined as the xy-plane, then the poling direction can be defined as the z-axis, about which the material exhibits symmetry.[8] The field variables are the stress components (T_{ij}), strain components (S_{ij}), electric field components (E_k), and the electric displacement components (D_k). Hence, the piezoelectric constitutive equation can be defined as:

$$S_{ij} = s^{E}_{jkli} T_{kl} + d_{ijk} E_k \qquad (2.2.1)$$

$$D_k = d_{ijk} T_{kl} + \varepsilon^{T}_{ik} E_k \qquad (2.2.2)$$

where s is the compliance constant, d is the piezoelectric constant, and ε is the dielectric permittivity.[9-11] Equation (2.2.1) defines the converse piezoelectric effect of electric field induced strain with the contribution of the material mechanical properties while equation (2.2.2) defines the direct piezoelectric effect of strain induced charge displacement with the contribution of the material capacitance. The piezoelectric constant is identical in both converse and direct piezoelectric effect, which can be expressed with a matrix by taking into consideration of the symmetries of transversely isotropic material behaviour

$$\begin{pmatrix} 0 & 0 & 0 & 0 & d_{15} & 0 \\ 0 & 0 & 0 & d_{15} & 0 & 0 \\ d_{31} & d_{31} & d_{33} & 0 & 0 & 0 \end{pmatrix} \tag{2.2.3}$$

where d_{31} is the transverse piezoelectric constant, d_{33} is the vertical piezoelectric constant, and d_{15} is the sheer piezoelectric constant.[9-11] By combining the constitutive equation with the piezoelectric constant matrix, the piezoelectric behaviour can be mathematically described.

2.3 Pyroelectric Materials

The pre-fix pryo- means heat in Greek, hence pyroelectricity is a definition describing that material can generate a charge displacement with respect to the change of temperature. Crystals need to possess an intrinsic dipole moment to exhibit the pyroelectricity, hence pyroelectric materials are all piezoelectric but piezoelectric materials with non-polar crystal such as GaAs and quartz are not pyroelectric. ZnO, which has an intrinsic dipole moment aligned with its c-axis, is a good example of pyroelectric material.

Figure 2.3 is a schematic demonstration of the pyroelectric response with respect to a change in temperature. The intrinsic dipole moment of a material with polar crystal structure will generate a built-in electric field, which will be screened by space charges. A change in temperature dT will accordingly induce a change in the polarization of the material, and if the rate of change of temperature is higher than the screening rate of the space charge, a potential can be generated until a new equilibrium is established. Within this procedure, the charge flow can be observed in the external circuit to screen the change in polarization, resulting in a current response with respect to dT. The pyroelectric effect can be mathematically described as:

$$dP = pdT \tag{2.3.1}$$

where P is the polarization and p is the pyroelectric coefficient. Consider a time period of dt, the pyroelectric current I can be described as:

$$I = \frac{dP}{dt} = p\frac{AdT}{dt} \tag{2.3.2}$$

where A is the electrode area. Upon heating the material, the pyroelectric response becomes stronger as the temperature dependence of the polarization becomes stronger. However, above the Curie temperature, a critical temperature defining the polar to non-polar transition point, the pyroelectric response disappears as there is no dipole moment in the material. This means that the pyroelectric materials should be used at temperatures much below their Curie temperature. This results in pyroelectric coefficients being lower, but less variable with ambient temperature as the dependence of polarization on temperature is more linear at lower temperatures. The pyroelectric effect originates from the temperature induced depolarization of oriented dipoles, of which the procedure resembles that of the mechanical stress induced depolarization in the piezoelectric effect. For instance, for a pyroelectric material with well oriented dipole, a stress applied along the dipole orientation direction compresses the dipole and can result in depolarization, while releasing the stress will cause the dipole to return to its original status. This process will also induce screening charges to flow out or in, which is analogous to the procedure in Figure 2.3. Due to this fact, all pyroelectric materials are piezoelectric.

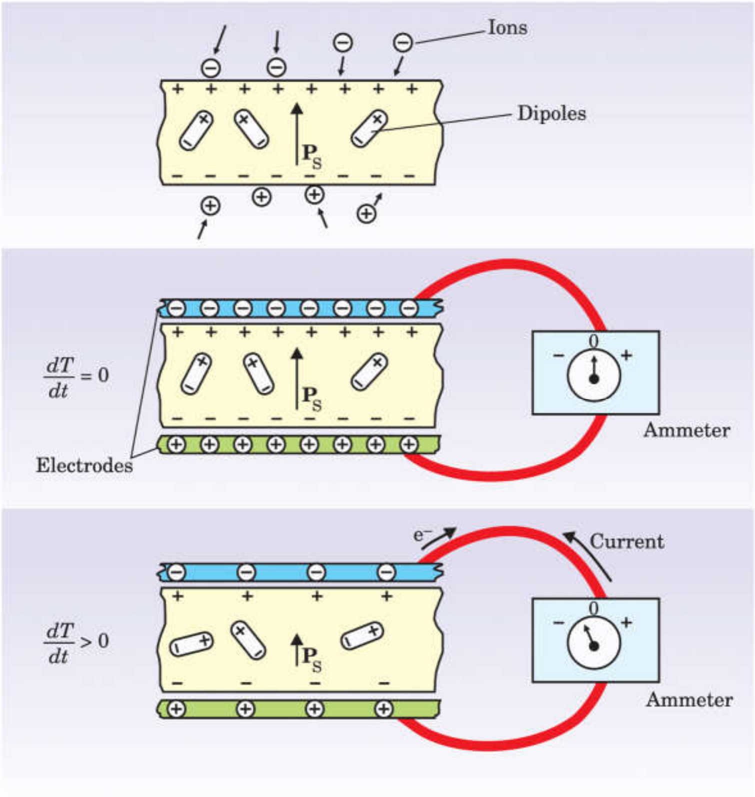

Figure 2.3 Illustration of the pyroelectric effect. An increase in temperature T reduces the spontaneous polarization Ps causing change in surface charge. This will induce a current flow to composite the change in surface charge.[12]

2.4 Ferroelectric Materials

The concept of ferroelectricity is derived from that of ferromagnetism. In ferromagnetic materials, the magnetic dipole moment is aligned to form a magnetic domain, which can be polarized by the magnetic field. In ferroelectric materials, it is the electrical dipole moment that forms the ferroelectric domain which can be reoriented by the electric field. Hence, a material is ferroelectric when (i) the material possesses spontaneous polarization and (ii) the spontaneous polarization is switchable with respect to the electric field.[13] Hence, ferroelectric materials are a subset of pyroelectric materials. Although ferroelectric domains comprise a set of dipole moments with the same orientation, a polycrystalline ferroelectric material can possess large quantities of randomly oriented domains, which cause the net dipole moment to be zero.[14] This is to say, the spontaneous polarization is isotropic and the ferroelectric material has to be polarized by an external electric field in order to exhibit piezoelectricity. Lead zirconate titanite ($Pb(Zr_xTi_{1-x})O_3$) and barium titanate ($BaTiO_3$) with perovskite ABO_3 structure are good examples of ferroelectric materials.

The crystal structure of $BaTiO_3$ is illustrated in Figure 2.4. Ever since the discovery of ferroelectricity in $BaTiO_3$ in 1945, it has been one of the mostly studied materials.[15] In the unit cell of $BaTiO_3$, the Ba^{2+} ions occupy the A sites at the corners while Ti^{4+} is at the body centre. The face centres of the unit cell are occupied by O^{2-} ions, which form a Ti-O octahedron. At high temperatures (above the Curie point), the crystal of $BaTiO_3$ possesses a centrosymmetric cubic structure with no distortion in the Ti-O octahedron. This results in zero dipole moment in the unit cell and the material is paraelectric. With the decrease of temperature, the $BaTiO_3$ crystal can be transferred from cubic to tetragonal (373K), orthorhombic (278K), and rhombohedral (183K) structures, each involving a small distortion to the Ti-O octahedron. These distortions can be regarded as the elongation of the cubic unit cell along particular crystal orientations, which will accordingly result in a relative displacement of the Ti^{4+} and O^{2-} ions. This can induce a net dipole moment in the unit cell, which give rise to the spontaneous polarization in the ferroelectric phases of $BaTiO_3$.

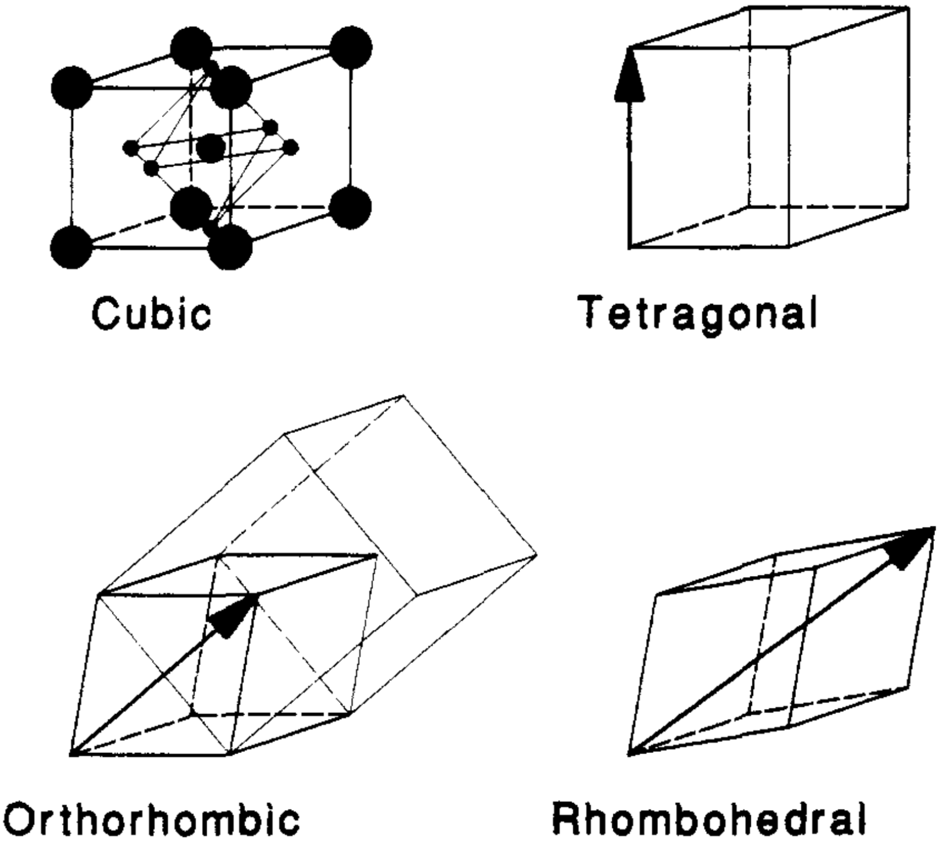

Figure 2.4 Schematic view of the structure of the different phases of $BaTiO_3$. The Ba^{2+} ions (large sphere) are located at the corners, the Ti^{4+} ions (medium sphere) at the centre, and the O^{2-} (small sphere) ions at the face centres. The arrows show the polar direction along the cubic [001] direction for the tetragonal phase, the [011] direction for the orthorhombic phase, and the [111] direction for the rhombohedral phase.[16]

Unlike ZnO whose spontaneous polarization is non-switchable, that in the $BaTiO_3$ possesses a switching behaviour with the influence of electric field.[17] This makes $BaTiO_3$ not only pyroelectric, but also ferroelectric. By applying an external field, the random oriented domains can be re-aligned to the field direction, which accordingly induces a net dipole moment. If the field strength is stronger enough (larger than the coercive field), these aligned dipole moment can be trapped after the unloading the electric field and the ferroelectric material can exhibit piezoelectricity. This procedure is named as polarization. P-E loops (polarization vs. electric field) are the most widely used method to illustrate the ferroelectricity of a material. A conventional P-E loop for a ferroelectric material after polarization saturation is shown in Figure 2.5.[18] The ferroelectric behaviour can be described by the remnant polarization P_r and coercive field E_c. While the P_r can represent the amount of trapped dipole upon unloading the external field, the E_c represent the ability of a ferroelectric material to withstand the external electric field without becoming depolarized. For a ferroelectric material with randomly oriented dipoles, applying an external electric field stronger than E_c can reoriented the dipoles along the electric field direction.

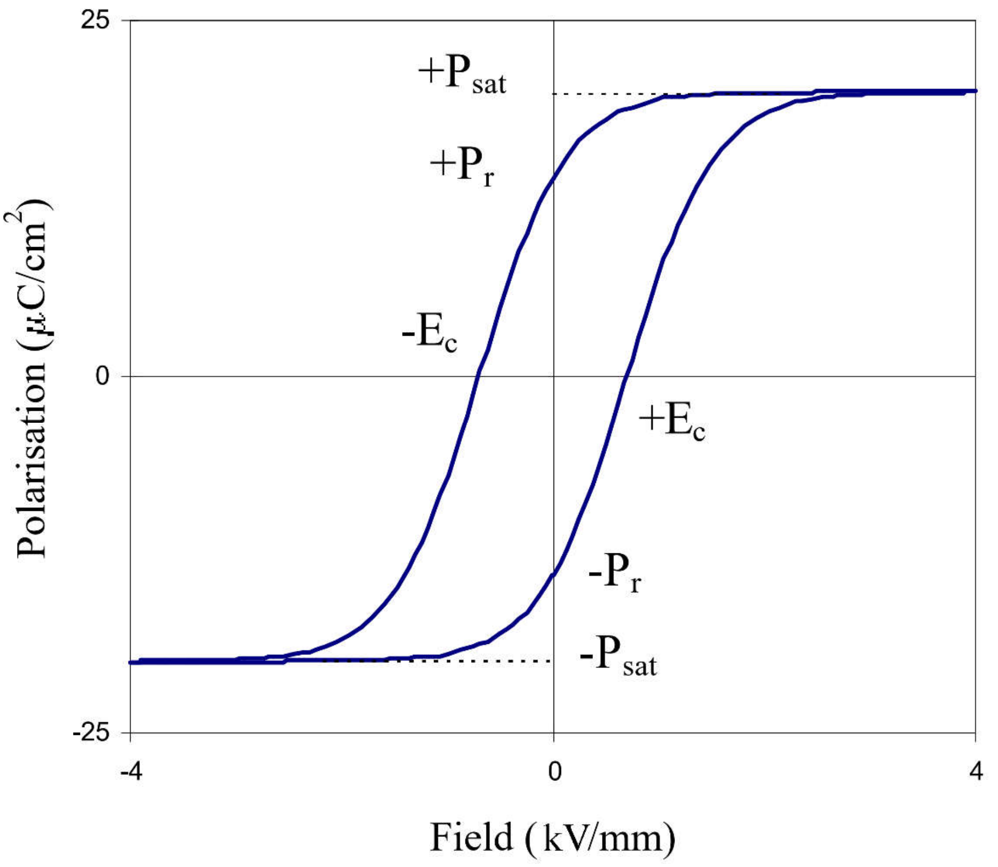

Figure 2.5 P-E hysteresis loop parameters for ferroelectric material[18]

In practise, a P-E loop is a D-E loop (charge displacement vs. field) as it is the charge displacement D that is measured. D originates from the capacitance of the material, which is a common response to electric field for all dielectrics and can be strongly coupled with their leakage phenomena. Hence, it may led to false interpretations of the material ferroelectric properties by solely use the P-E loop.[19,20] A more accurate method to identify the material's ferroelectricity is its I-E loop (current vs. electric field), which is shown in Figure 2.6. Upon approaching saturation, current increases with increasing E until E_C is reached then decreases with further increasing E. This is because fewer dipole moments can response to the electric field at saturation. Hence, the distinct phenomena associating to the switching behaviour of a ferroelectric material can be a current peak at E_c.

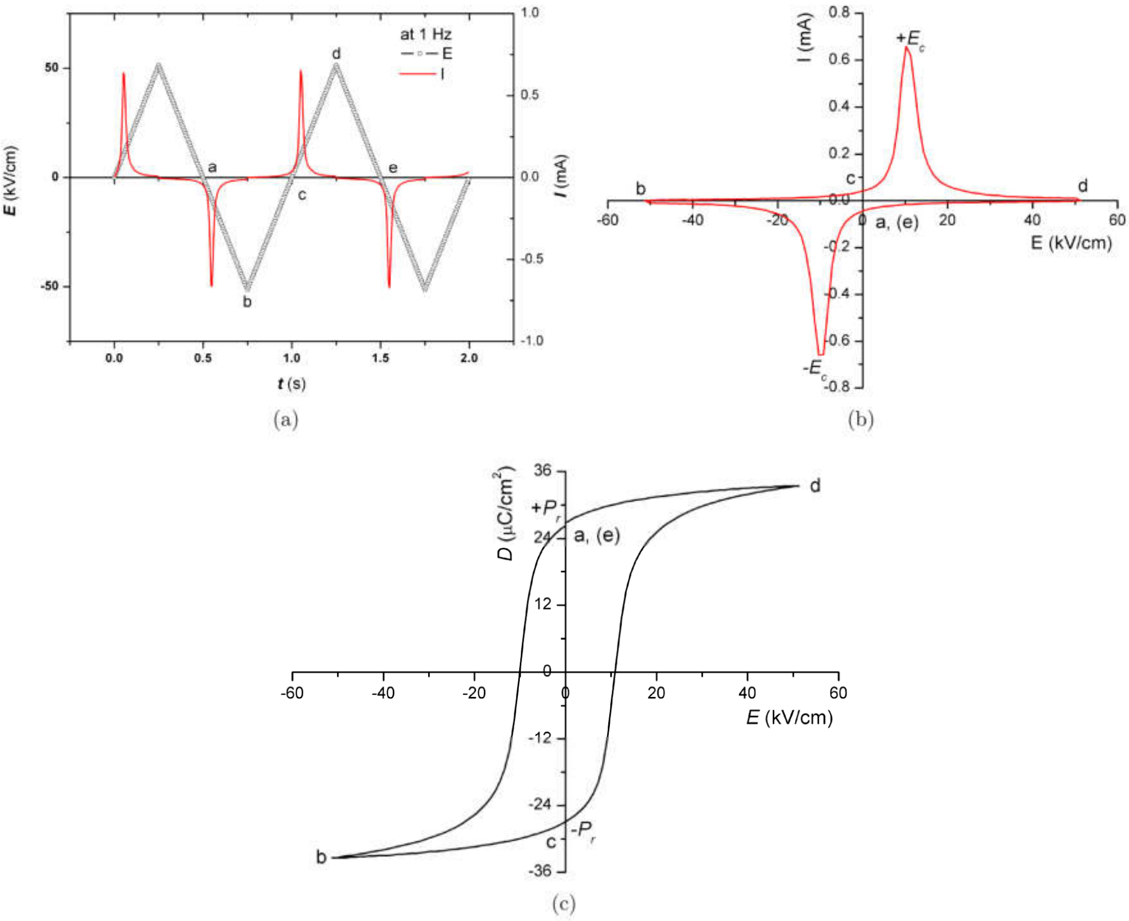

Figure 2.6 Electric displacement-electric field (D-E) loop measurement of NKN850 ceramics at 1Hz and 25°C. (a) Electric field versus time and current versus time (b) current-electric field (I-E) hysteresis loop, (c) electric displacement-electric field (D-E) loop.[19]

Chapter 3 Poly(vinylidene fluoride) Ferroelectric Polymers

3.1 Conformational and Crystal Structure

The investigation of the molecular conformation of the PVDF polymer can be dated back to the 1960s, when Wentink et al. firstly observed in their experiment that the infrared spectra of PVDF change dramatically with temperature.[21] Albeit that no explanation was given, their observations have attracted much attention to investigate the conformational structure of the PVDF polymers. Theoretical calculation reported by Liquori et al. indicates that more than one conformational structure exist in PVDF polymer chains, which was later observed by Cortili et al. from infrared spectroscopy (IR). [22,23] In their research, the PVDF sample films prepared from stretching after casting were found to possess all-trans (TTTT) chains while those directly casted without orientating treatment were found to possess trans-gauche (TGT$\overline{\mathrm{G}}$) ones. Besides, there is also a slightly defected form of TTTT conformation, which is found to be trans-trans-trans-gauche (TTTGTTT$\overline{\mathrm{G}}$).[23,24] As PVDF is a crystallized polymer, the packaging of molecule chains with different conformations can result in different crystal forms, those are TGT$\overline{\mathrm{G}}$-α, δ, TTTT-β, and TTTGTTT$\overline{\mathrm{G}}$-γ.

The most commonly observed phase in the PVDF polymer is the α phase, which can be attributed to its thermodynamic stability. The structure of α-PVDF is indicated in Figure 2.3.1. Early researches based on IR and XRD results have confirmed that the molecular chain conformation of α-PVDF is trans-gauche (TGT$\overline{\mathrm{G}}$), which is a chain conformation without intermolecular dipole moment. Hasegawa et al. proposed that the α-PVDF possess a pseudo orthorhombic unit cell with two TGTG chains packed in antiparallel manner along the c-axis. The unit cell belongs to C_{2h} point group with a lattice parameter of a=4.96 Å, b=9.64 Å, and c=4.96 Å. Due to the antiparallel manner of the chain package, no net intramolecular dipole moment will exist, hence the α-PVDF is a non-polar phase and is paraelectric. There is also a modified form of α phase called δ phase, which can be obtained by poling the α-PVDF at room temperature.[25] The structure of δ-PVDF is also indicated in Figure 3.1. Davis et al. firstly proposed the XRD spectrum of δ-PVDF by investigating the XRD and IR data, in which they claimed that its unit cell parameter and molecular conformation is same as that of α phase. However, changes in diffraction intensities can be observed in the δ-PVDF spectra, which can be an evidence of a new chain packaging structure. Bachmann et al. analysed the XRD data for δ-PVDF and proposed a statistical packing of the up and down chains at the same site in the orthorhombic cell with the space group $P2_1cn$. Unlike the α-PVDF, δ-PVDF is ferroelectric, in which the rotating of $TGT\overline{G}$ chains resulting in a net intramolecular dipole moment along the a-axis.

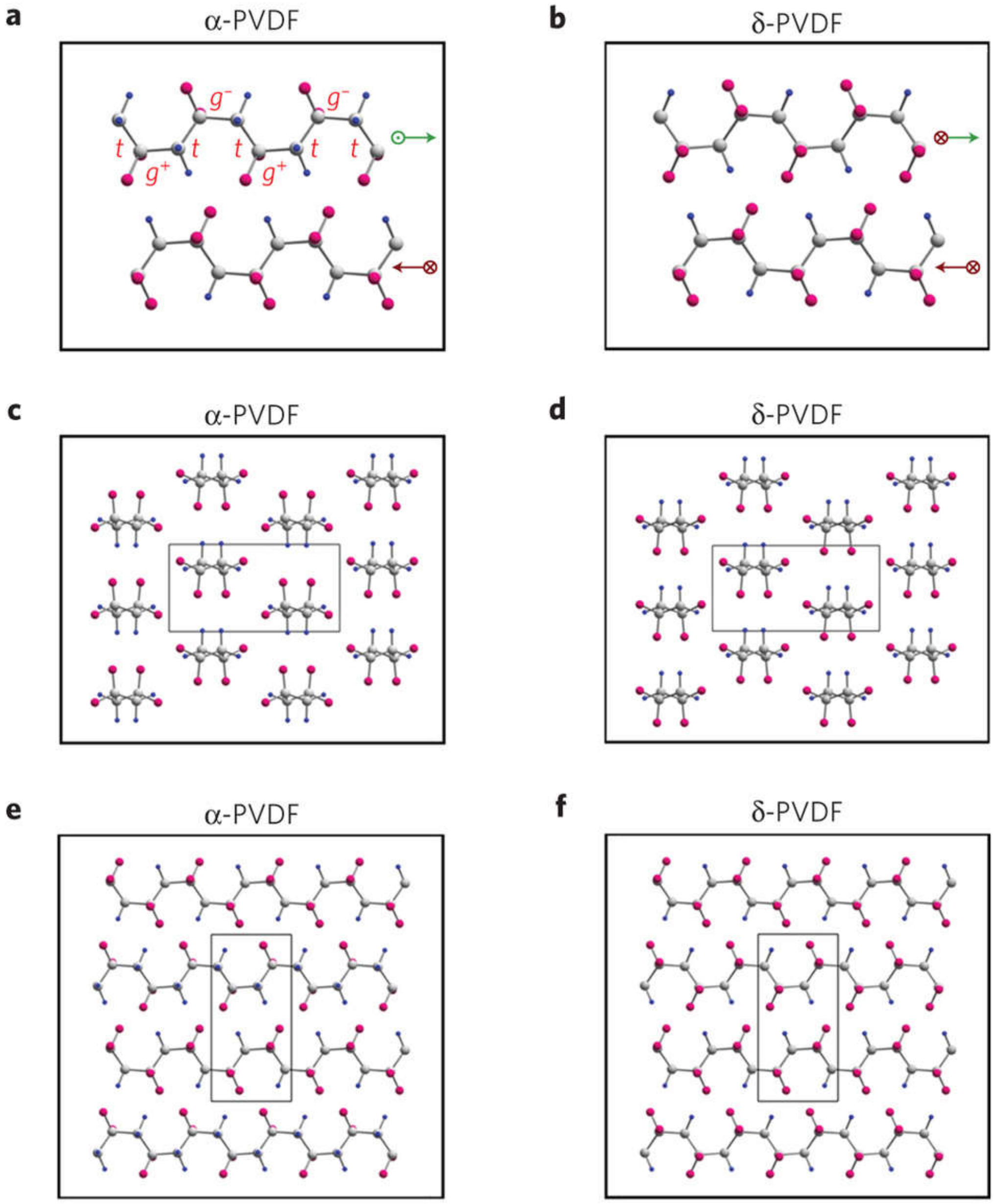

Figure 3.1 Molecular packing and crystal structure. (a), (b), Schematic packing of two polymer chains with the TGT$\overline{\text{G}}$ configuration in the unit cell of the α-phase and the δ-phase. The symbols present the in- and out-of-plane components of the dipole moment. In the α-phase all contributions cancel out. In the δ-phase the in-plane components cancel out but the out-of-plane ones yield a net microscopic dipole moment. (c), (d), The crystal structures and molecular packing of α-PVDF and δ-PVDF viewed along the c axis. The polymer chain is projected onto the ab-plane. (e), (f), Crystal structure of α-PVDF and δ-PVDF viewed along the a axis. The drawn inner lines represent the unit cells. Grey circles represent carbon atoms, red circles fluorine atoms and blue circles hydrogen atoms[25]

Lando et al. have conducted a XRD and NMR investigation in the crystal structure of β-PVDF polymer, which was later refined by Hasegawa et al. by taking into consideration of the CF_2-CF_2 steric hindrance.[26,27] The structure of β-PVDF is indicated in Figure 3.2, in comparison with that of α-PVDF. The unit cell of β-PVDF crystal was found to be orthorhombic, which belong to point group C_{2v}, with a unit cell parameter of a=8.58 Å, b=4.91 Å, and c=2.56 Å. The CH_2-CF_2 dipole in the in the TTTT chains cannot cancel each other, resulting in a net dipole moment in the unit cell.

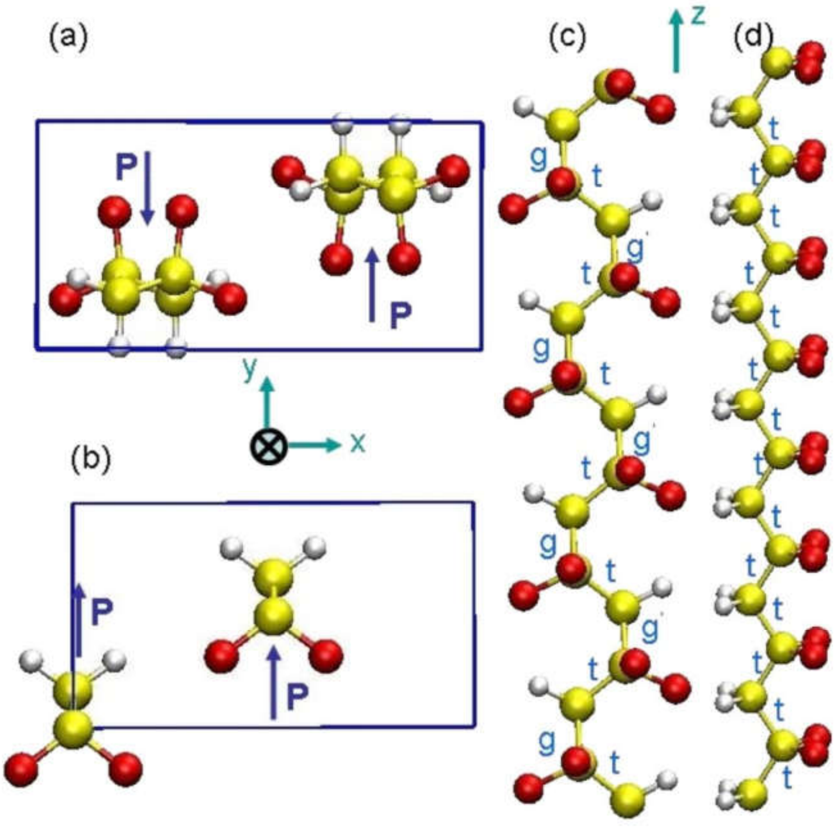

Figure 3.2 Comparison of the unit cell of the (a) α phase and (b) β phases. The yellow sphere is the carbon, the red sphere is fluorine, and the white sphere is hydrogen, (c) and (d) are the molecular structure of α phase and β phase.[28]

The identification of γ-PVDF crystal have been confused for a long time. Based on the IR results, Cortilli and Zerbi assumed that the γ phase might be a modified crystalline of β phase with some extent of chain conformation disordering.[23,24] However, later investigations have shown that the crystal structure of γ phase might be very different from that of β phase.[29] Weinhold et al. proposed an orthorhombic unit cell with a=4.97 Å, b=9.66 Å, and c=9.18 Å, in which two chains with a conformation of TTTGTTT$\overline{G}$ are packed.[30] The proposed structure is indicated in Figure 3.3. Almost at the same time, Takahashi et al. reported that the unit cell could be monoclinic with β=92.9°, and the cell parameter was found to be a=4.96 Å, b=9.58 Å, and c=9.23 Å, with chain conformation and packaging same as Weinhold's results.[31] The γ-PVDF as an independent crystalline form with TTTGTTT$\overline{G}$ conformation is finally approved by Tashiro et al. by combined measurements of IR, Raman and wide-angle-XRD, which is widely accepted nowadays.[32]

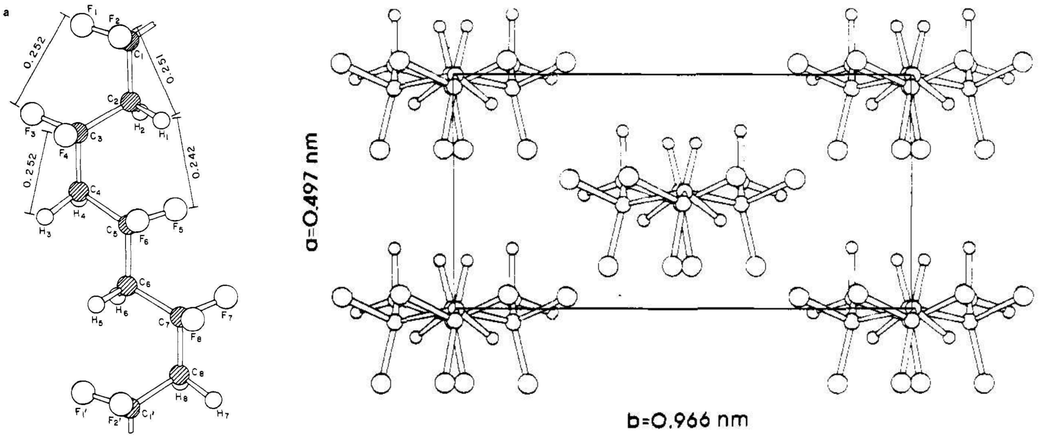

Figure 3.3 Molecular conformation and chain packing for γ-PVDF[30]

The crystal structure of PVDF can differs in samples processed at different conditions. The relation between phase and processing condition is indicated in Figure 3.4.[33] For instance, the solution-casted sample is a α phase when using non-polar solvents while that can be a γ or β phase when using polar solvents. In terms of melting, the cooling rate can play an important part as a normal cooling rate can always result in an α phase while an extremely fast cooling rate can always induce a β phase. Interconversion between phases in the as-prepared samples is also possible via specific treatments.

Mechanical stretching has been proved to be efficient in transferring α-PVDF into β-PVDF.[34,35] Cakmak et al. have reported an α/β mixture in the melting spun PVDF fibres, who claim that it might be the uniaxial stress that induced the formation of β phase. Later observations have assured this point of view as more β phase is presented in the stretched region compared with the non-stretched region and the transformation procedure is stress dependent. The mechanisms concerning the stress induced phase formation varies, including defects-assisting, molecular motion in the crystalline/amorphous interphase, crystal reorganisation, and chain reorientation. Electrical field is also capable to induce an in-situ α to β phase transition. Davis et al. reported a that the α phase can be transferred to δ phase at moderate field strength or to β phase at strong field strength.[36] More recent reports have shown that the direct transfer from α to β phase is physically not possible due to the large energy barriers and it is suggested that an α to γ to β transition route is more likely when an electric field is applied. These results have shown that the ferroelectric β phase cannot be naturally formed due to its relatively higher energy state over α phase, hence phase transition from α to β have to grab energy from the external source such mechanical, electrical or thermal energy in order to overcome the barriers.

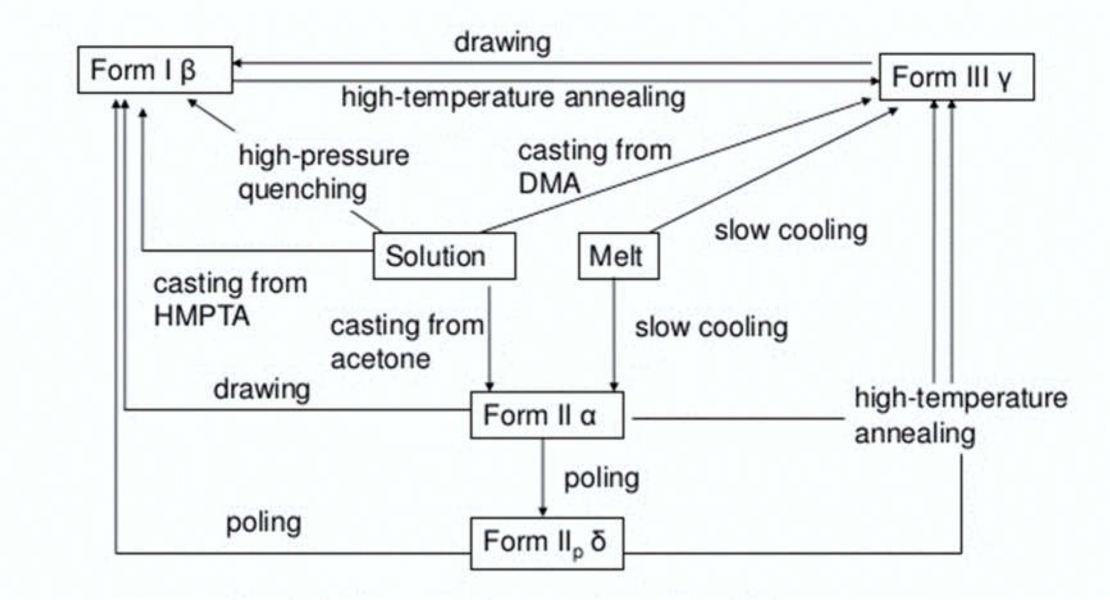
Form I β
drawing
high-temperature annealing
Form III γ
high-pressure quenching
casting from DMA
slow cooling
Solution
Melt
casting from HMPTA
casting from acetone
slow cooling
drawing
Form II α
high-temperature annealing
poling
poling
Form II$_p$ δ

Figure 3.4 Relation between PVDF phase and processing conditions, DMA is short for dimethylacetamide while HMPTA is short for hexamethylphosphoramide [33]

3.2 Ferroelectricity in PVDF Polymers

Ferroelectric materials are defined as material that possess spontaneous polarization which is switchable by the electric field. As discussed above, β, γ, and δ-PVDF can all be ferroelectric as they possess either intermolecular (β, γ) or intermolecular (δ) electric dipoles. Herein in this section, we use the β phase as an example to introduce the ferroelectricity in PVDF polymers.

As is well known that the polarization direction is aligned with the b-axis of the β-PVDF unit cell, hence the switching behaviour can be monitored by the crystal structure changes from a unpoled sample to a poled one. Early days observations of the piezoelectric and pyroelectric responses of the PVDF polymer have led to two primarily assumptions, with one being the trapped charge effect and the other being the polarization switching. Kepler et al. studied the X-ray intensity of β-PVDF as a function of sample orientation, in which a poling process can induce order in the orientation of the crystalline regions.[37] This gives an evidence of the domain switching behaviour, which indicates that the β-PVDF is ferroelectric. Also, in their research, the maximum polarization P of the β-PVDF induced by a poling process is:

$$P = \frac{3}{\pi} P_0$$

where P_0 is the polarization in ideal conditions where all dipoles are perfectly aligned with the electric field. Another demonstration of the switching behaviour of the β-PVDF is done by Takahashi et al. who compared the intensity of the (110) planes by changing the sign of the electric field. They found that the intensities of (110) under positive and negative poling are different, hence if assign the crystal plane of positively poled β-PVDF as [110], then that of negatively poled is then $[\bar{1}\bar{1}0]$.[38]

3.3 PVDF Composites with Inorganic Inclusions

The most significant advantage of PVDF polymer is their highly insulation nature, which result in a high dielectric strength. A pure PVDF polymer can possess a E_c over 200MV/m leading to a large discharging energy density, which can be attributed to its highly insulating nature.[39-41] Hence, pure PVDF polymer is suitable in strong field applications, particularly capacitors with high power output. While in the weak field, their functionality can be hindered by the relatively weaker ferroelectric properties. Pure PVDF polymer typically possess a relative dielectric permittivity from 8~19 (1kHz), and a piezoelectric constant up to 50 pC/N (effective value measured in PVDF thin film), which is far lower than their ceramic counterparts.[42,43] Therefore, alternative routes that could effectively improve the ferroelectric properties of the PVDF polymers is still an open question nowadays.

Introducing a heteroadditive into polymer matrix to form a 0-3 composite has long been known as an efficient method to improve the properties of the pure polymer. For example, Shah et al. have reported a dramatic enhancement in mechanical properties in nanoclay filled PVDF polymers, where an increase of 0.5 GPa and 120% in elongation was observed in comparison with the unfilled neat polymer.[44] Javadi et al. have reported an enhanced strain energy density in chemically modified graphene/P(VDF-TrFE-CFE) nanocomposite that is 4700 times larger than the pure polymer.[45] Li et al. have reported an increase in conductivity in thermally reduced graphene/PVDF nanocomposites, where a conductivity of 10^{-3} S/m was observed at a graphene content of 0.105 vol.%.[46] The most widely studied aspect in PVDF composites is their enhanced dielectric performance. In this section, we will use the dielectric performance as an example to introduce the effect of inclusion additions.

A straight forward idea for boosting the dielectric response of a ferroelectric polymer is to add ferroelectric ceramics with large permittivity to utilize the mixing effect. These composites usually possess an inclusion volume fraction of 50 vol.% ~ 60vol.% and dielectric permittivity significantly higher than that of the pure polymer. For instance, Mao et al. managed to achieve a dielectric permittivity of 95 at 1kHz and $BaTiO_3$ (100nm) of 60 vol.%, corresponding to 9 times increase over that of the pure PVDF.[47] The major challenge in fabricating PVDF composites with ceramic inclusions is how to avoid high leakage induced by Ohmic contact of agglomerated particles. Till now, the most efficient route to address this issue is to coat a highly insulating polymer on the ceramic particle surface to prevent direction charge transfer between adjacent particles.[48,49] Figure 3.5 shows the polymer grafting process to coat the $BaTiO_3$ surface reported by Yang et al.[48] In their research, $BaTiO_3$ nanoparticles were first functionalized by poly(1H,1H,2H,2H-heptadecafluorodecyl acrylate) (PHFDA) and poly(trifluoroethyl acrylate) (PTFEA) via reversible addition-fragmentation chain transfer (RAFT) technique before mixing and hot-pressing with poly(vinylidene fluoride-co-hexafluoropropylene) (P(VDF-HFP)) polymer. The coating possesses thickness from 2~6nm, which well isolates the $BaTiO_3$ particles. Composites with 50 vol.% $BaTiO_3$ of both coatings possess analogous dielectric permittivity around 45 at 1kHz, this results in a discharge energy density up to 4 times higher than the pure P(VDF-HFP) (at 20kV/mm, 10Hz).

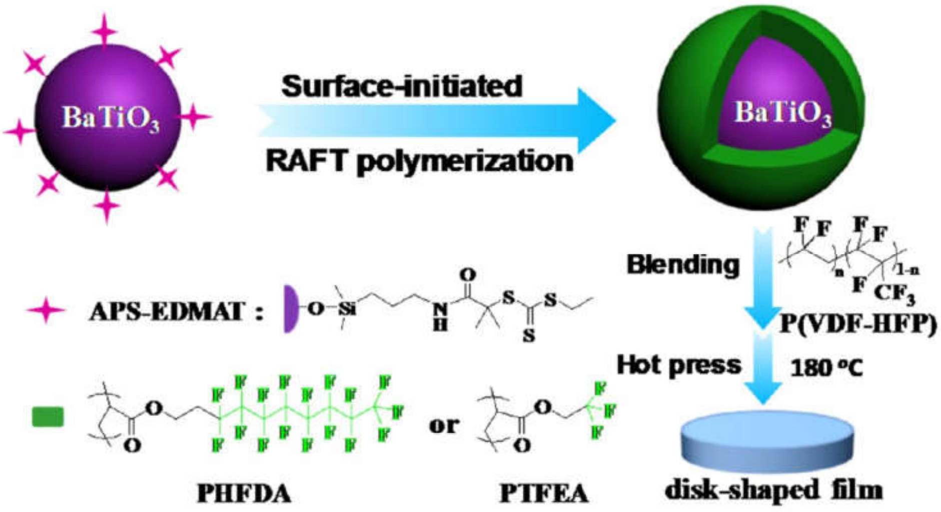

Figure 3.5 Schematic illustration for the preparation of fluoro-polymer@$BaTiO_3$ nanoparticles and P(VDF-HFP) nanocomposite films[48]

The major drawback of using ceramic particles as an inclusion to enhance the composite dielectric response is that a high solid loading is always needed. This increases the fabrication difficulty as well as degrades the composite mechanical strength. An attractive new candidate for hybridizing with ferroelectric polymers can be nano-sized conductive particles such as carbon nanotube and graphene, which have been demonstrated to induce a gigantic dielectric permittivity in composites with small solid loadings.[50,51] Analogous to the ceramic fillers, pristine nano-carbons can also exhibit poor dispersity in the PVDF solutions, therefore the polymerization technique is also introduced to coating the nano-carbons.[52-54] Apart from this, there are also reports of use the intrinsic oxidized form of nano-carbons and thermally or chemically reduced in-situ in composite to retain its conductivity.[55-57] For instance, Tang et al. used an in-situ thermal reduction technique to fabricate a rGO/PVDF nanocomposite, with graphite-oxide (GO) as the raw inclusion.[57] The hydrophilic GO provides good dispersity in PVDF casting solutions and can be thermally reduced in-situ to conductive rGO, as shown in Figure 3.6. The dielectric permittivity and tanδ was found to be 662 and ~4 at 1kHz with merely 2.4 vol.% solid loadings, providing to be the best combination reported. However, even with this promising dielectric figure, the energy storage performance of composites with nano-carbons has not been widely reported. Hence, how these high permittivity composites would behave at strong charging field remains to be a question in this research scenario.

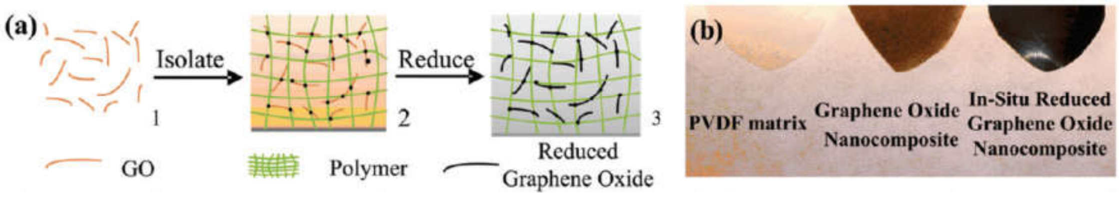
(a)
Isolate
Reduce
1
2
3
GO
Polymer
Reduced Graphene Oxide
(b)
PVDF matrix
Graphene Oxide Nanocomposite
In-Situ Reduced Graphene Oxide Nanocomposite

Figure 3.6 (a) Image of the graphene oxide and nanocomposite: (a) the in situ reduced process for the single layer reduced-graphene oxide nanocomposite, (b) digital image of graphene oxide and in situ reduced-graphene oxide nanocomposite[57]

Mechanisms concerning the enhanced dielectric response in composite materials can be classified into two categories: (i) the mixing rules dealing with the contribution of inclusion dielectric permittivity and (ii) interfacial interaction model dealing with the contribution of inclusion/matrix interface. The mixing rules include Lichtenecker's formula, Maxwell-Garnett equations, and Bruggemen approximation.[58] Lichtenecker's formula is the simplest form among those in mixing rules, which can be expressed as:

$$\log \varepsilon_m = f \log \varepsilon_p + (1-f) \log \varepsilon_c \tag{3.3.1}$$

where ε_m, ε_p, and ε_c is the dielectric permittivity of composite, polymer and ceramic, respectively, and f is the solid loading.[59] While Lichtenecker's formula always lead to large errors in practise, the Maxwell-Garnett and Bruggeman's formula are more commonly used. The Maxwell-Garnett model can be expressed as:[60,61]

$$\varepsilon_m = \varepsilon_p \left(1 + \frac{2f(\frac{\varepsilon_c - \varepsilon_p}{\varepsilon_c + 2\varepsilon_p})}{1 - f(\frac{\varepsilon_c - \varepsilon_p}{\varepsilon_c + 2\varepsilon_p})} \right) \tag{3.3.2}$$

while the Bruggeman's formula can be expressed as:[62]

$$\varepsilon_m = \frac{f}{3}(\varepsilon_c - \varepsilon_p)\frac{\varepsilon_m}{\varepsilon_m + (\varepsilon_c - \varepsilon_p)} \tag{3.3.3}$$

The drawbacks of the mixing rules can be obvious, that the solid loading is regarded as the only factor that dominates the dielectric response of the composites. Hence, the mixing rules are not suitable to describe the size effect of the inclusions. Besides, the mixing rules are more of a macroscopic approximation of the dielectric behaviour, and the microscopic kinetics behind the dielectric response is still unclear. This means that the mixing rules is insufficient to deal with the loss of the composites.

The addition of inclusion particles can induce massive interfaces, which give rise to the interfacial interaction model, such as Lewi's model and Tanaka's model. These models based on the assumption that an electric double layer or analogous structure should exist on the inclusion surface giving rise to an improved dielectric in composites over the matrix.[63-65] The static condition of an inclusion surface assumed by Lewi is sketched in Figure 3.7.[63] The inclusion is regarded as a metallic, of which the surface is assumed as negatively charged due to a Fermi level or electrochemical potential difference between inclusion and matrix. The negatively charged inclusion surface can absorb free charge carriers such as ions and molecules to construct an electrical double layer (EDL) structure as sketched in Figure 3.7. The inner Helmholtz layer, which is indicated as layer (c) in the figure, is the front layer of the EDL and is composed of tightly bonded ions and highly ordered molecules. This inner Helmholtz layer is followed by a less ordered outer Helmholtz layer (d) and a loosely bonded Gouy-Chapman diffusion layer (e). The charge density δ(r) in the double layer with respect to the distance away from the surface r, which can be described using Poisson-Boltzmann relation as:

$$\delta(r) = \delta_\infty \exp(-\frac{ze\varphi(r)}{kT}) \tag{3.3.4}$$

where δ_∞ is the charge density in the bulk matrix, z is the valence, $e=1.60\times10^{-19}$C is the electron charge, φ(r) potential gradient, $k=1.38\times10^{-23}\mathrm{m^2kgs^{-2}K^{-1}}$ is the Boltzmann constant and T is the temperature in Kelvin. The length of the accumulation layer is defined as the 1/κ where κ is the Debye-Huckel parameter with unit of $\mathrm{m^{-1}}$ as:[42]

$$\kappa = \sqrt{\frac{2e^2z^2n_\infty}{\varepsilon_m kT}} \tag{3.3.5}$$

where ε_m is the dielectric permittivity of the matrix. With the definition of κ, the potential gradient $\varphi(r)$ can be described as:

$$\varphi(r) = \varphi_0 \exp(-\kappa r) \tag{3.3.6}$$

where φ_0 is the potential on the inclusion surface. These equations are also claimed to be valid at the existence of an applied surface potential. The surface interaction model indicates a strong charge polarization on the inclusion surface, which explains the advantageous of inclusion particles with large surface area in contributing a large dielectric permittivity to the composites. However, this model resembles the matrix as an electrolyte with mobile charge carriers. As dielectric matrix is normally an insulator with wide band gap, their electrical behaviour may be very different from an electrolyte. Besides, only the properties of the matrix are considered with inclusions treated solely as a charge blocking site. This fails to explain the variation between dielectric responses for composites with conductive and non-conductive inclusions.

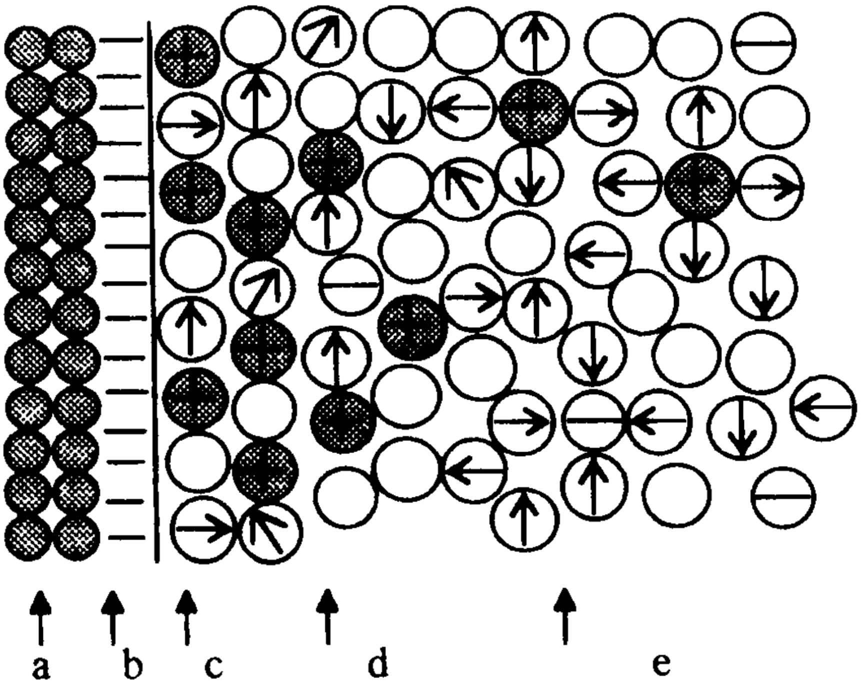

Figure 3.7 A metal electrode-dielectric interface showing (a), positive metal cores; (b), the outer electron cloud of the metal; (c), the structured inner Helmholtz layer of molecules and ions; (d), the outer Helmholtz layer and (e), the Gouy-Chapman diffuse space charge layer. The arrows indicate the orientation of polar molecules, and the molecules at the inner Helmholtz layer are highly ordered compared to those at the diffusion layer. [63]

To discuss the mechanism of loss, Bowen et al. proposed an electric field concentration model via finite element analysis (FEA) method, as shown in Figure 3.8. [66] In their research, a matrix with relative dielectric permittivity ε_r=1 is divided to 50×50 squares. An inclusion particle occupies a single square, with ε_r set to be 10^6 so that the field distribution on the inclusion phase is 0. This means the inclusion particles are in permanently breakdown status resembling conductors. The modelling results indicate that the addition of inclusion always magnifies the applied field E, resulting in a local field E_{local}>E. Therefore, it is indicated that this field concentration contributes to an improved effective dielectric permittivity to the composites. The field concentration is found to be dependent on the inclusion volume fraction, with higher volume fraction giving rise to a higher field concentration. Besides, the field concentration model also deals with the dielectric strength of the composites. As the E_{local} may be far stronger than the E applied, the composites possessing a large ε may simultaneously possess weaker E_b.

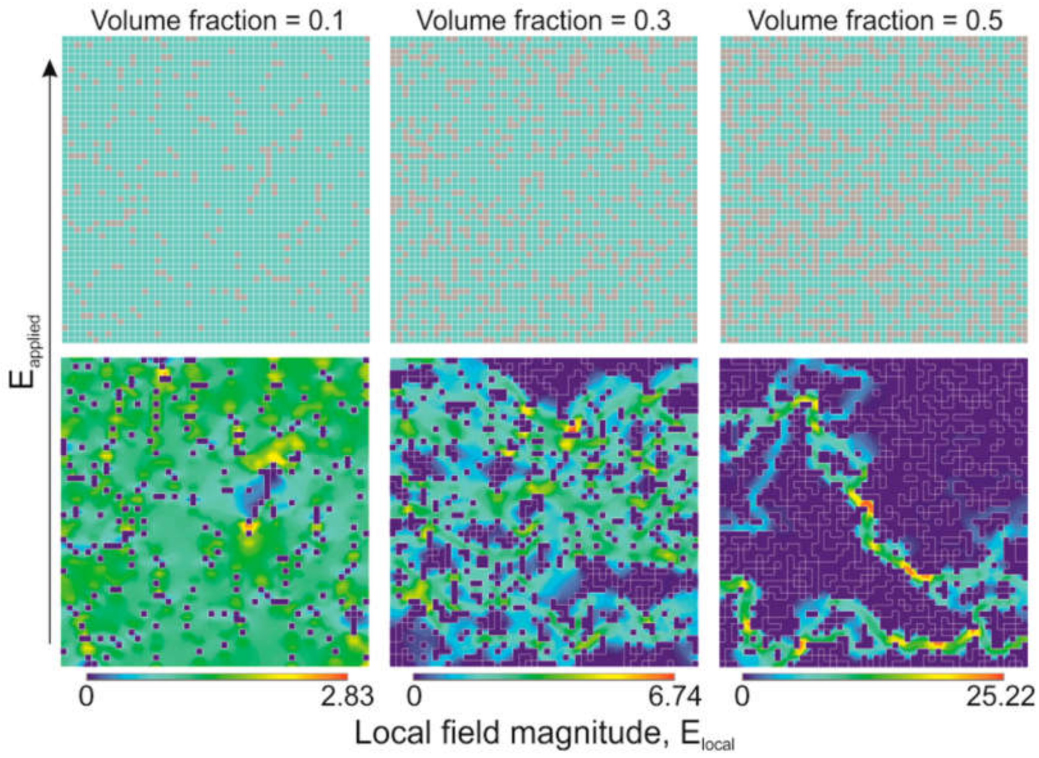

Figure 3.8 Finite element model of two phase composites with varying volume fraction of the conducting phase. Upper images show example random distributions of the conductor (gray) in a dielectric matrix (cyan), and lower images are corresponding contour plots after application of a normalized external electric field ($E_{applied}$=1). For a filler-free matrix, E_{local}=1 at all locations.[66]

3.4 β-Phase Formation in PVDF Composites

The addition of inclusions also affects the crystallization kinetics for the PVDF polymers, as many researchers have observed a core-shell structure compromising a layer of β phase crystal absorbed on the inclusion surface. Levi et al. reported an enhancement in the piezo- and pyroelectric properties in CNT/PVDF composites and claimed that this enhancement might be corelated to the increased β phase crystallinity.[50] They claimed that the β phase might have some energetic relation with the CNT surfaces as: (i) a layer of polymeric coating was observed on the CNT surface and (ii) the β phase content is sensitive to the loading of CNT. Martins et al. obtained 90% β phase in $CoFe_2O_4$/PVDF composites with a $CoFe_2O_4$ loading of 5 wt.%.[67] A core-shell structure was also observed, and the coating layer was later assigned to be β-PVDF with a face-on molecular orientation. Other researchers also reported a β phase formation in PVDF composites with varies inclusion species.[68-70] These findings indicate the β phase formation in PVDF composites is a universal phenomenon, which causes many debates on the formation mechanisms.

The challenges of interpreting the inclusion induced β-PVDF formation mechanism can be indicated from the example of a CNT/PVDF composites. Yu et al. studied the β phase formation mechanism on the CNT interface with the help of density functional theory (DFT) the model for simulation is illustrated in Figure 3.4.1 (a) to (h).[71] In their results, they suggested that both TTTT and $\mathrm{TGT}\bar{G}$ chains can be absorbed on the CNT surface, and the TTTT chain bonds more tightly on the CNT surface than the $\mathrm{TGT}\bar{G}$ chain does. This indicates a confining effect of CNT surface, which is also widely observed in other organic/inorganic type interfaces.[72-75]. Many assumptions have been proposed to generate a molecular level explanation for this confining effect. For instance, Manna et al. attributed the β phase formation on the CNT surface to the matching of the zig-zag morphology between the PVDF chains and carbon atoms.[76] While, Ke et al. fabricated a series of PVDF composites with surface functionalized CNT, and attributed the formation of β phase to the chemical interactions between the -CF_2 or -CH_2 and the functional groups.[77] Comparing these two reports, it is obvious that CNT with both pristine and functionalized surface can induce a β-PVDF, which means neither a morphological matching nor hydrogen bonding is mandatory.

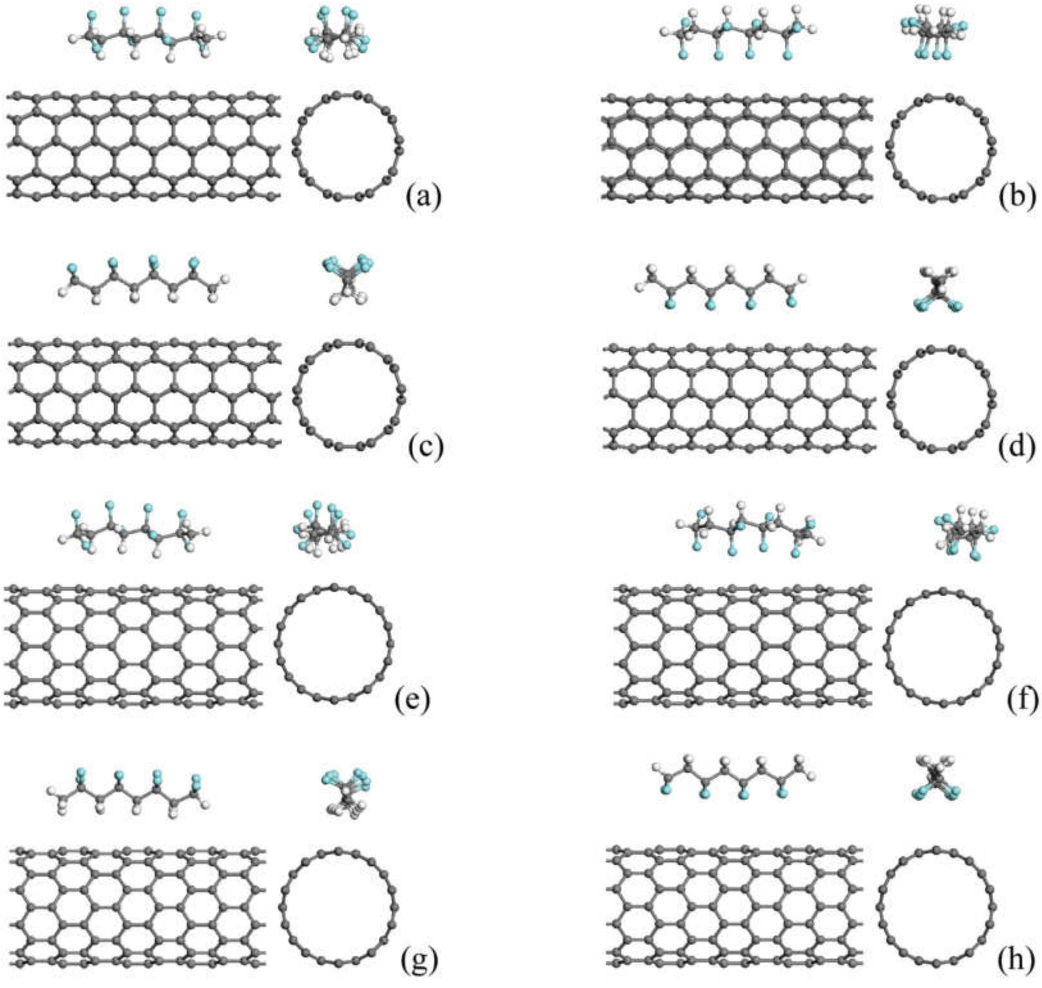

Figure 3.9 Simulation model describing (a), (b) TGT$\bar{G}$ and (c), (d) TTTT chains absorbed on the armchair CNT tube, (e), (f) TGT$\bar{G}$ and (g), (h) TTTT chains absorbed on the zig-zag CNT tube[71]

On assumption that could potentially be universally explored concerning the inclusion induced β-PVDF is the ion-dipole interaction model. Martins et al. studied the β phase formation mechanism in PVDF 0-3 composites.[67] They fabricated the PVDF composites with two kinds inclusions, those are $NiFe_2O_4$ and $CoFe_2O_4$, and found that the β phase content in $CoFe_2O_4$/PVDF composite is much higher than that in $NiFe_2O_4$/PVDF. By conducting a Zeta potential test for both inclusion particles, it was found that the Zeta potential of $CoFe_2O_4$ is higher than that of the $NiFe_2O_4$, while the potential value for both inclusions are negative. Based on this, it is claimed that the ion on the inclusion surface causes an electrostatic field which interacts with the molecular dipole inducing β-PVDF formation, as indicated in Figure 3.10. However, no direct evidence of the β-PVDF dipole orientation is given in the research, hence the ion-dipole interaction model is still not demonstrated. Besides, the charged state of the inclusion surface may be different in the PVDF casting solution to that measured from Zeta potential. These insufficiencies cast some doubt on the ion-dipole interaction model, which means a universal mechanism concerning the inclusion induced β-PVDF formation is still not well established.

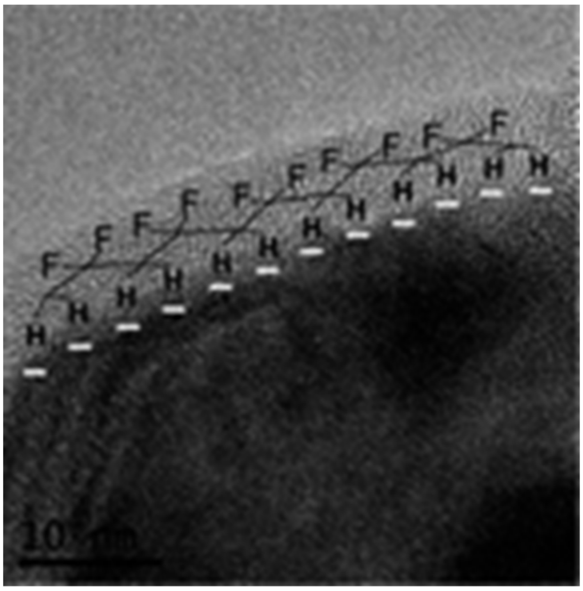

Figure 3.10 Schematic representation of the interaction between $CoFe_2O_4$ nanoparticles and PVDF chains in the nanocomposite: the partially positive C–H bonds of the polymer are attracted by the negatively charged ferrite surface due to the static electric force. This leads to the all-trans conformation of the polymer phase[67]

Chapter 4 Aim and Objectives

This project is concerned with a broad but systematic investigation of the role of heterointerface in rGO/PVDF composite materials. The overall aim of this project is to find the missing link between the interfacial electrical interaction and the structure and ferroelectric properties of the composite materials. The ambition is thus to unify the changes in structure and properties in the composite material with respect to the inclusion addition to the interfacial electrical interactions. Several objectives have been designed to achieve this goal, which are listed as follows:

- To fabricate a group of PVDF nanocomposites with different volume fractions of homogeneous dispersed reduced-graphite-oxide (rGO) via in-situ thermal reduction technique as an example to study the interfacial interactions.
- To establish a general model of the inclusion/matrix interface that highlights the effect of electrical contrast and inclusion geometry on the dielectric behaviour, those are dielectric response and loss, of the composites.
- To investigate the energy storage behaviour of the rGO/PVDF nanocomposites and discuss with the heterointerface model. To
- To investigate the phase transformation phenomenon of PVDF polymer with respect to rGO addition and discuss with the heterointerface model.
- To fabricate piezoelectric devices with the rGO/PVDF nanocomposites, to study the role of interfaces in the piezoelectric properties of these devices

Chapter 5 Experimental and Measurement Methods

5.1 Solution-casting of Pure PVDF film

The pure PVDF films were prepared via a solution-casting method. 2.5g PVDF powders (Alfa Aesar, UK) were dissolved into 10mL N, N-dimethylformamide (DMF, ACS, 99.8%, Alfa Aesar, UK) solvent in a 50mL glass tube. The glass tube is then closed with a plastic cap and sealed with tape, followed by magnetic stirring for 4h at room temperature to fully break the agglomerations. The casting solution was then poured onto a clean glass substrate and air dried overnight at room temperature. Then, the dried PVDF films were peeled off from the substrates, sandwiched by alumina substrates, transferred to the oven and thermally annealed at 100°C for 2h to completely remove the residue solvents.

5.2 Solution-casting of the GO/PVDF Nanocomposites

Two kinds of carbon nanomaterials were chosen as the starting filler to fabricate the nanocomposites, these are graphite oxide (GO) and commercial graphite nanoplate (xGnP, Strem Chemistry, USA). The GO powders are generously provided by the Surface Engineering Groups in University of Birmingham, which were fabricated via an improved Hammer's method. Briefly, graphite flakes with an average diameter of 45μm (99.8% Alfa Aesar, UK) were mixed with $KMnO_4$ at a weight ratio of 1:6 (3g/18g), followed by infiltrating a H_2SO_4 (98%) and H_3PO_4 solvent mixture with a volume ratio of 9:1 (360 ml/40 ml). The mixed suspension was then stirred for 12h at 50 °C on a ceramic hotplate incorporating a magnetic stirrer. After cooling, the suspension was poured into a beaker with 400 ml distilled water and 3 ml H_2O_2, and then centrifuged several times to separate the GO powders. The separated GO was oven dried at 90°C for 24h and stored until required. To obtain a homogeneous dispersion, 0.1g GO and 0.1g xGnP powders were dispersed into 10ml DMF solvents and sonicated for 12h before use. The dispersibility of GO and xGnP in DMF solvents were compared after 4 days of sedimentation as shown in Figure 5.1 (a) and (b). As indicated, the GO can provide more stable dispersion compared to that of xGnP, as few residues can be observed on the bottom of GO bottle. Hence, the GO dispersion is chosen for the following experiment.

To improve the accuracy of GO content, 0.13g GO powder were dispersed in 10mL DMF solvent to prepare the GO concentrated mixture. The mixture was then sonication for 8h in a sealed glass tube. To prepare nanocomposites with GO content of 1.0 vol.%, 1.5 vol.%, 2.0 vol.%, and 2.5 vol.%, 2.5g PVDF powders were added to 0.45g, 0.68g, 0.92g, and 1.16g GO/DMF mixture and then magnetic stirred for 4h at room temperature until no agglomerations present. The casting solution was then poured onto a clean glass substrate and air dried overnight at room temperature. Then, the dried GO/PVDF films were peeled off from the substrates, sandwiched by alumina substrates, transferred to the oven and thermally annealed at 100°C for 2h to completely remove the residual solvents.

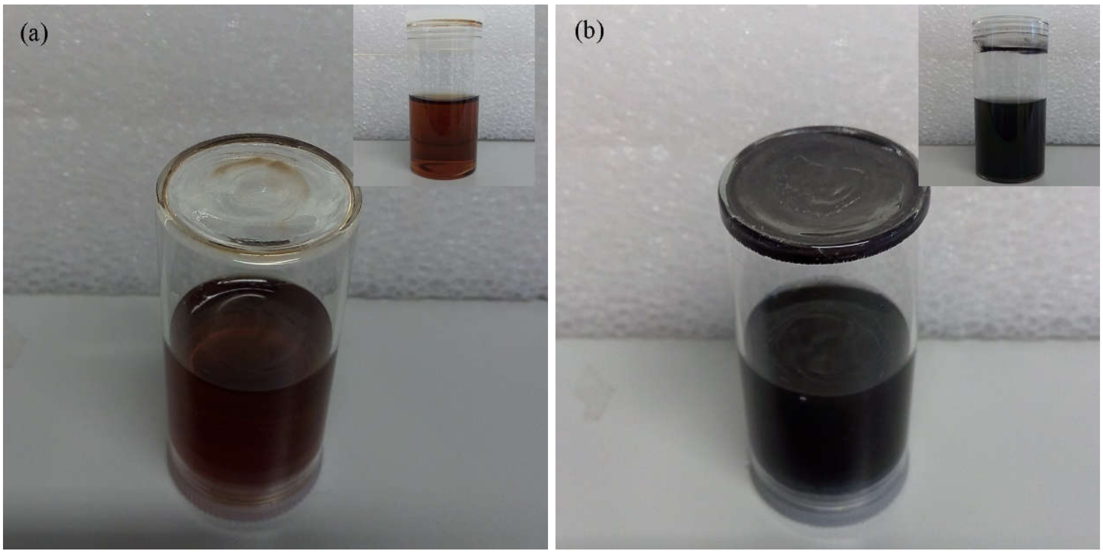

Figure 5.1 Photograph comparing the dispersity of (a) GO and (b) xGnP in DMF solvents after sonication for 12h and 4 days of sedimentation

5.3 In-situ Thermal Reduction of the GO Particles

The GO/DMF mixture prepared from sonication method was poured into an alumina boat and transferred into the oven to dry at 100°C overnight. The alumina boat with dried GO particle was then closed with an alumina substrate and place in a tube furnace. The GO particles were then rapidly heated in the tube furnace to 200°C and calcine for 1h in N_2 atmosphere to simulate the in-situ reduction in polymer environment. The rGO particles were then cooled down to room temperature and collected for measurements.

5.4 In-situ Thermal Reduction of the GO/PVDF Nanocomposites

The GO was transformed into electrically conductive rGO in a stepwise manner by reduction in-situ in the PVDF polymer. The oven dried GO/PVDF nanocomposites were sandwiched between alumina substrates and transferred to the oven to heat at temperature of 120°C, 140°C, 150°C, 160°C, 170°C, 180°C, and 200°C for 1h. The removal of functional groups in the GO powders changes the colour of the nanocomposites from dark brown to black, as seen in Figure 5.2, which indicates a narrowed bandgap in thermally annealed GO powders. Note also that the pure PVDF film retains its natural colour when heat treated under the same conditions.

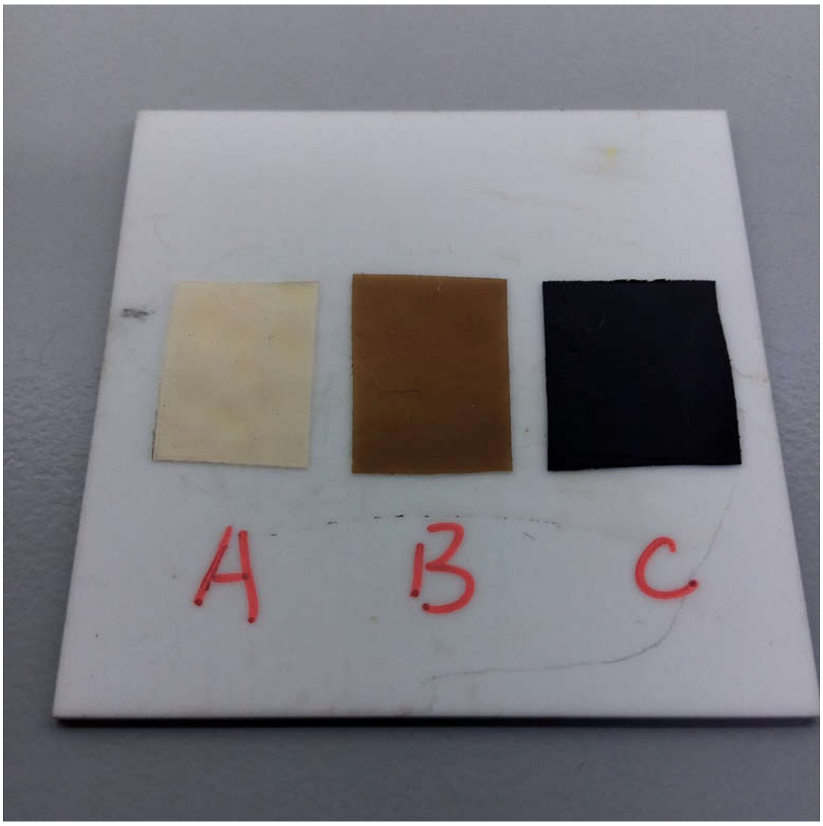

Figure 5.2 Photograph comparing the (A) PVDF film annealed at 200°C for 1h, (B) GO/PVDF film annealed at 100°C for 1h and (C) rGO/PVDF film annealed at 200°C for 1h

5.5 Lapping and Electrode-Sputtering the rGO/PVDF Nanocomposites

The rough surface of the thermally annealed nanocomposites was polished to avoid impact of surface roughness on the electrical properties. Briefly, the sample was cleaned using ethanol and then waxed on a smooth glass substrate. The glass substrate with sample was attached on a jig via vacuum and place on a glass lapping pan of a precision lapping and polishing machine (PM6, Logitech Limited, UK). A mixture of 3μm alumina particles, 1, 2-ethanediol (99.8%, Sigma Alderich, Germany), and water was used as the lapping liquid. The lapping pan is running in 25r/min until the desired thickness is reached. The lapped and polished samples were cut with a sharp knife into a roughly 1cm*1cm squares. The samples were then sandwiched by a sample holder with ϕ1mm round hole and placed in a sputter coater (KX575, Emitech, UK) and sputtered with two cycles of Cr for 2min/cycle and one cycle of Au for 2min/cycle. This will result in a Cr layer of 80nm and Au layer of 200nm. The Cr/Au electrode is also sputtered on the other side of the samples.

5.6 Measurement Techniques

The microstructure of the GO, rGO particles as well as the cross-sectional morphology of PVDF and nanocomposites were measured by scanning electron microscopy (SEM). An SEM (FEI Inspect-F, Hillsboro, OR, USA) with acceleration voltage of 20kV and spot size of 5 was used for measurements. The samples were pasted on the conductive sample holder using adhesive carbon tape. Non-conductive sample such as PVDF and nanocomposites were gold sputtered to improve the SEM image quality.

Fourier transformation infrared (FTIR) spectroscopy was used to measure the IR absorption of the GO, rGO, PVDF, and composite samples. The IR spectroscopy based on the theory that the chemical bonds absorb the IR radiation of its characteristic frequency. Hence the structure of a molecule can be interpreted from its IR absorption spectrum. An FTIR spectrometer (Tensor 27, Bruker Optik GmbH, Germany) with an attenuated total reflection (ATR) accessory (Miricale, Piketech, USA) was used to capture the IR spectra. A ZnSe crystal was used as the IR optic material. The incident angle of the IR beam was 45°, of which the route is shown in Figure 5.3. Each sample were measured with 32 scans and a resolution of 4cm^{-1}. The wavenumber range was set to 4000-600cm^{-1}. The difference between ATR-IR technique and traditional FTIR is that the detector the ATR-IR mode only measures the IR absorption in the reflected beams rather than the transmitted ones. Hence, ATR-IR is suitable for the measurement for non-transparent materials.

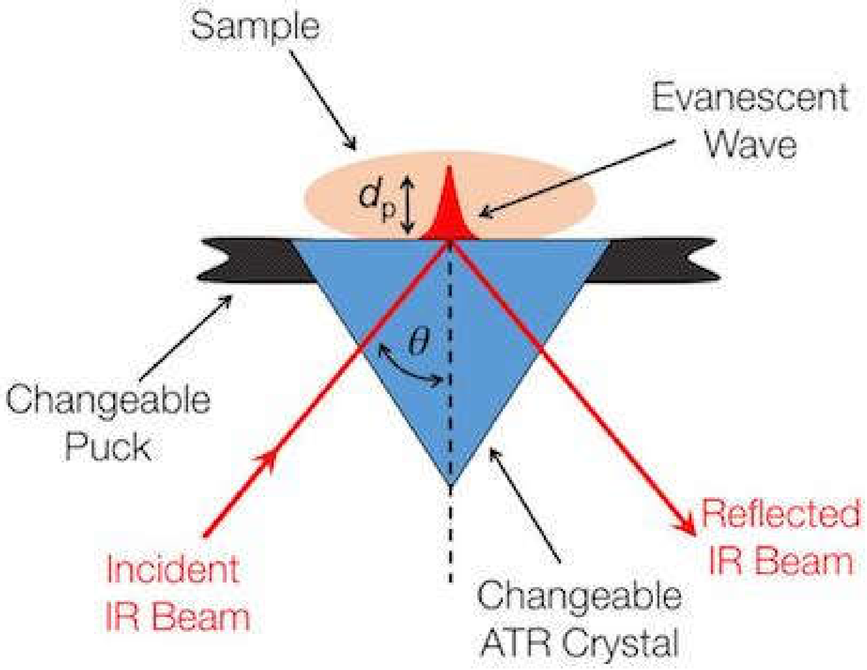
Sample
Evanescent Wave
d_p
θ
Changeable Puck
Incident IR Beam
Changeable ATR Crystal
Reflected IR Beam

Figure 5.3 The route of IR beam in ATR-IR spectroscopy[78]

X-ray diffraction (XRD) was used to measure the phase present in the PVDF and composite samples. According to the Bragg's equation:

$$n\lambda = 2d\sin\theta \tag{5.4.1}$$

where n is the number of diffraction, λ is the wavelength of CuKα radiation, d is the spacing of lattice planes, and θ is the diffraction angle. The diffraction peaks form a pattern that is characteristic of the crystal structure of the sample. An X-ray diffractor

(Bruker D8 Advanced, Bruker, USA) with Cu/Kα as target (λ=1.5405 A). The sample-under-test was fixed on the holder with the tube and detector rotates at rates of -1°/min and +1°/min, respectively. The angle between the tube and detector is 2θ, which was set to be 20° to 90° in this research.

The morphology as well as the local piezoelectricity was characterized via an atomic force microscope (AFM) (NT-MDT, Russia) with a piezo-response (PFM) accessory. The samples were glued on a conductive holder by silver paste and fixed on the AFM stage. A Pt/Ir coated probe with a spring constant of 2.8N/m was used in contact mode with the sample surface. A bunch of laser beam was focused on the backside of the cantilever probe and reflected to a split photodiode detector. While scanning the sample surface, the deflection of the cantilever probe will induce a displacement of reflected laser spot on the detector, hence the fluctuation of the surface morphology can be imaged. This is shown in Figure 5.4. As for the PFM, a DC bias V_{DC} plus an AC voltage V_{AC} is applied from the probe to the sample, the corresponding piezoelectric amplitude Γ_{33} is:

$$\Gamma_{33} = d_{33}V_{DC} + d_{33}V_{AC}\cos(\omega t + \varphi) \tag{5.4.2}$$

where ω is the angular frequency and ϕ is the phase angle indicating the domain orientation.

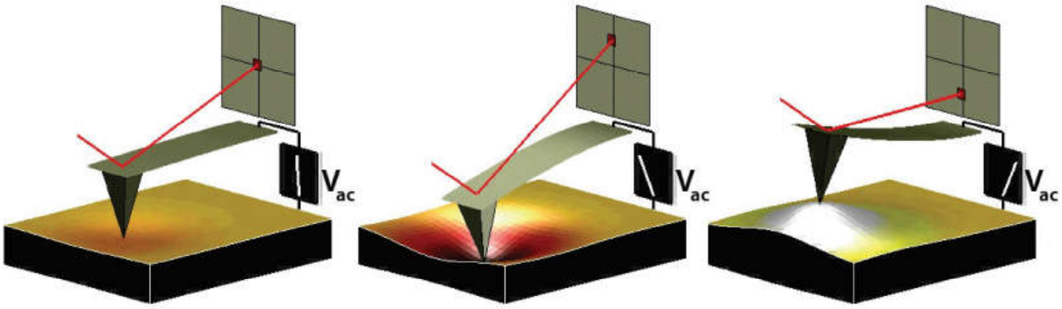

Figure 5.4 Illustration of the AFM/PFM method, with the sample deforms to respond to the applied voltage [79,80]

The electrical parameters of a given material such as leakage current I_0 and effect series resistance R_s can be calculated from the I-V characteristics curves. In this research, the I-V characteristic curves of the PVDF and nanocomposites were measured by a source meter (Keithley 2400, Keithley, USA). The samples with ϕ1mm Cr/Au electrodes on both surfaces was perpendicularly fixed on a glass substrate with epoxy and wired with silver pasted. A voltage sweep from -50V to 50V to the sample was conducted via a source meter (Keithley 2400, Tektronix, UK) and the corresponding current is also measured by the source meter. The data is processed via a built-in I-V sweep program (Tektronix, UK) in LabVIEW 9.0.

The dielectric behaviour of PVDF and the nanocomposites were measured by the impedance method. An impedance analyser (HP4294a, Angilent Technology, USA) with a customized fixer was used capture the impedance spectra. Before measuring the sample, the testing system is calibrated at open circuit, short circuit, and with a resistive load. The experiment was processed at room temperature and an excitation bias of 500mV was used. The testing range was between 50Hz to 50MHz.

The strong field dielectric performance of PVDF and the nanocomposites were measured by a ferroelectric hysteresis tester (NPL, UK) composing of a function generator, a voltage amplifier and a source meter. The ferroelectric hysteresis tester is controlled by a LabVIEW 9.0 program. The samples with ϕ1mm Cr/Au electrodes on both surfaces were clamped by two conductive tips in contact with the sample electrode and fully immersed in silicon oil. An alternating voltage is applied through the voltage amplifier to the sample and the current response I is captured by the source meter. The charge displacement D within an individual period t_1 to t_2 is then defined as:

$$D = \int_{t_1}^{t_2} I dt \tag{5.4.3}$$

In ferroelectrics, the dipole switching behaviour can dominate the dielectric response of the material, hence the charge displacement D is also regarded as polarization P.

Chapter 6 Modelling the Dielectric Behaviour of a Composite

6.1 Introduction

It is well-known that the dielectric response of a composite is directly dependant on the content and electrical properties of the inclusion material. The challenge is to establish a model to describe the relation between dielectric behaviour of the composite and the inclusion/matrix interaction. In this chapter, we will develop a model concerning the dielectric behaviour that can be widely explored in composites with a wide selection of inclusion species. As a composite always composes a matrix far more insulating than the inclusion, it is possible to assume the inclusion is in a permanently percolated condition. This simplifies a composite to a conductor/insulator diode, facilitating modelling its dielectric behaviour using Schottky junction theory.

To accomplish this task, this chapter is organized as follows. We start from a development of classic Schottky junction theory to describe the capacitance behaviour of a conductor/insulator device. This theory will be applied to develop a model for the dielectric behaviour of a conductor/insulator composite. Then, the structure and morphology of the rGO particles and rGO/PVDF nanocomposites is studied. Finally, the electric behaviour of the rGO/PVDF nanocomposites, such as the I-V and impedance response, will be measured and discussed with the model.

6.2 Schottky Junction Theory and Device Capacitance

An intimate contact between metal and insulator can lead to two kinds of junctions, ohmic junction or Schottky (rectifying) junction.[81] For Ohmic junction, there is no energy barrier for charge flowing from insulator to metal or vice versa so that a linear dependence of current I on voltage V can be expected. While for Schottky junction, charges can flow freely in only one direction as a transfer barrier exists in the other. This on-off characteristic makes the Schottky junction an important component in heterostructure based devices.

Figure 6.1(a) shows the band diagram of a conductor and an insulator, with E_c is referred to the bottom of the conduction bands while E_v is referred to the top of the valence bands and E_0 is the reference energy level of the free space. An important concept in the band theory is the Fermi level E_F which is defined by Fermi-Dirac equation as:[82,83]

$$f(E) = \frac{1}{\exp\left(\frac{E-E_F}{kT}\right)+1} \tag{6.2.1}$$

where f(E) is the probability of a particle possessing energy E, k is the Boltzmann constant and T is temperature in Kelvin. At $E=E_F$, f(E)=1/2, this defines the Fermi level as a statistical concept that the probability of a particle possessing this energy is 50%. At T=0K, f(E)=1, this also defines Fermi level as the top of the occupied levels at T=0 K.[84] The concept of Fermi level defines the carrier species and density for an insulator material. A E_F closer to E_c indicates the electron is the predominant carrier while a E_F closer to E_v indicates the hole is predominant. An intimate contact, defined as contact without gap, between conductor and insulator will equalize their Fermi levels, which will accordingly lead to a band distortion in the insulator as shown in Figure 6.1(b). This due to the charge transfer phenomenon where electrons are removed from the high E_F side and appear in the low E_F side. The Fermi level position defined electron (n) and hole (p) density on the junction surface can be described as:

$$n = N_c \exp(-\frac{E_c - E_F}{kT}) \tag{6.2.2}$$

$$p = N_p \exp(-\frac{E_F - E_v}{kT}) \tag{6.2.3}$$

where N_c/N_p is the effective density of states on the E_c/E_v, k is the Boltzmann constant, and T is the temperature in Kelvin.[81,85] The difference between E_c and E_F is the Schottky barrier Φ_B preventing reverse diffusion of electrons.

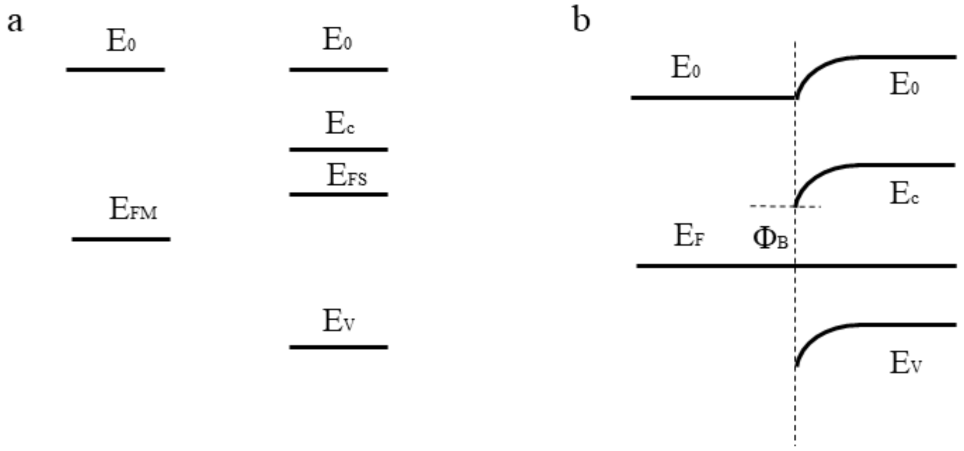

Figure 6.1 Electrical structure of a metal and a semiconductor (a) before contact and (b) after contact

A more relevant discussion to our research is the charge transfer phenomenon of a Schottky junction with respect to the applied bias V. The most significant phenomenon at the junction when V is applied is the shifting of E_F. A reverse V applied through insulator to metal always down-shifts the insulator E_F due to electron extraction while a forward V in turn up-shifts the insulator E_F due to electron injection. Therefore, equation (6.2.2) and (6.2.3) can be modified with respect to V as:

$$n = N_c \exp(-\frac{E_F - E_v - eV}{kT}) \tag{6.2.4}$$

$$p = N_p \exp(-\frac{E_c - E_F + eV}{kT}) \qquad (6.2.5)$$

Equation (6.2.4) and (6.2.5) describes a capacitive behaviour of the Schottky junction, which means the junction can act as a charge blocking component for the conductor/insulator device. The surface bias V also induce a charge limited current I at the junction, which is defined as:

$$I = I_0(\exp(\frac{eV}{kT}) - 1) \qquad (6.2.6)$$

where I_0 is the diode leakage current, which is an intrinsic value to the insulator and is defined as:

$$I_0 = AA^*T^2 e^{-\frac{\phi_B}{kT}} \qquad (6.2.7)$$

where A is the diode area and A^* is the Richardson constant.[81,86] Equation (6.2.6) is valid for both forward and reverse bias, which can be used to describe the rectifying phenomenon of a Schottky diode device.

We now apply the Schottky junction theory to a more specific condition, an insulator sandwiched by two pieces of conductor, which is known as MIM diode.[87] If the a thin (≤10nm) insulator layer is considered, then a quantum tunnelling may occur which will lead to a large current due to direct conductor to conductor travelling of charges.[88] While, if a wide insulator layer is considered, then the direct tunnelling of charges can be inhibited and the current is also a space charge limited current as described in equation (6.2.6).[89] As the conductor/insulator/conductor structure resembles a capacitor, the theory package of Schottky junction can be applied to study the capacitor dielectric behaviours. Considering only electrons under a forward bias, the carrier density change ΔN with respect to V can be described as:

$$\Delta N = N_0\left(\exp\left(\frac{eV}{kT}\right)-1\right) \tag{6.2.8}$$

where n=N_0 is the Fermi level defined carrier density. Therefore, the charge density at the junction is defined as:

$$\delta = e\Delta N = eN_0\left(\exp\left(\frac{eV}{kT}\right)-1\right) \tag{6.2.9}$$

This layer of negative charge in the insulator can form a Schottky capacitance C with the mirrored positive charge on the conductor surface, which can be defined as:

$$C = \frac{A\delta}{V} = \frac{AeN_0}{V}\left(\exp\left(\frac{eV}{kT}\right)-1\right) \tag{6.2.10}$$

This equation bridges the gap between Schottky effect and the device capacitance, which establishes the fundamentals for modelling the conductor/insulator composite.

6.3 Modelling of the rGO/PVDF heterointerface

The structure of a conductor/insulator composite can be described by the diode model indicated in Figure 6.2(a). The diode is constructed by three identical metals (M_1, M_2, M_3) and an insulator (In) in intimate contact, and all junctions are assumed to be Schottky junction. Regarding M_1 as the system electrode, then M_2 and M_3 can resemble the effect of inclusion particles. A bias V applied through M_1 down-shifts the system Fermi level causing electron to be extracted from the Insulator. Due to the equalization of Fermi level, the bias V is simultaneously applied on the surface of M_1, M_2, and M_3, resulting in the device current $I=I_1+I_2+I_3$, where

$$I_1 = I_2 = I_3 = I_0\left(\exp\left(\frac{eV}{kT}\right)-1\right) \tag{6.3.1}$$

The magnified I by M_2/In and M_3/In indicates that the insertion of M_2 and M_3 can be regarded as an effective expansion M_1/In area. This cooperating manner indicates that inclusion particles can enhance composite system capacitance by providing additional charge blocking interfaces. This effect is shown in detail in Figure 6.2(b). Assuming a composite capacitor possessing an electrode area A_0, volume U, and inclusion volume fraction f. The inclusion particles possess a total effective surface area A, which is defined as the sum of surface area projected to the electrode surface. With the findings in Figure 6.2(a), the composite resembles an equivalent capacitor with $A+A_0$ as the electrode area and $(1-f)U/(A+A_0)$ as capacitor thickness. Assuming $A_0 \ll A$ and $f \ll 1$, which is the case for most high permittivity composites with nano-sized inclusions, the electrode area of the equivalent capacitor can be simplified as A while the thickness as U/A. This means for high permittivity composites, the dimension of inclusion particles can have a predominantly impact on the system dielectric response.

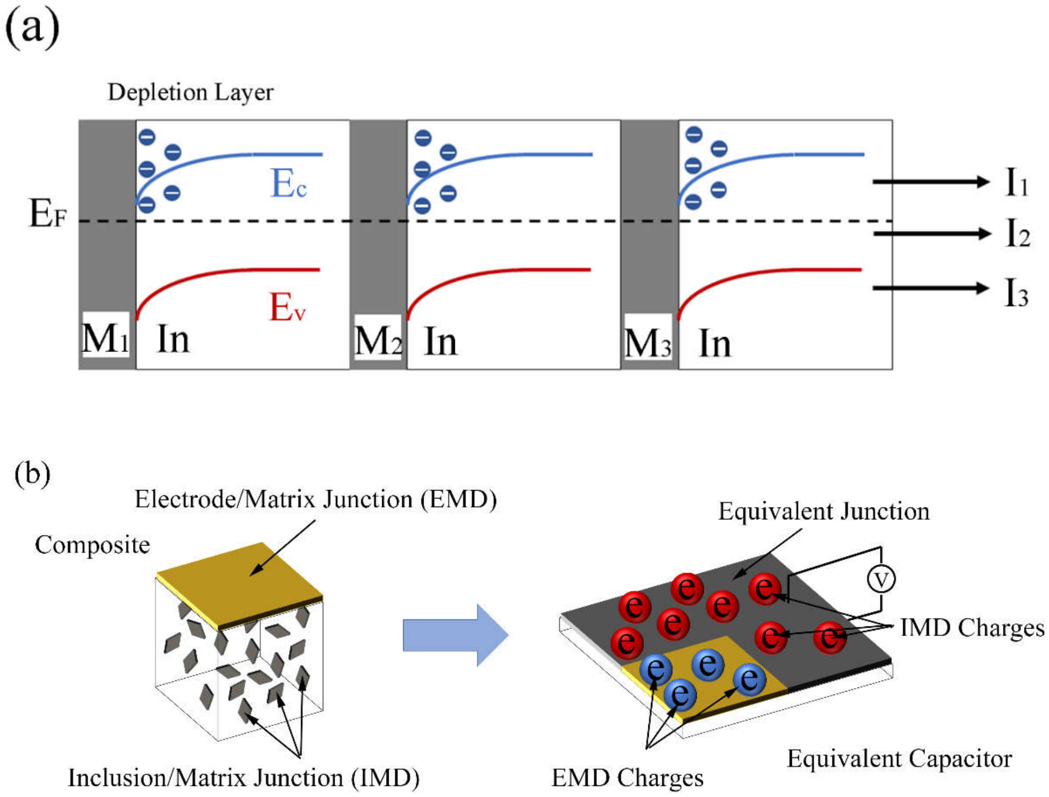
(a)
Depletion Layer
EF
Ec
Ev
M1
In
M2
In
M3
In
I1
I2
I3
(b)
Electrode/Matrix Junction (EMD)
Composite
Inclusion/Matrix Junction (IMD)
Equivalent Junction
V
IMD Charges
e
EMD Charges
Equivalent Capacitor

Figure 6.2 (a) a diode model resembles a conductor/insulator type composite and (b) illustration for the effective expansion of composite system electrode by the addition of inclusion particles

We use the equivalent structure to study the dielectric behaviour of the conductor/insulator composite. An alternating field is applied across the equivalent structure resulting in a junction potential φ on the electrode, the C with respect to φ can be derived from equation (6.2.10) as:

$$C = \frac{AeN_0}{\varphi}\left(\exp\left(\frac{e\varphi}{kT}\right)-1\right) \tag{6.3.2}$$

Analogously, we could define the capacitance of a pure matrix with electrode area A_0 as:

$$C_0 = \frac{A_0eN_0}{\varphi}\left(\exp\left(\frac{e\varphi}{kT}\right)-1\right) \tag{6.3.3}$$

By comparing equation (6.5.3) and (6.5.4), we define the magnification coefficient υ as:

$$\nu = \frac{C}{C_0} = \frac{A}{A_0} \tag{6.3.4}$$

The definition of υ demonstrates the origin of improved dielectric permittivity is the expanded electrode area contributed by the formation of inclusion/matrix junctions. The increase in the number of inclusion/matrix junctions lead to a higher A, hence the inclusion volume fraction f can have a straightforward impact on the composite dielectric response. However, the impact of f may not always be linear. Consider the simplest form, a composite with identical spherical conductors, the effective junction area A=nπr^2 where n is the number of junctions and r is the sphere radius. In this case, the increase in f could linearly increase the dielectric response. While for composites with randomly dispersed platey conductors, the orientation angle may induce a non-linear dependence of system dielectric response on f. Define the effective area of an individual platey conductor as:

$$A_i = S_i \cos\theta \tag{6.3.5}$$

where S_i is the area of the conductor and 0≤θ≤π, the total effective junction area A is then:

$$A = S_1 \cos\theta_1 + S_2 \cos\theta_2 + \cdots + S_n \cos\theta_n \tag{6.3.6}$$

It is obvious that the set $S_{fn}\cos\theta_n$ is discrete, which means it could follow a normal distribution if n is large enough. Therefore, we define the expectation of set $S_n\cos\theta_n$ as S_{exp}, then equation (6.5.7) can be rewrite as:

$$A = nS_{\exp} \tag{6.3.7}$$

Combining equation (6.3.6) and (6.3.7), it can be indicated that for composite with isotropic inclusions, the increase of system dielectric response may be non-linear at small inclusion volume fractions.

By understanding the origin of improved dielectric response, it is still important to know that of loss to completely describe the dielectric figure of a composite. To start, we show the electric field across the equivalent structure E* is given by:

$$E^* = \frac{\varphi A}{U} \tag{6.3.8}$$

E* represents the local electric field between the inclusion particles, hence equation (6.3.8) indicates that the inclusions magnifying dielectric response can simultaneously magnify the local electric field. This finding is analogous to the simulation results reported in the literatures. [42,90-92] For an external field E, E*>E, which means the strong field dielectric behaviour occurs at weaker field reducing the dielectric strength of the composites. This initially explains the contradict between high dielectric response and high dielectric strength. To describe the loss in detail, we studied the interaction between adjacent inclusions as shown in Figure 6.3. According to the figure, we can define a $\omega = t/2$ as the critical depletion length where the spacing is fully populated by charge carriers, the corresponding φ is then defined as critical potential φ_c. At $\varphi<\varphi_c$, $\omega<1/2t$ which means depletion layers of M_2/In and M_3/In are well isolated by free space and the device is an ideal capacitor. While at $\varphi>\varphi_c$, $\omega>1/2t$ would differentiates E_c in the interference area as indicated by the dash line in Figure 6.3. This would populate the interference area with carriers of mirrored charge hence induces a tendency for carriers to recombine to re-establish equilibrium. Assuming the number density at φ is $n(\varphi)$ and that at φ_c is $n(\varphi_c)$, their difference $\Delta n = n(\varphi) - n(\varphi_c)$ defines a pseudo-leakage to the system due to the loss in carriers on the junction surface. As the system always retains to the equilibrium after carrier recombination, its discharge energy J_d is then governed by $n(\varphi_c)$, which is:

$$J_d = \frac{1}{2} Aen(\varphi_c)\varphi \quad \varphi \geq \varphi_c \tag{6.3.9}$$

As energy efficiency η is defined as $\eta=J_d/J$ where $J=J_d+J_{loss}$, the carrier recombination induced pseudo-leakage can be described as:

$$\eta = \begin{cases} 1 & \varphi < \varphi_c \\ n(\varphi_c)\exp\left(-\dfrac{e\varphi}{kT}\right) & \varphi \geq \varphi_c \end{cases} \tag{6.3.10}$$

Equation (6.3.10) reveals an exponentially decay of η after carrier recombination occurred, which also indicates it is insufficient to reduce the leakage by solely isolate the inclusion particles.

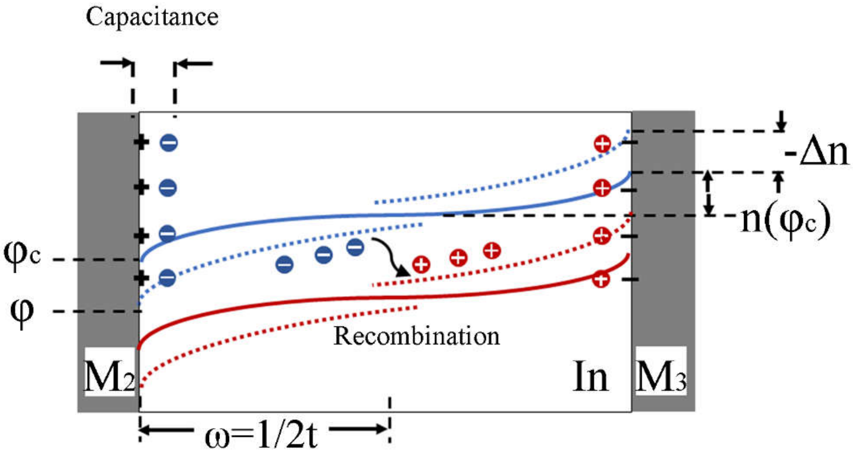

Figure 6.3 Illustration of carrier recombination induced pseudo-leakage.

To sum up, our model suggests that composite capacitors can benefit from inclusion particles with high surface area as they contribute to a large A. This accordingly grants composite a high effective dielectric permittivity ε, which is in good agreement with the experimental data reported in composite with graphene and carbon nanotube particles.[51,57,93,94] However, inclusions with large surface area also increases the matrix filling ratio,[92] which reduces the inter-inclusion spacing causing a smaller ω_c. This suggests composites with a higher ε are more likely to exhibit high loss and possess a smaller dielectric strength.

6.4 Morphology and Structure of rGO and rGO/PVDF Nanocomposites

In this section, we will characterize the microstructure of rGO particles and the rGO/PVDF nanocomposites.

The structure of GO and rGO particles can be characterized by the XRD, which is shown in Figure 6.4(c). The XRD results indicate a multilayer nature of individual GO sheet with an interlayer spacing significantly increased from ~3.4Å of graphite to ~8.6Å after oxidation, this is due to intercalated H_2O molecules between GO lattice planes after oxidation.[95,96]. Figure 6.4(b) and Figure 6.4(c) show the SEM image of GO and rGO particles. The rGO particles were thermally reduced in N_2 atmosphere at 200°C for 1h to simulate the in-situ reduction in polymer environment. Compared to the rGO particles, the GO particles show stronger agglomeration due to large Van der Waals force between surface functional groups. These results indicate the GO particles are functional groups abundant, which may possess a good dispersity in the DMF solvent.

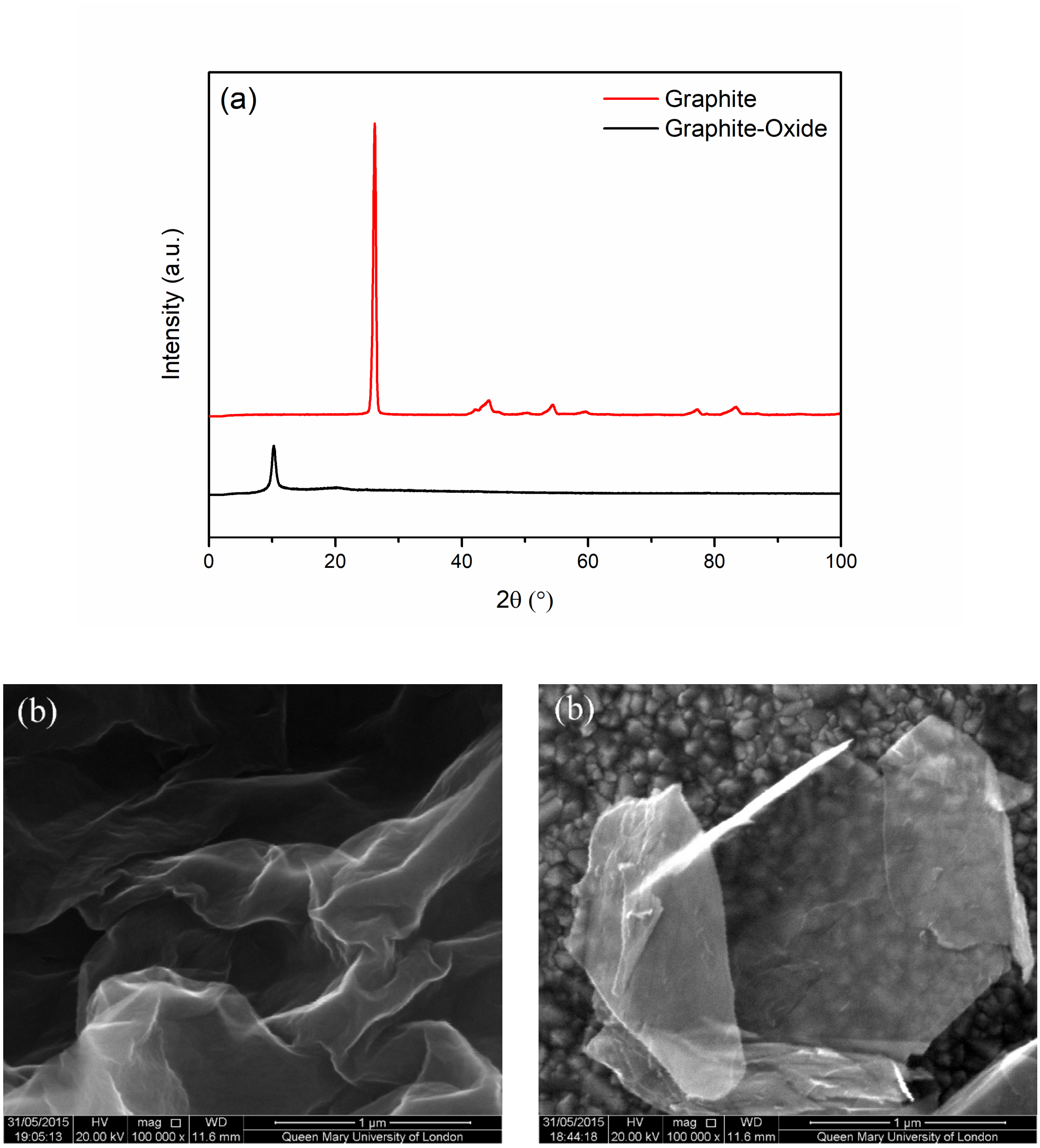

Figure 6.4 (a) X-ray diffractions for raw graphite and graphite-oxide prepared via Harmmer's method, and Morphology of (b) GO particles and (c) rGO particles reduced at 200°C for 1h in N_2 atmosphere

Figure 6.5(a) shows the ATR-IR spectra of the GO and TRGO, respectively, which indicated the removal and reaction of varies functional groups. The GO spectrum was contributed mostly by the O-H stretching (3050cm^{-1} to 3800cm^{-1}) together with C=O (1725cm^{-1}), C-O-C (1160cm^{-1}), and C-O (1080cm^{-1} and 1045cm^{-1}), indicating the existence of hydroxyl, ether, and carboxyl groups. [97-99] After thermal reduction at 200° C, the TRGO spectrum was carbonyl moieties dominated and differed from the GO spectrum in that the broad peak at 3050cm^{-1} to 3800cm^{-1} was disappeared, which was in accordance with the results observed in the literature. The difference between GO and rGO spectrum indicated that while 200°C was sufficient to remove hydroxyl groups, the carbon moieties will remain after reduction due to their increased thermal stabilities. In addition, reactions between functional groups were observed. The peak at 1620cm^{-1} in GO spectrum represented the C=C stretching, which was shifted to 1540cm^{-1} after thermal reduction corresponding to the restoration of conjunctive network of aromatic groups in the carbon backbones.[97,98] Moreover, ether group, which was rarely found in GO, expanded in amount in rGO corresponding to the increased intensity of 1160cm^{-1} peak due to the reaction between desorbed water and carboxyl groups. Furthermore, the newly appeared peaks at 2980cm^{-1}, 2880cm^{-1}, and 1380cm^{-1} confirmed the formation of C-H bond served as defects on the carbon backbones, which was a result of the removal of hydroxyl groups.

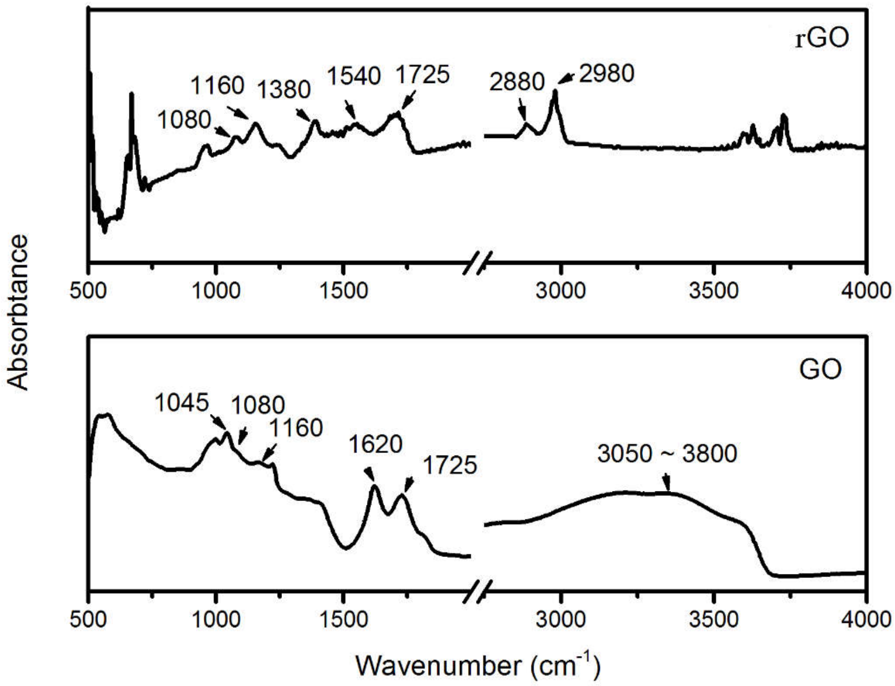

Figure 6.5 ATR-IR spectra for GO and rGO particles reduced at 200°C for 1h.

Figure 6.6(a) and (b) compare the cross-section structure of (a) an as-casted and (b) a 200°C reduced rGO/PVDF nanocomposite. Both samples were frozen at -18°C in a freezer and broken by hand to avoid cutting scalps from affecting the morphology. As for the as-casted sample, the cross-section morphology exhibits large roughness. This could be a sign of high amorphous phase content in the as-casted sample causing high plastic deformation at break. In comparison, the 200°C reduced sample cross-section exhibits a brittle fracture which may indicate a high crystallinity. The bulk density of 200°C reduced sample were measured via Archimedes' method and averaged between 3 samples, which was found to be 1.62 g/cm^3 corresponding to 0.96 of the theoretical value. Figure 6.6(c) shows the cross-section of a pure PVDF annealed at 200°C. Analogous to the 200°C reduced nanocomposite sample, the pure PVDF annealed at 200°C also exhibits a brittle fracture. But the morphology is smoother for pure PVDF compared to the 200°C reduced nanocomposite. This may be corelated to the addition of rGO, which will be discussed in the following chapters.

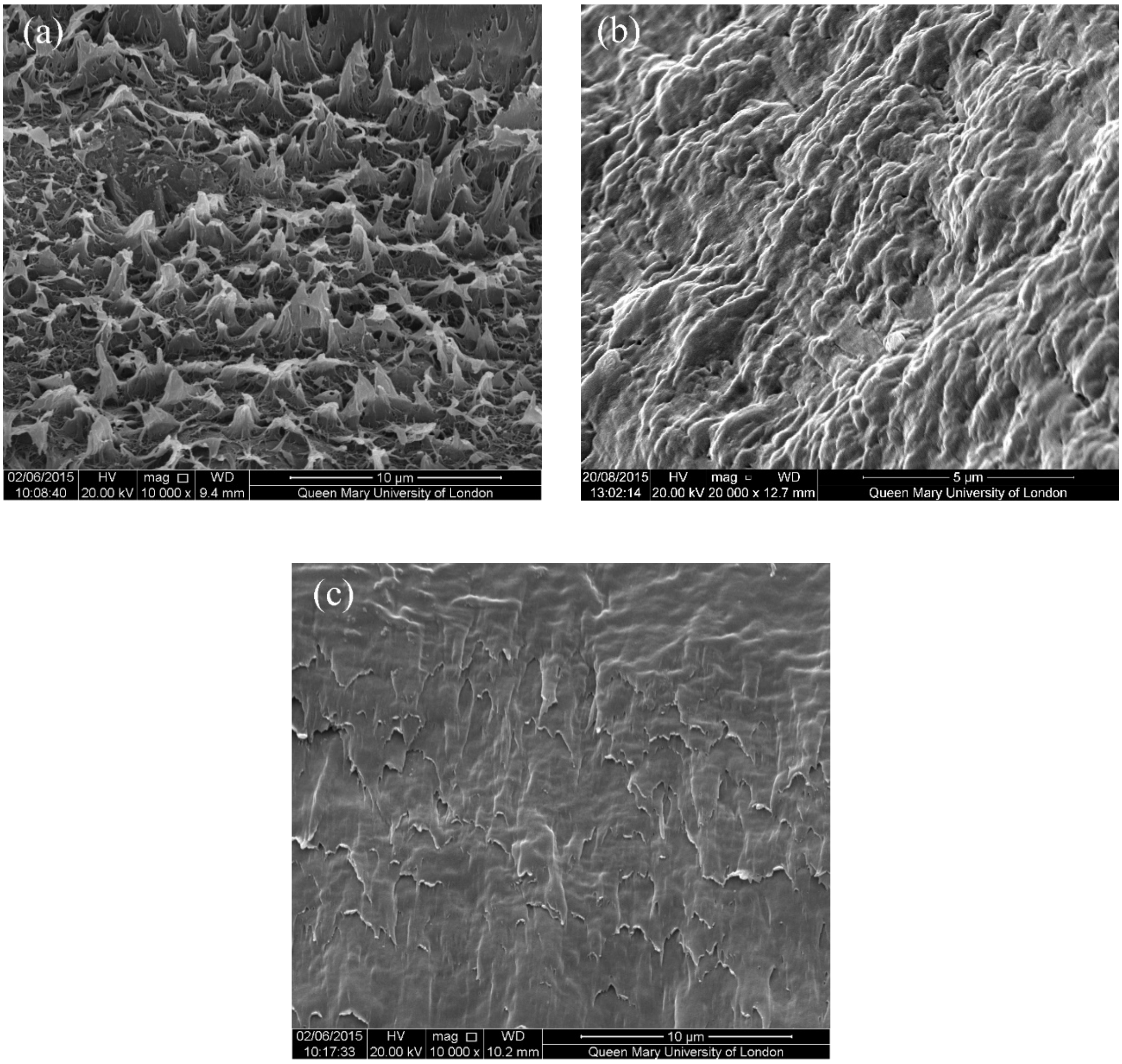
(a)
02/06/2015 10:08:40 | HV 20.00 kV | mag 10 000 x | WD 9.4 mm | 10 µm | Queen Mary University of London
(b)
20/08/2015 13:02:14 | HV 20.00 kV | mag 20 000 x | WD 12.7 mm | 5 µm | Queen Mary University of London
(c)
02/06/2015 10:17:33 | HV 20.00 kV | mag 10 000 x | WD 10.2 mm | 10 µm | Queen Mary University of London

Figure 6.6 (a) SEM image of (a) as-casted GO/PVDF nanocomposites, (b) rGO/PVDF nanocomposites reduced at 200°C for 1h, and (c) pure PVDF annealed at 200°C for 1h.

6.5 I-V Characteristics of the rGO/PVDF Nanocomposites

To demonstrate the effect of inclusion/matrix heterojunction, we measured the I-V curves for a group of rGO/PVDF nanocomposite devices with varies of rGO content and reduced at 200°C as well as a pure PVDF device. The nanocomposites used were polished and sputtered with Φ1mm chrome/gold electrodes as described in Chapter 5. A sourcemeter (Keithley 2400, Tektronix, UK) was used to sweep a voltage from -50V to 50V to the samples. The experimental data were collected via a Keithley built-in I-V sweep program in Labview 9.0 (National Instrument, USA).

Figure 6.7(a) shows the I-V curves of PVDF and rGO/PVDF nanocomposites. To start, the I increases with increasing rGO content. For devices with 2.0 vol.% and 2.5 vol.% rGO (2.0-rGO@200 and 2.5-rGO@200), their I-V curves exhibit strong non-linearity. These findings are good supports of the existence of a rGO/PVDF heterojunction. Herein, we use the equation (6.2.6) to calculate the electrical parameters from the I-V curves.[81,86] A two-diode series circuit can resemble the I-V response of the sample device, which is shown in insert Figure 6.7(a). The diode 1 is in opposite connection with diode 2, and therefore the overall current response of the system is limited by the Schottky junction at diode1. As for a real device, the junction bias is smaller than that applied due to the effective series resistance R_s contributed by contact, sheet resistance and material dimensions.[100-102] Hence, equation (6.2.4) need to be modified as:[81]

$$I = I_0(\exp(\frac{e(V - R_s I)}{kT}) - 1) \tag{6.4.1}$$

To estimate the R_s, we could use the high V section of the I-V curve where the contribution of R_s to I could be dominant.[103] Similarly, we could also estimate the I_0 from the high V section as at high V, -1 component of equation (6.4.1) could be neglected and a simplified equation can be obtained:

$$\ln I = \ln I_0 + \frac{e(V - R_s I)}{kT} \tag{6.3.2}$$

The calculated results of R_s and I_0 is summarized in Figure 6.7(b). As seen, the I_0 is 4.1×10^{-9}A in the pure PVDF device, which is in the same range as those in the 1.0-rGO@200 and 1.5-rGO@200. With the rGO content increases to 2.0 vol.%, a sharp increase of I_0 to 4.8×10^{-7}A was observed, followed with a further increase to 7.2×10^{-7}A in 2.5-rGO@200. As for the R_s, the value decreases with increasing rGO content, from $3.1\times10^{9}\Omega$ for the pure PVDF to $1.8\times10^{6}\Omega$ for the 2.5-rGO@200. The I_0 is intrinsic to a diode device as defined by equation (6.2.7), hence the only variable is the junction area A. Due to this fact, it is reasonable to attribute the increase of I_0 to the formation of rGO/PVDF junctions. Meanwhile, the increased rGO content providing large junction area also compacts the inter-rGO spacing, this lead to a decreased effective charge tunnelling distance that causes the decreased R_s. Therefore, these findings are in good agreement with the characteristics of the equivalent structure as shown in Figure 6.2, which demonstrates the magnifying effect of rGO/PVDF heterojunction to the system current response.

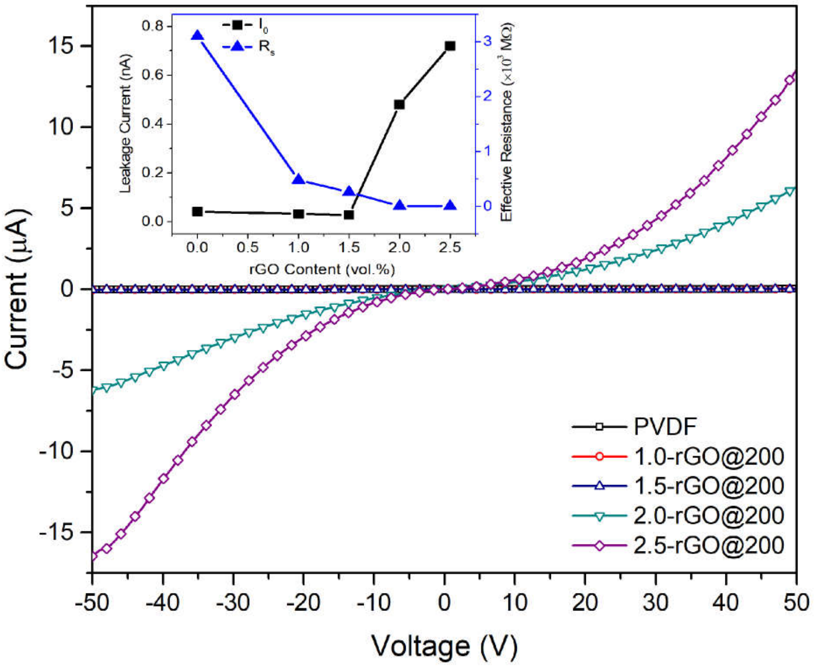

Figure 6.7 I-V curve of 50μm rGO/PVDF nanocomposites coated with φ1mm chrome/gold electrode with different rGO content, in comparison with a pure PVDF, the insert figure shows the fitted results of I_0 and R_s

6.6 Equivalent Circuit of the rGO/PVDF Nanocomposites

The impedance of a material resembles to that of its equivalent circuit. In this section, the equivalent circuits of both pure PVDF and nanocomposites reduced at 200 °C were measured. An impedance analyser (HP4295a, Agilent Technologies, USA) was used to measure the impedance spectra, which is discussed in detail in Chapter 5. The equivalent circuits were simulated from the impedance spectra by Zsimpwin software (Ametek Scientific Instrument, USA).

Figure 6.8(a) shows the Nyquist plots of both pure PVDF and the nanocomposites. As seen, the Nyquist plots exhibit the tendency to close a semi-circle at higher rGO content, which is a sign of the increased impact of the charge transfer resistance R_{ct}. As for the pure PVDF device, we found its impedance response is identical to a single constant-phase-element (Q), of which the impedance Z_{CPE} is defined as:

$$Z_{CPE} = \frac{1}{(j\omega)^n Q} \qquad (6.3.1)$$

where n is a factor between 0 (resistor) and 1 (capacitor), ω is the angular frequency and, and Q is associated to the CPE capacitance.[104] Contrasted to the pure PVDF, we found it is only by assuming a parallel circuit that can the electrical behaviour of the nanocomposites can be reasonably described. As seen, the Q_2 is in series connection with R_{ct} and then connected with Q_1 in parallel, this means the R_{ct}-Q_2 controls the system charge transfer kinetics. The fitting results of the equivalent circuits attribute the introduction of the R_{ct}-Q_2 component to the addition of rGO particles, which is listed in Table 6.6.1. To start, Q_2 is larger than Q_1 and is increasing with rGO volume fraction. This indicates a predominant contribution of Q_2 to the system capacitance, and the capacitance increases with increasing rGO content. Meanwhile, comparing to the quality factor n_1 of Q_1, the n_2 for Q_2 exhibits smaller values, and is decreasing with increasing rGO content. This means the Q_2 component resembles more to a resistor device with increasing rGO content. Therefore, if assigning the Q_2 as the rGO/PVDF heterojunction capacitance, its characteristics with the rGO content are in good agreement with the equivalent structure model in Figure 6.2(b). Combining the results calculated from the I-V curves, we claim the inclusion/matrix heterostructure would dominate the system capacitance of a composites, and the equivalent structure indicated in Figure 6.2(b) can be used in the following sections to study the dielectric behaviour of the rGO/PVDF nanocomposites.

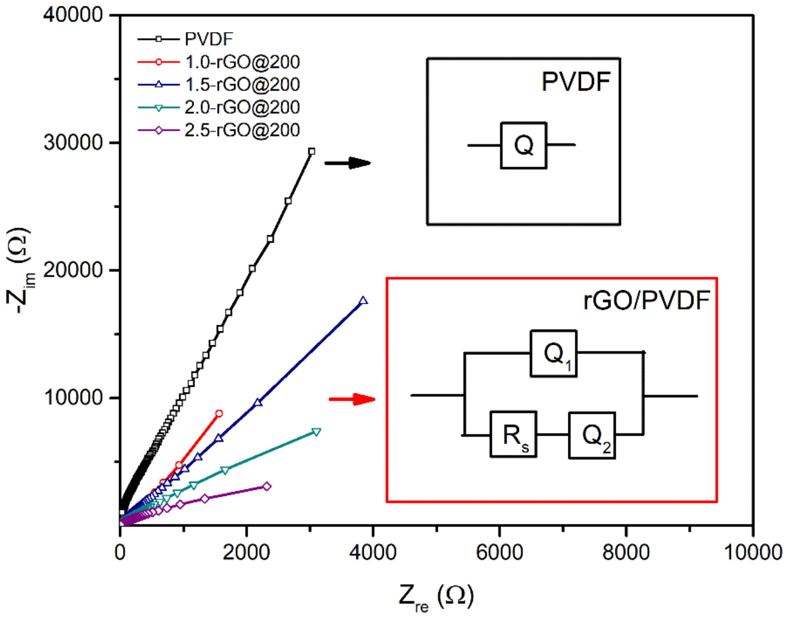

Figure 6.8 Nyquist plot of pure PVDF and rGO/PVDF nanocomposites, and their corresponding equivalent circuits

Table 6.6.1 Equivalent circuit parameters for pure PVDF and nanocomposites

Sample	Geometry	Q_1 ($S \cdot s^n$)	n_1	Q_2 ($S \cdot s^n$)	n_2
PVDF	Φ1mm*40μm	$0.47*10^{-11}$	0.94	-	-
1.0-rGO@200	Φ1mm*40μm	$1.74*10^{-11}$	1	$5.80*10^{-10}$	0.76
1.5-rGO@200	Φ1mm*40μm	$0.84*10^{-11}$	1	$4.38*10^{-10}$	0.74
2.0-rGO@200	Φ1mm*40μm	$1.42*10^{-11}$	1	$3.12*10^{-9}$	0.68
2.5-rGO@200	Φ1mm*40μm	$2.12*10^{-11}$	1	$1.5*10^{-8}$	0.62

6.7 Summary

In this chapter, we proposed a model describing the effect of inclusion/matrix heterojunction on the composite dielectric behaviours. This model is partially discussed with the experimental data measured from both pure PVDF and rGO/PVDF nanocomposites. The findings of this chapter can be summarized as the followings:

1. We suggest the effect of adding inclusion particles as an effective expansion of the electrode area for a composite capacitor device, which explains the improved dielectric response. Besides, we also suggest the carrier recombination between the adjacent inclusion/matrix junctions contributing predominantly to the loss of the composite capacitor.
2. We show the carrier recombination kinetics define a charge density limited discharge energy J_d to the composite device, which indicate the device energy density decreases exponentially with increasing charging field after recombination occurred.
3. We measured the I-V curves as well as impedance spectra of the rGO/PVDF nanocomposites, in comparison with those of a pure PVDF device. These results showed evidences of the existence of the rGO/PVDF heterojunction, which can be good supports to our model.

Chapter 7 Dielectric Behaviour of the rGO/PVDF Nanocomposites

7.1 Introduction

In the last chapter, we have shown good support to the mechanism of inclusion/matrix heterojunctions contributing predominantly to the composite dielectric response. However, there is still a lack of evidence for the charge carrier recombination induced loss. In this chapter, we will measure the dielectric behaviour of the rGO/PVDF nanocomposites and discussed with the model proposed in the last chapter.

This chapter is structured as follows. To begin with, we show the impact of both reduction temperature and rGO content on the dielectric permittivity of the nanocomposites by investigating their properties in the frequency domains. After that, we measured the discharging energy density J_d of the nanocomposites via ferroelectric hysteresis test. The charge carrier recombination induced loss is evidenced by studying the nanocomposite hysteresis loops. By understanding the kinetics of charge storage and loss, we established an explicit relation between composite dielectric permittivity and its discharge energy density. This for the first time makes it possible to design large energy density composite capacitors via tailoring their dielectric responses.

7.2 Dielectric Responses of the rGO/PVDF Nanocomposites

In this section, we investigate the frequency domain of the dielectric permittivity and tanδ of the nanocomposites. The nanocomposite films were polished as described in Chapter 5 and sputtered with ϕ1mm Cr/Au electrode. The frequency domain of the dielectric response is measured by an impedance analyser (HP-4294a, Agilent technology, USA) with a sinusoidal excitation bias level of 500 mV.

Figure 7.1(a) shows the frequency domain of the relative dielectric permittivity ε_r of 1.5-rGO reduced at different temperatures. As seen, while the reduction temperature can have an observable impact on the ε_r of the nanocomposites, the effect is not linear. For instance, the ε_r@1kHz is measured to be around 17 and barely changed between 100 °C and 140 °C, which is almost identical to that of the pure PVDF. Measurable difference of the ε_r is observed for samples reduced above 140 °C, after which the ε_r is increased significantly with increasing temperatures. As seen, the ε_r for 1.5-rGO@150 is 20, which is increased stepwisely to 50 for 1.5-rGO@200. Figure 7.1(b) shows the frequency domain of tanδ at different annealing temperatures for 1.5-rGO. tanδ is defined as the ratio between imaginary and real part of the permittivity and hence is representing the loss of the nanocomposites. Analogous to that of the ε_r, the tanδ only increases at above 140 °C, which indicates a more lossy behaviour for the nanocomposites reduced at higher temperatures. Generally, the tanδ@1kHz is always attributed to the conduction due to travelling charges. While as seen in Figure 7.1(b), a Debye term peak emerges at above 140°C, which can be assigned to the relaxation phenomenon of the nanocomposites. This means the conduction loss might be coupled with the relaxation phenomenon and thus tanδ@1kHz cannot be merely assigned to the leakage of the nanocomposites. Herein, we could correlate the temperature dependence of the dielectric behaviour to the change in effective series resistance R_s of the rGO/PVDF heterojunction. As discussed in Chapter 5, the reduction of rGO can be classified into 2 stages, namely (I) removal of H_2O molecule at $T \leq 140$°C and (II) major removal of oxygen containing group at above 140 °C.[105] As reported, the electrical structure of rGO is closely related to its C/O ratio, and a major removal of functional groups at above 140 °C can lead to a sharp decrease in the C/O and therefore a more metallic behaviour due to the restoration of the sp^2 bonding networks.[106-110] This leads to a higher capacitance via reducing the R$_s$ on the rGO/PVDF heterojunction.

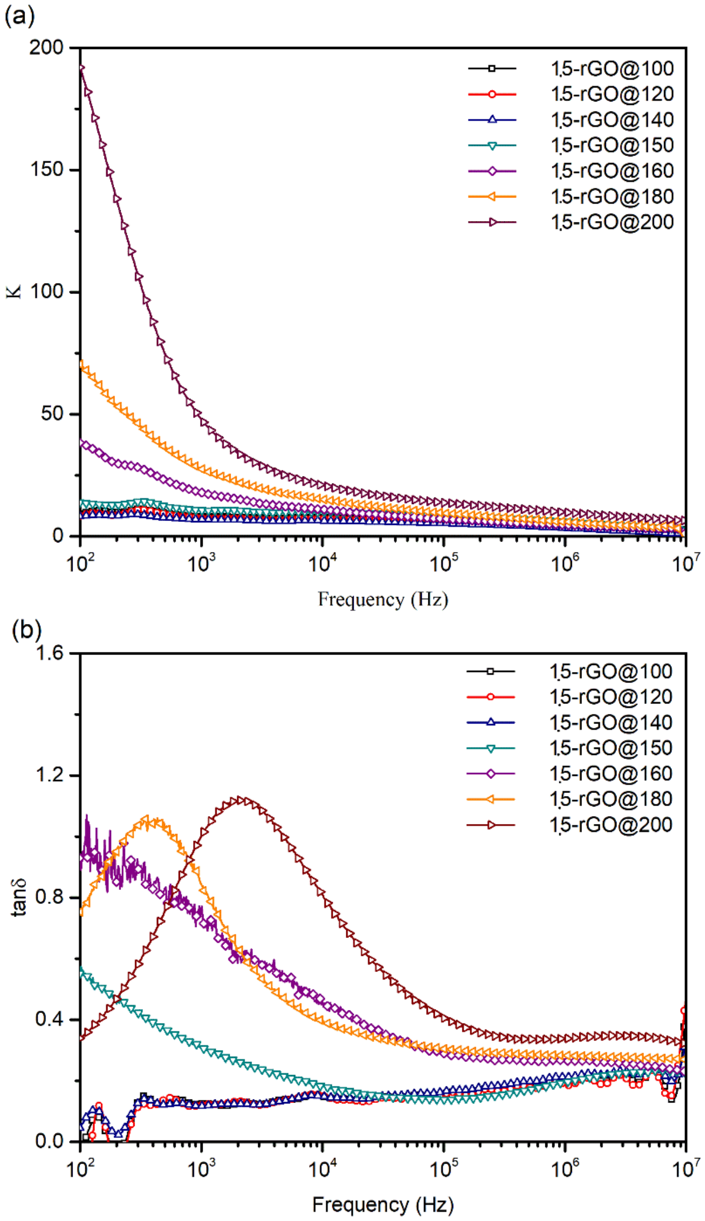

Figure 7.1 Frequency domain of (a) relative dielectric permittivity and (b) tanδ of 0.015-rGO-PVDF nanocomposites reduced at the temperature range from 100°C to 200°C for 1h

Figure 7.2(a) shows the frequency domain of the ε_r of the nanocomposites reduced at 200°C with respect to the rGO content f. As expected, the ε_r increases with increasing f. For instance, at the ε_r@1kHz was measured to be 22 for 1.0-rGO@200, which was increased to 380 at for 2.5-rGO@200. This is a significant increase in ε_r over that of the pure PVDF, for which the ε_r@1kHz was measured to be 11. Figure 7.2(b) shows the frequency domain of tanδ of the nanocomposites with respect to the f. Albeit higher than that of the pure PVDF, the tanδ@1kHz is merely 0.3 for 2.5-rGO@200, compared to that of 0.2 for 1.0-rGO@200. Regarding to the ε_r value as high as 380, the tanδ@1kHz observed in this research is significantly lower than those usually reported (tanδ@1kHz ≥1).[45,51,54,56,111-113] The relation between tanδ and f is defined by the percolation theory as:

$$\tan\delta \propto (f - f_c)^a \tag{7.2.1}$$

where f_c defining the percolation threshold and a is a constant.[114] According to equation (7.2.1), the weak dependence of tanδ on f indicate the rGO content is still away from the percolation threshold. Therefore, it is reasonable to regard the dispersion of rGO as homogeneous.

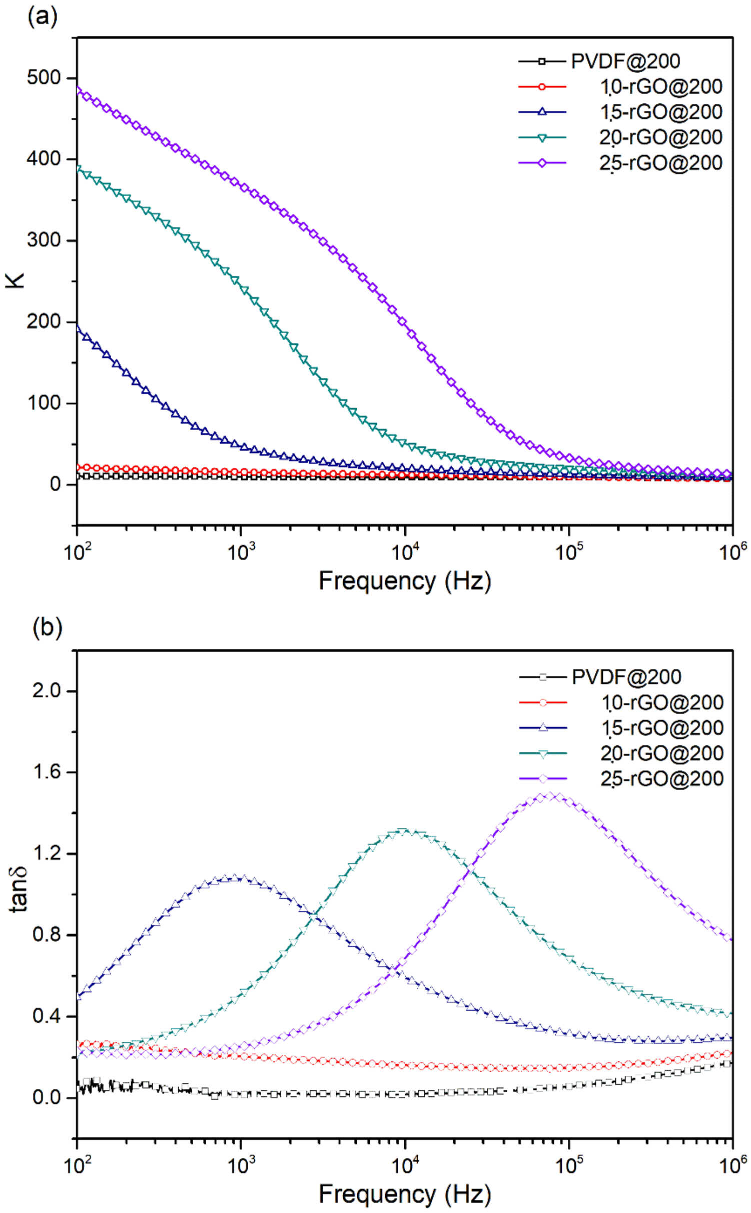

Figure 7.2 Frequency domain of (a) relative dielectric permittivity and (b) tanδ of rGO-PVDF nanocomposites reduced at 200°C for 1h

7.3 Energy Storage Performances of the rGO/PVDF Nanocomposites

In Chapter 6, we suggested composite capacitors possessing higher ε are more likely to exhibit high loss on charging the devices. This has, however, still not been approved by the experimental data nowadays as there is few reports about the energy storage performance for high ε composites. To discuss with the model in Chapter 6, we calculated the discharge energy density and energy efficiency of the rGO/PVDF nanocomposites by measuring their charge displacement vs. electric field (D-E) loops.

Figure 7.3(a) shows the calculated discharging energy density J_d of the nanocomposites, which is calculated as:

$$J_d = \frac{1}{2}\eta\varepsilon E^2 \tag{7.3.1}$$

where η is the energy efficiency and E is the charging field. As indicated, the nanocomposites can possess an enhanced J_d compared to the pure PVDF at weak field. For instance, the J_d of 1.0-rGO@200 is calculated to be 0.002J/cm^3 at 4MV/m, which was increased to 0.012J/cm^3 in 1.5-rGO@200, corresponding to 4 and 24 times increased over pure PVDF under the same field strength. We found the problems preventing nanocomposite capacitors from achieving higher J_d are: (i) too weak dielectric strength E_b, and (ii) rapidly decreasing energy efficiency η. These problems are indicated in detail in Figure 7.3(b) and (c), respectively. Figure 7.3(b) shows the E_b of the nanocomposites defining the maximum charging field of a capacitor. It can be indicated that the addition of rGO decreases the E_b. The pure PVDF is very tolerable to the external field due to its highly insulating nature, and the E_b was found to be 220MV/m in this research. With the addition of rGO, the E_b dropped dramatically to 34MV/m for 1.0-rGO@200, which is 6 times lower than that of the pure polymer. Continuing increasing the f results in an even more reduced E_b. For instance, the E_b for the 2.5-rGO@200 is merely 3MV/m. The weak E_b prohibits a large charging field strength overshadows the high ε merit of the nanocomposites. Figure 7.3(c) shows the energy efficiency of the nanocomposites, which is defined as:

$$\eta = \frac{J_d}{J} \tag{7.3.2}$$

where J is the theoretical energy density. Analogous to that of E_b, the addition of rGO can dramatically decrease the η. For instance, the η of PVDF at 1kV/mm was 0.98, which decreased to 0.69 in 1.0-rGO@200 and further to merely 0.04 in 2.5-rGO@200. Besides, the η shows a strong field strength dependence. Comparing to the pure PVDF exhibiting a linear η drop, that of the nanocomposites (except 1.0-rGO@200) decreases more rapidly in an exponential manner with increasing charging field. According to the model proposed in Chapter 6, the relation between η and E can be described as:

$$\eta = \begin{cases} 1 & E < E_{gate} \\ b\exp(-E) & E \geq E_{gate} \end{cases} \tag{7.3.3}$$

where b is a constant and E_{gate} is the critical field when charge carrier recombination occurs. This equation can be partially approved by the exponential decay of η with increasing E in Figure 7.3(b), which supports the carrier recombination kinetics in contributing to the leakage. The energy storage performance measured in this section provides an experimental demonstration for the correspondence of high ε and high loss, which means high ε composite are not practically suitable for large energy density applications.

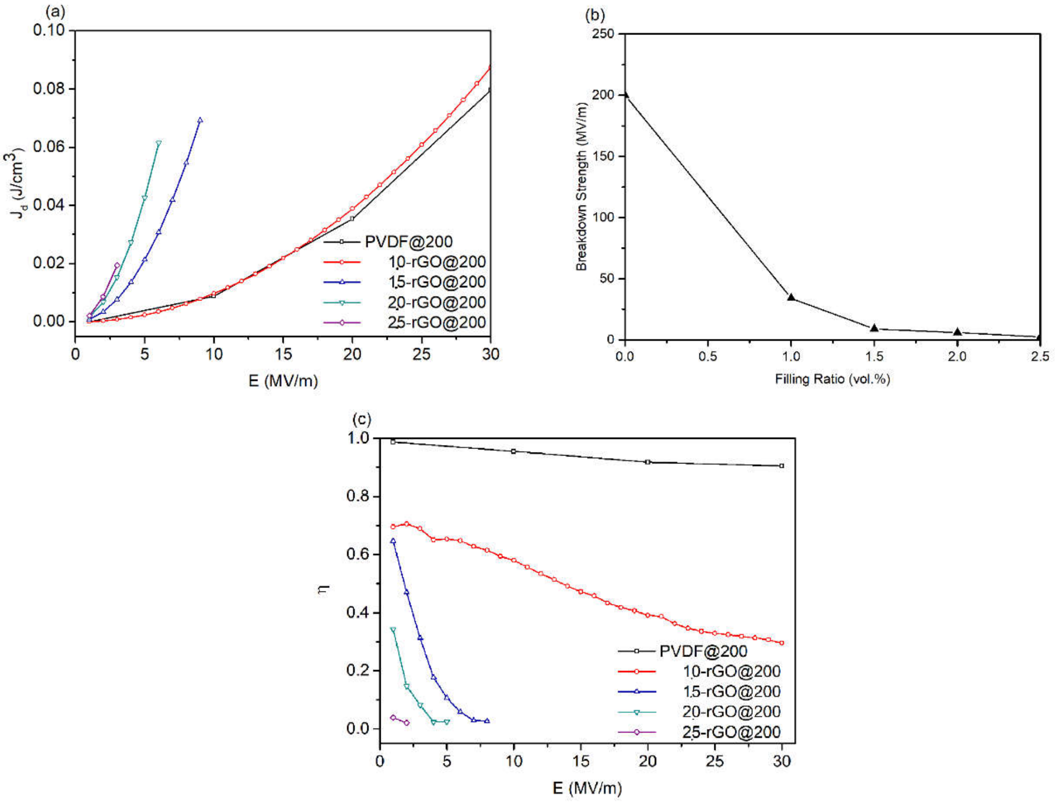

Figure 7.3 (a) discharging energy density J_d, (b) dielectric strength, and (c) efficiency η vs. field strength E for nanocomposites reduced at 200°C with varies of rGO content

The carrier recombination phenomenon can be directly evidenced from the D-E (charge displacement vs. charging field) loops of the nanocomposites. (1.5-rGO@200), as shown in Figure 7.4(a) shows the D-E loops of the 1.5-rGO@200 measured at 1 MV/m, 5 MV/m, and 8 MV/m. As seen, on charging the device at 1MV/m 10Hz, the device exhibits a classic capacitor D-E loop with η=0.65. While on charging the device at 5 MV/m, the D-E loop become flatter with an overcharging section exist on the discharge section. This overcharging phenomenon is enhanced when increasing the charging field to 8 MV/m, resulting in a drop in η from 0.11 (5 MV/m) to 0.02. The overcharging phenomenon was found as electric-field-gated, and the E_{gate} was found to be 2 MV/m. This gating characteristic corresponds to equation (7.3.3), which is an indicator of carrier recombination. The relation between overcharging and carrier recombination is illustrated in detail in Figure 7.4(b). When $E < E_{gate}$, potential on rGO/PVDF junction $\varphi_1 < \varphi_c$ hence no carrier recombination occurs. This resembles charging the device at 1MV/m, with only the ballistically transporting or hopping free carriers contribute to the leakage. When $E > E_{gate}$, $\varphi_1 > \varphi_c$ triggering carrier recombination result in a loss of carrier Δn_1 on the junction surface. On discharging the device, potential drops to φ_2 where $\varphi_2 > \varphi_c$. This will resupply a carrier density of Δn_2 to be recombined until potential drops to φ_c. This resupply of charge carriers resembles a pseudo-charging conduct, hence contributes to the overcharging curve on the D-E loop. The overcharging curve defines the flatness of the device D-E loops causing a sharp drop in η, demonstrating the carrier recombination as a predominant contributor to the leakage of composite capacitor devices.

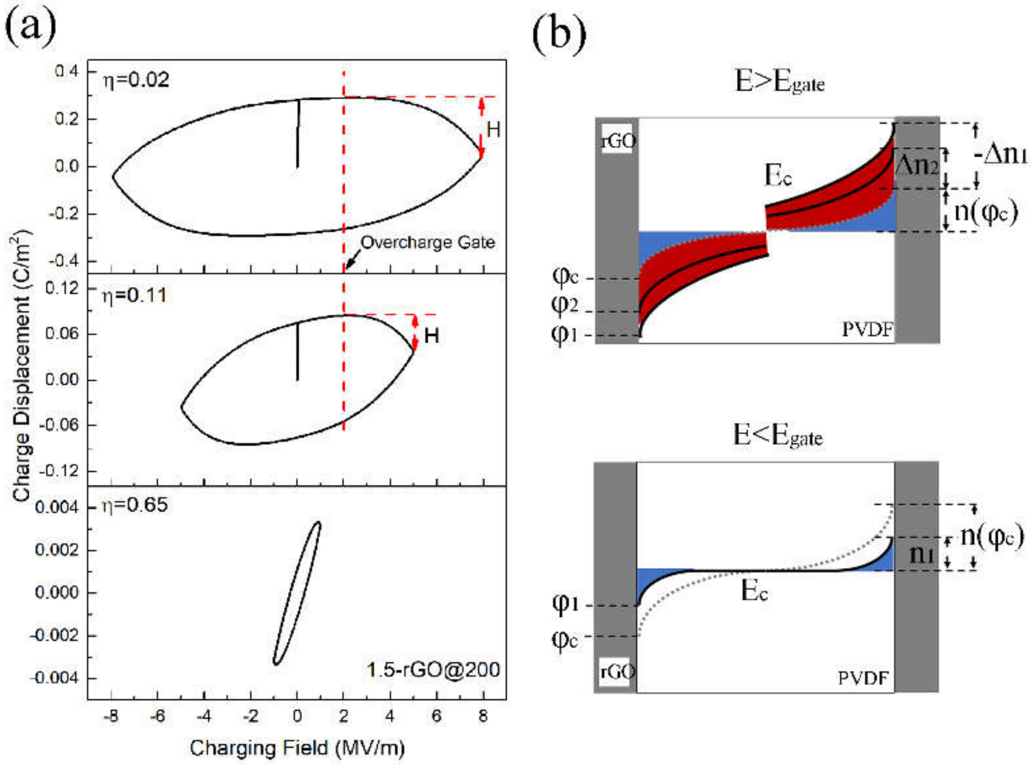

Figure 7.4 (a) D-E loops of 1.5-rGO@200 showing field-gated leakage and carrier recombination induced overcharging effect, and (b) band distortion between rGO particles illustrating the kinetics of carrier recombination

7.4 Modifying the rGO/PVDF Heterojunction for Achieving Large Discharge Energy Density

The carrier recombination kinetics also opens a new route for achieving large energy density in composite capacitors. According to the last section, an increase in ε would simultaneously decrease E_b, therefore a possible strategy one can use to avoid an early breakdown is to reduce the composite ε to increase E_b. However, a significant decrease in ε will in turn degrade the dielectric behaviour of a composite to its matrix. This means further study to balance the ε and E_b is still needed.

Fortunately, the temperature tuneable structure of rGO offers us the opportunity to study the ε-E_b relation. As indicated in section 7.2, the dielectric response of the rGO/PVDF nanocomposites is smaller when reduced at lower temperatures, it is interesting to know how these lower temperature reduced nanocomposites can behave at strong charging field. Figure 7.5 shows the D-E hysteresis loops of the 0.015-rGO nanocomposites reduced at a temperature range from 100°C to 200°C. As seen, increases in D was observed in 1.5-rGO@150 and 1.5-rGO@160, which is measured to be 1.7 μC/cm^2 and 4.1 μC/cm^2, respectively. These results show the enhancement over 1.2 μC/cm^2 of the pure PVDF. Besides, the overcharging phenomenon is not observed when charging the at 50 MV/m and the samples show relatively slimmer hysteresis at stronger electric field compared to that of 200°C reduced.

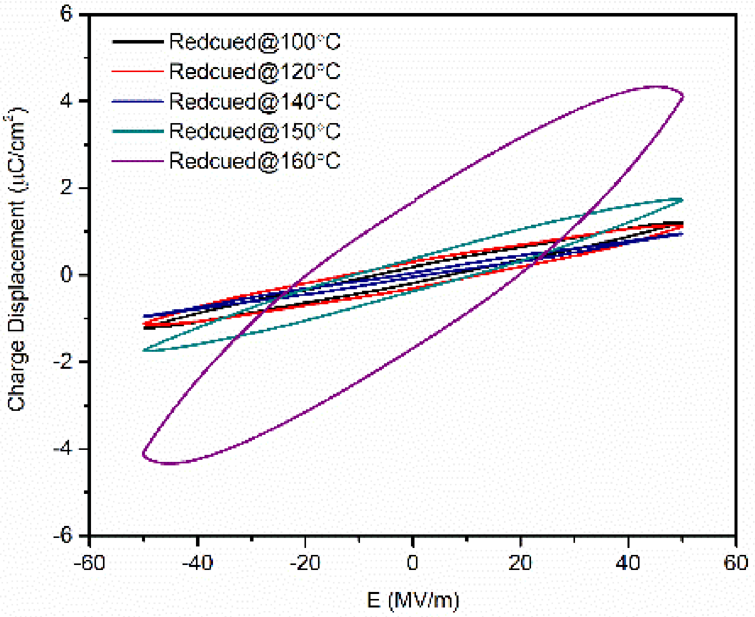

Figure 7.5 D-E hysteresis loops measured at 50MV/m at 10Hz for 1.5-rGO nanocomposites reduced in the temperature range between 100°C and 160°C

The enhanced energy storage performances of the nanocomposites reduced at lower temperatures are shown in Figure 7.6(a), (b), and (c). To begin with, a dramatically enhanced dielectric strength was observed, which is plotted in Figure 7.6(a). For instance, the dielectric strength of 150 °C and 160 °C reduced nanocomposites are 145 MV/m and 70 MV/m, respectively, compared to that of merely 9 MV/m in composite reduced at 200 °C. This enhancement in E_b prolonged the upper limit of the charging field strength, and a J_d is achievable in nanocomposites reduced at lower temperatures. The J_d and η of the 1.5-rGO@150, 1.5-rGO@160 and a pure PVDF are calculated and shown in Figure 7.5(b) and (c). Herein, the η=0.5 was set as the cut-off efficiency. As expected, nanocomposites reduced at lower temperatures can exhibit a higher η. For instance, the η of 1.5-rGO@200 is 0.65 at 1 MV/m, in significant contrast to that of 1.5-rGO@150 and 1.5-rGO@160, which is 0.94 and 0.92 at 10 MV/m, respectively. The reduced loss has led to a more promising J_d. For instance, the J_d of 1.5-rGO@160 is 0.67J/cm^3 at 50MV/m, which is 3 times of that of pure PVDF measured at same condition.

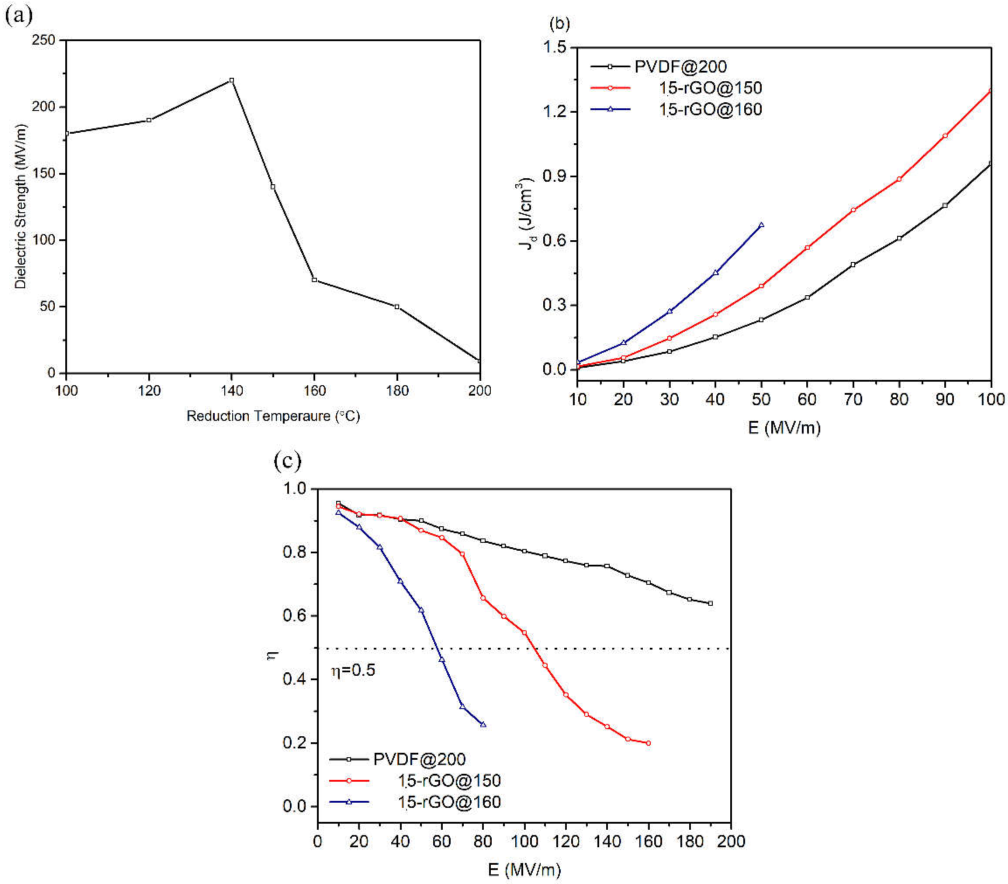

Figure 7.6 Effect of reduction temperature on the (a) dielectric strength, (b) discharging energy density J_d and (c) efficiency η of 0.015-rGO

7.5 Relation Between Dielectric Permittivity and Discharge Energy Density

The above discussion about ε and J_d makes the question about how to design the composite ε particularly important. The challenge to answer this question is to establish a method of using ε to evaluate the discharge energy density J_d of a composite at any charging field.

As discussed, the carrier recombination is charge density limited, which may indicate a direct relation between η and charge displacement D. To demonstrate, we plotted a series of discrete η-D pairs in Figure 7.7, which were measured from a pure PVDF and all nanocomposites involved. We show the η-D relation of all samples can be described by an exponential decay function, which can be constructed as:

$$\eta = \eta_0 \exp\left(-\frac{D}{\alpha}\right) \tag{7.5.1}$$

where $\eta_0 = 1$ is the static energy efficiency and α is a constant. By fitting with only the experimental data of the PVDF, we found α=0.051, and the function is shown as a solid curve in Figure 7.7. As seen, the curve is also in good agreement with experiment data of the nanocomposites, demonstrating the η-D relation is intrinsic to the matrix regardless of the conditions of inclusion particles. Using $D = \varepsilon E$, equation (7.5.1) can be modified to:

$$\eta(\varepsilon, E) = \exp\left(-\frac{\varepsilon E}{0.051}\right) \tag{7.5.2}$$

Equation (7.5.2) establishes the η-ε relation making possible evaluating J_d for PVDF composite at any charging field by calculating the corresponding η by ε. As an example, the insert figure in Figure 7.7 compares the experimental and calculated J_d for 1.5-rGO@150 and 1.5-rGO@160. As seen, the calculated J_d curves fit reasonably well with the experimental data, though an underestimation is observed at stronger charging field. The gap between calculation and experiment can be attributed to the non-linear junction capacitance as well as the instantaneous conformational transition of PVDF polymers.[115] Therefore in practise, we claim equation (7.5.2) is relatively accurate in evaluating J_d for composite capacitors charging at weak field or constructed with a linear matrix. For those charging at strong field or constructed with a non-linear matrix, equation (7.5.2) may only estimate the lower limit of their J_d.

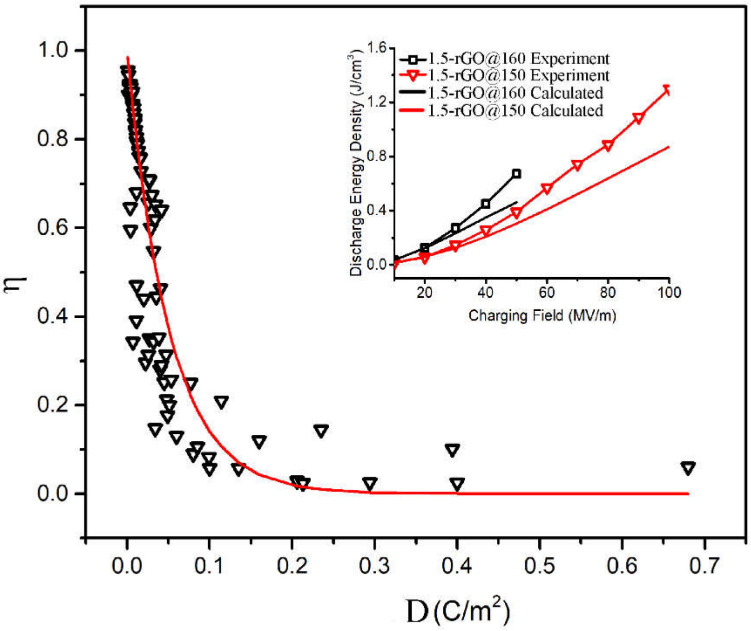

Figure 7.7 Plots of discrete efficiency-charge displacement pairs measured from both pure PVDF and nanocomposite devices with varies reduction temperature and rGO content, the solid curve is the fitting result of the PVDF device, which fits well with the nanocomposites data, insert figure compares the experimental and calculated discharge energy density for two nanocomposite devices.

7.6 Summary

In this chapter, we measured the dielectric behaviour of the rGO/PVDF nanocomposites, the results demonstrate the model in Chapter 6. The findings of this chapter can be listed as the followings:

1. Enhanced dielectric permittivity has been observed in rGO/PVDF nanocomposites. The dielectric permittivity is found to be affected by two factors, the rGO volume fraction and reduction temperature. This demonstrates the contribution of rGO/PVDF heterojunctions.

2. We demonstrate composites with higher dielectric permittivity are more likely to exhibit high loss. The high dielectric permittivity can inevitably cause a weak breakdown strength, and their energy efficiency drops more rapidly upon increasing the charging field strength. This finding implies that tanδ is not a suitable parameter to evaluate the loss of composite capacitors.
3. We demonstrate the charge carrier recombination as the predominant kinetics of leakage in composite capacitors with large dielectric permittivity.
4. We show a strategy to improve the discharge energy density by balancing the dielectric permittivity and dielectric strength of the composites. This done by increasing the series resistance of rGO/PVDF heterojunction via a low temperature reduction regime. A nanocomposite with 1.5 vol.% rGO reduced at 160°C exhibits a discharge energy density of 0.67 J/cm^3 at 50MV/m, which is 3 times higher than that of the pure PVDF.
5. We established an explicit relation between dielectric permittivity and energy efficiency, which can be used to predict the discharge energy density of a composite capacitor.

Chapter 8 β-Phase Formation in the rGO/PVDF Nanocomposites

8.1 Introduction

There are three conformations in PVDF molecule chains resulting at least 4 distinct crystal structures. Among those, β phase is the most desired in smart device applications as it exhibits the strongest dipole moment. One of the dramatic effect of inclusion addition is to induce β phase nucleation in PVDF polymer. This makes the PVDF composite ferroelectric and applicable to smart devices. This chapter is an investigation of the β phase formation in rGO/PVDF nanocomposites. The purpose of this chapter is to reveal the characteristics of β phase crystal in the rGO/PVDF nanocomposites to show their applicational potential in smart devices.

To do this, this chapter is structured as follows. First, we will study the molecular conformation in rGO/PVDF nanocomposites using the attenuated total reflection infrared (ATR-IR) technique. Both effects of reduction temperature and rGO content are investigated. Then, we report a detailed investigation of the crystal structure by the X-ray diffraction (XRD) technique. The morphology and local piezoelectric response of the nanocomposites will be measured by the Atomic-/Piezo-force microscopy (AFM/PFM). These results are discussed and a mechanism for β phase formation is proposed with consideration of the contribution of the rGO/PVDF interface.

8.2 Molecular Conformation in the rGO/PVDF Nanocomposites

In this section, we report the use of infrared (IR) absorption spectra to investigate the molecular conformation in the rGO/PVDF nanocomposites. rGO/PVDF nanocomposites with rGO content between 1.0 vol.% to 2.5 vol.% and reduced at 100°C to 200°C for 1h were prepared and tested. An FT-IR spectroscopy (Tensor II, Buker Cooperation, Germany) with a single reflection ATR accessory (MIricale, Piketech, USA) was used, details can be found in Chapter 5.

Figure 8.1 shows the ATR-IR spectra for the rGO/PVDF nanocomposites and pure PVDF, all of which were annealed at 200°C for 1h. For the pure PVDF polymer, sharp peaks at 614 cm^{-1}, 760 cm^{-1}, and 976 cm^{-1} was observed, which can be associated to the non-polar TGT$\bar{G}$ molecular conformation.[116] Meanwhile, the much stronger peak at 1271 cm^{-1} compared to 840 cm^{-1} and the absence of peaks at 813 cm^{-1}, 1234 cm^{-1}, and 1275 cm^{-1} indicated that the α phase is predominant in the pure PVDF.[29,32,117] This can be attributed to the thermal stability of α phase that resulting in a preferred nucleation. While for the nanocomposites, the newly emerged peaks as well as intensity changes were observed in the IR spectra, which can be associated to the formation of TTTT conformations. To start, the 614 cm^{-1}, 764 cm^{-1}, and 976 cm^{-1} bands can still be observed, which indicates the existence of TGT$\bar{G}$ chains in the nanocomposites. Meanwhile, an increased relative intensity of the 840 cm^{-1} band over the 1271 cm^{-1} band was observed, which can be associated with the formation of long term (T>3) trans sequence and could be recognized as the characteristic of β phase. In addition, two shoulders peaks were observed at 813 cm^{-1} and 1230 cm^{-1}, which could either be attributed to the existence of γ phase with shorter trans (T<3) sequence.[23] Because the absorption bands of γ phase exhibits as shoulder peaks with weak intensity, we therefore treat the shorter trans sequence as the defect in TTTT chains. According to the IR spectra, we claim the addition of rGO can induce the transition of TTTT PVDF chains that constructs the β phase.

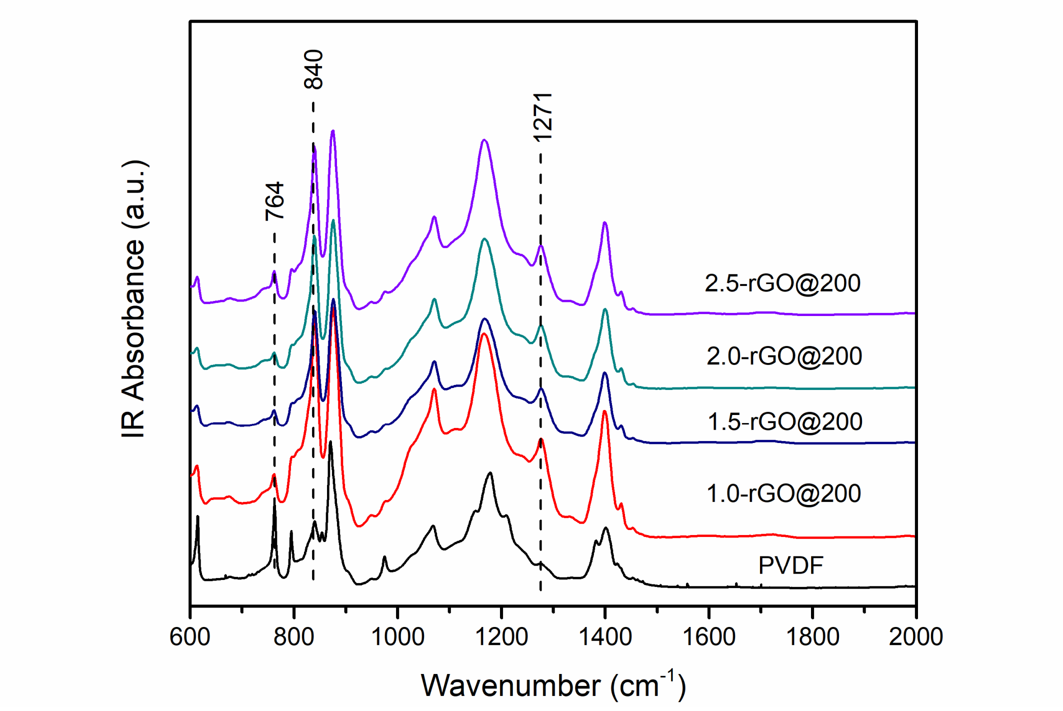

Figure 8.1 ATR-IR spectra of pure PVDF and rGO/PVDF nanocomposites

The relationship between the formation of β phase and the annealing temperature T_r is shown in Figure 8.2 The results indicate that while pure PVDF and the nanocomposites show analogous phase content when annealed at low temperatures, variations can be observed at annealing temperatures of 200°C. Figure 8.1 (a) shows the ATR-IR spectra for pure PVDF polymer annealed at 100°C, 150°C, 170°C and 200°C for 1h. For pure PVDF annealed at 100°C (PVDF@100), the relative high intensity of 840 cm^{-1} can be attributed to the existence of all-trans conformations of polar phase, and the relatively higher intensity of 1230 cm^{-1} over that of 1271 cm^{-1} indicates that short sequence

(TTTG) is dominant in the polar molecule chains.[29,118,119] Besides, the weak intensity of the 614 cm^{-1} with the disappearance of the 760 cm^{-1} and the 976 cm^{-1} bands indicates a minor amount of non-polar trans-gauche chains.[25] Hence, the PVDF@100 is predominantly a β/γ phase mixture. The formation of polar molecule chains in the low temperature annealed samples can be attributed to the chemical interaction between PVDF chains and either polar molecules of the DMF solvent or functional groups of GO.[77,120] At current stage, it is difficult to identify which effect is dominant. For PVDF@150, the absorption intensity of all bands increases compared with PVDF@100, indicating an increased crystallinity with further evaporation of the residue solvents. However, no new band emerges, and the crystal structure is identical to that of the PVDF@100. With further increasing the temperature to 200°C, a significant increase in the relative intensity of the 614 cm^{-1} band can be observed, followed by decreased all trans peaks at 840 cm^{-1}, 1230 cm^{-1} and 1271 cm^{-1}, indicating the formation of non-polar α phase.[25] For the nanocomposites 0.025-rGO@100 and 0.025-rGO@150, the ATR-IR spectra show no difference with that of PVDF@100 and PVDF@150, as shown in Figure 8.2(b). However, variations can be observed between PVDF@200 and 0.025-rGO@200, where the decreased intensity of 1230 cm^{-1} is simultaneously associated by the growing 840 cm^{-1} and 1271 cm^{-1} bands. This means, apart from transferring to non-polar α phase, the γ phase is transferred to β phase.[36,119]

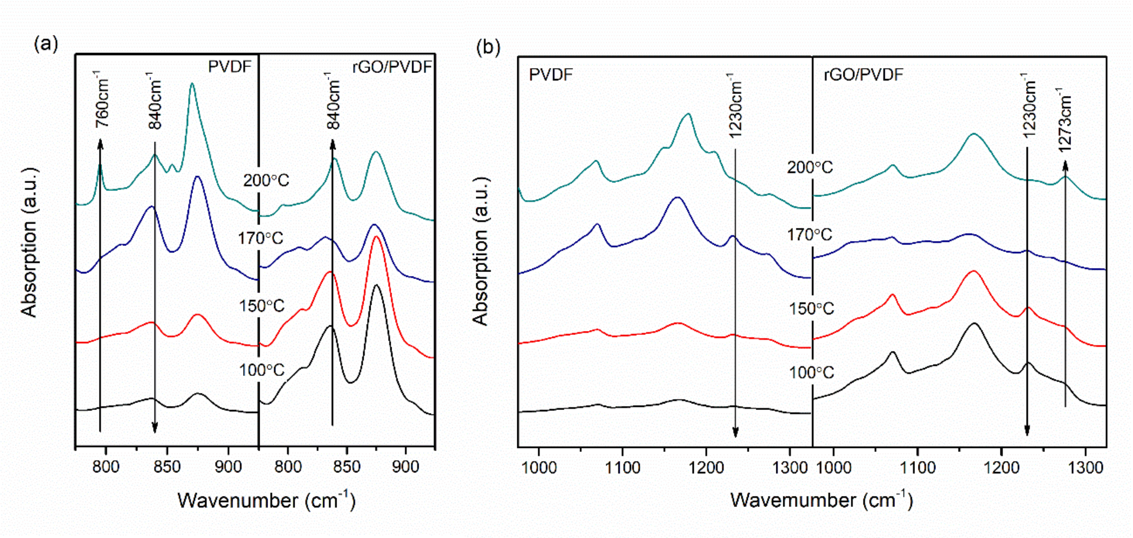

Figure 8.2 ATR-IR spectra comparing pure PVDF and rGO/PVDF nanocomposites at annealing temperatures ranging from 100°C to 200°C, with IR wavenumber between (a) 775cm^{-1} to 950cm^{-1}, and (b) 975cm^{-1} to 1350cm^{-1}

The melting temperature T_m of the pure PVDF is stated to be about 155°C~160°C in the manufacture data sheets, and 160°C~180°C in the literatures depending on the crystalline forms as well as processing method.[121-125] To ascertain the melting point range of the PVDF polymer prepared in this research, we measured the dielectric permittivity vs. temperature plots of both an as-casted 1.5-rGO and an as-casted pure PVDF, which is plotted in Figure 8.3. Generally, the α-PVDF does not have a Curie point, the temperature for the ferroelectric to paraelectric transition, and the β- and γ-PVDF possess a curie temperature range overlapping with that of the melting temperature.[126] This means the temperature where dielectric permittivity peaks can be regarded as the melting point. As seen, the as-casted PVDF exhibits a peak dielectric permittivity at about 156 °C~161 °C, which is in good agreement with that stated in the manufacture data sheet. As for the as-casted 1.5-rGO, the dielectric permittivity ceased to grow above ~ 122 °C, and a sharp decrease in dielectric permittivity was observed at ~169 °C. The wide temperature range for as-casted 1.5-rGO may not be solely assigned to its melting behaviour but may also corelated to the reduction of GO. Still, it is reasonable to claim a melting point lower than 169 °C due to the sharp decrease in dielectric permittivity. Concerning the change in IR absorption with respect to temperature, we therefore suggest that the molecular conformational transition occurs in the melt-PVDF, and the TTTT molecular chains will pack to form the β phase on cooling the melt. As it is quite natural that pure PVDF will recrystalize in the more thermal-dynamically stable α phase, the contrasting results observed in the nanocomposites highlights the effect of rGO in the formation TTTT molecular chains and accordingly the β phase.

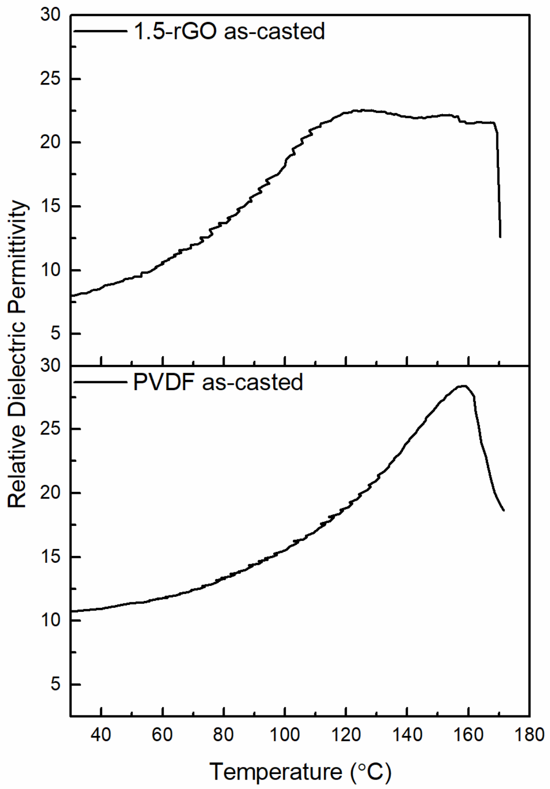

Figure 8.3 Dielectric permittivity vs. temperature plots for an as-casted 1.5-rGO and an as-casted pure PVDF

One limitation of the IR spectra is that it only shows the information of a single point on the sample surface. The effective depth of penetration d_e of the IR beam for parallel and perpendicular polarization can be calculated, respectively, as:[36,119]

$$d_{parr} = \frac{n_1^2 n_2 \cos\theta}{(n_1^2 - n_2^2)} \cdot \frac{2n_1^2 \sin^2\theta - n_2^2}{(n_1^2 - n_2^2)\sin^2\theta - n_2^2} \cdot \frac{\lambda}{\pi\sqrt{n_1^2 \sin^2\theta - n_2^2}} \tag{8.2.1}$$

$$d_{perp} = \frac{n_1^2 n_2 \cos\theta}{(n_1^2 - n_2^2)} \cdot \frac{\lambda}{\pi\sqrt{n_1^2 \sin^2\theta - n_2^2}} \tag{8.2.2}$$

where n_1, n_2 is the reflective index of the ZnSe crystal and PVDF, θ is the incident angle of the IR beam, and λ is the wavelength. The d_e is a mean value between d_{parr} and d_{perp}. Therefore by taking n_1=2.4 and n_2=1.4 [127], the d_e associating to the IR beams absorbed by 760 cm^{-1} and 840 cm^{-1} can be calculated as 5.74 μm and 5.06 μm. This small incident area means the IR spectra may only represent the surface condition of the sample films. Hence, addition information is still needed to study the microstructure of the nanocomposites.

8.3 Crystalline Structure of the rGO/PVDF Nanocomposites

In this section, we will use the X-ray diffraction (XRD) to study the crystalline structure of the rGO/PVDF nanocomposites. The XRD spectra of testing samples were measured by an X-ray diffractor (Bruker D8 Advanced, Bruker, USA) with CuKα radiation (1.5405 Å), with 2θ ranging from 10° to 140°.

Figure 8.4 shows the X-ray diffraction patterns for pure PVDF and the nanocomposites reduced at 200°C for 1h. As seen, the X-ray radiation has a penetration higher than the thickness of both PVDF and the nanocomposite films, as the sharp peak marked by the

* mark can be associated to the major diffractions of the Blu-Tack paste (Bostik, USA) used to glue the samples on the testing stage. This means XRD spectra can provide a complementary microstructure information for the nanocomposites.

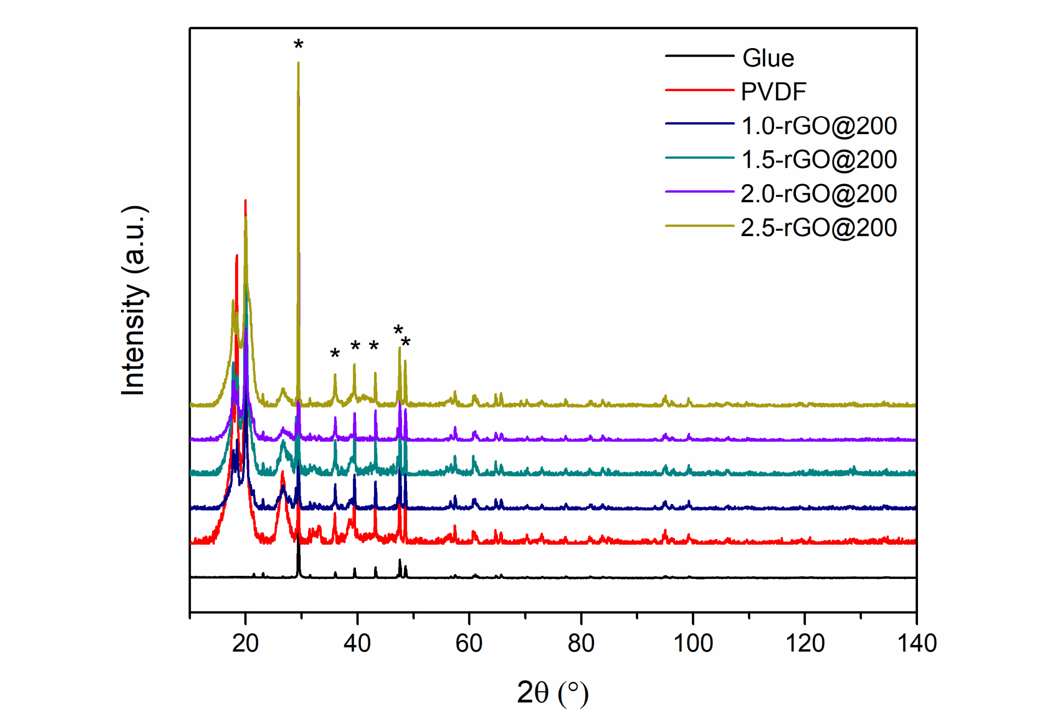

Figure 8.4 XRD spectra for PVDF and nanocomposites annealed at 200°C, the peaks marked by * is assigned to the substrate

To show details of the crystalline structure, we have studied the XRD pattern in the range between 2θ values of 14° to 25°, which are fitted with Lorenz function and shown in Figure 8.5(a) to (e). The peaks at 17.7°, 18.4°, 19.6° in the pure PVDF pattern can be assigned to (100), (020), and (110) planes, respectively, of the α phase while the formation of a shoulder peak at 2θ=20.6°C in the nanocomposite pattern can be assigned to either the (200) or the (110) planes of the β phase.[34,128] It can be observed that a very broad peak exists at around 2θ = 19°, which can be associated to the amorphous phase. We observed a growing intensity of β(200)/(110) as well as α(100) diffractions with increasing rGO volume fraction, which indicate a direct relation between rGO addition and β-PVDF transition.

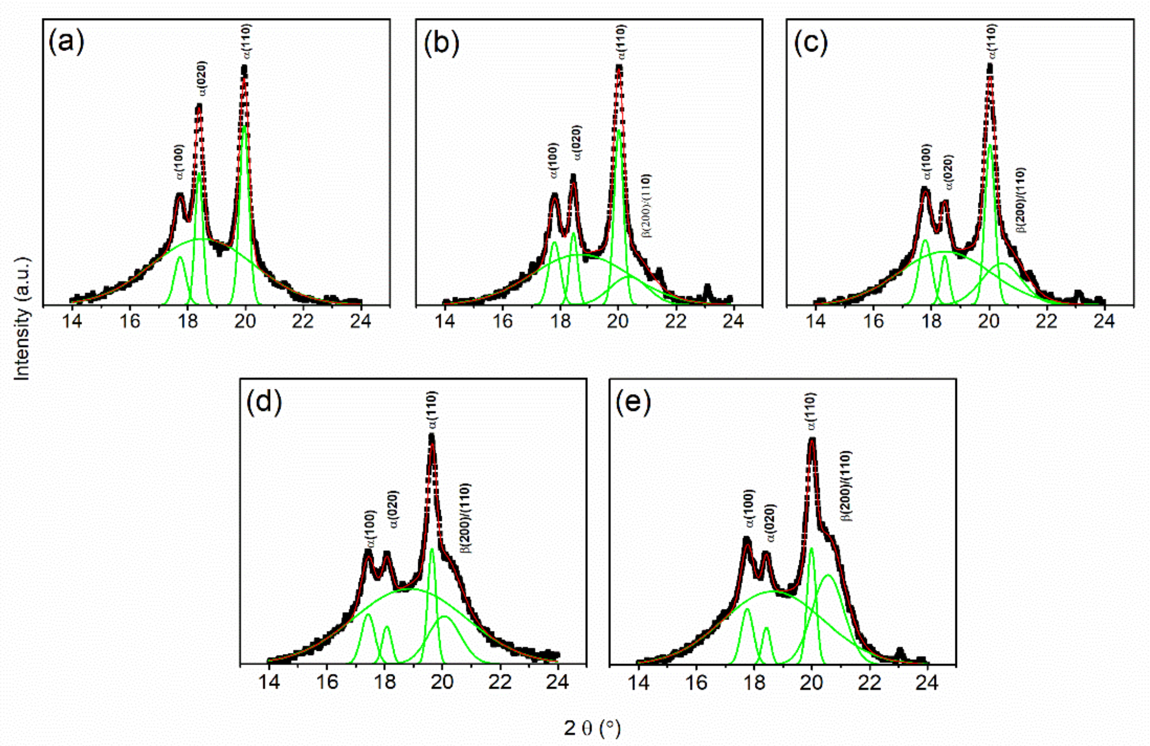

Figure 8.5 Fitting curves with Lorenz peak function for (a) pure PVDF and (b) to (e) the nanocomposites reduced at 200°C

The major challenge in quantitatively analyse the XRD pattern for the PVDF and the related composites is the overlapping of β(200) and β(110) diffractions due to the analogous lattice spacing. In this research, we suggest the shoulder peak at around 2θ=20.6° may be assigned to β(110) diffraction. To start, we calculated the β phase content X(β), which is plotted in Figure 8.3.3(a). Each point is an average of three samples. The X(β) is defined as:

$$X(\beta)=\frac{I_{\beta(200)/(110)}}{I_{\beta(200)/(110)}+I_{\alpha(100)}+I_{\alpha(020)}+I_{\alpha(110)}} \tag{8.3.1}$$

where I is the intensity of X-ray diffractions. As seen, the increase in rGO content give rise to a higher X(β), as the X(β) for 1.0-rGO@200 is merely 0.08, which was increased to 0.32 for 2.5-rGO@200. This establishes a direct relation between rGO addition and nucleation of the β-PVDF. As indicated in Figure 8.6, the addition of rGO also induced a change in the intensity of the α(100) diffraction. However, the X(α(100)) does not always increase with increasing rGO volume fraction, which is also indicated in Figure 8.6(a). This means the rGO may not have a direct impact on the nucleation of α-PVDF with (100) orientation. By regarding the change in intensity of the α(100) diffraction as a texture growth in α-PVDF, its texture quality F(α(100)), defined as:

$$F\left(\alpha(100)\right)=\frac{I\left(\alpha\left(100\right)\right)}{I\left(\alpha\left(100\right)+\alpha\left(020\right)+\alpha\left(110\right)\right)} \tag{8.3.2}$$

is calculated and plotted in Figure 8.6(b). As seen, F(α(100)) increases with increasing rGO volume fraction, indicating the addition of rGO can induce a preferred (100) orientation in α-PVDF. One possible explanation of the rGO induced crystal structure change in PVDF polymer is sketched in Figure 8.6(c). As X(β) is directly related to the rGO content, it is reasonable to assume a layer of β-PVDF on the rGO surface. This assumption is in accordance with the experimental and calculated results reported in the literatures.[67,68,77,129] Comparing the result of X(β) and X(α(100)), it is claimed that β phase possess the priority to form on the rGO surface and the α(100) may grow epitaxially with β phase as substrates. This is supported in Figure 8.6(b) by the increased FWHM of α(100) diffraction indicating increased density of defects due to disordering at the α/β phase boundary. The parameter of α(100) lattice is 9.64Å*4.96Å while that for the β(200) lattice is 4.91Å*2.56Å and for β(110) is 9.87Å*2.56Å. Compared to the β(200), the β(110) lattice possesses a smaller lattice mismatching hence is more likely to induce the epitaxial growth of the α crystals with (100) orientation. Hence, we claim that the shoulder peak at 20.6° could mainly be assigned to the β(110) diffraction, and the local structure on the rGO surface may be a layer of β phase grafted with the α phase shell.

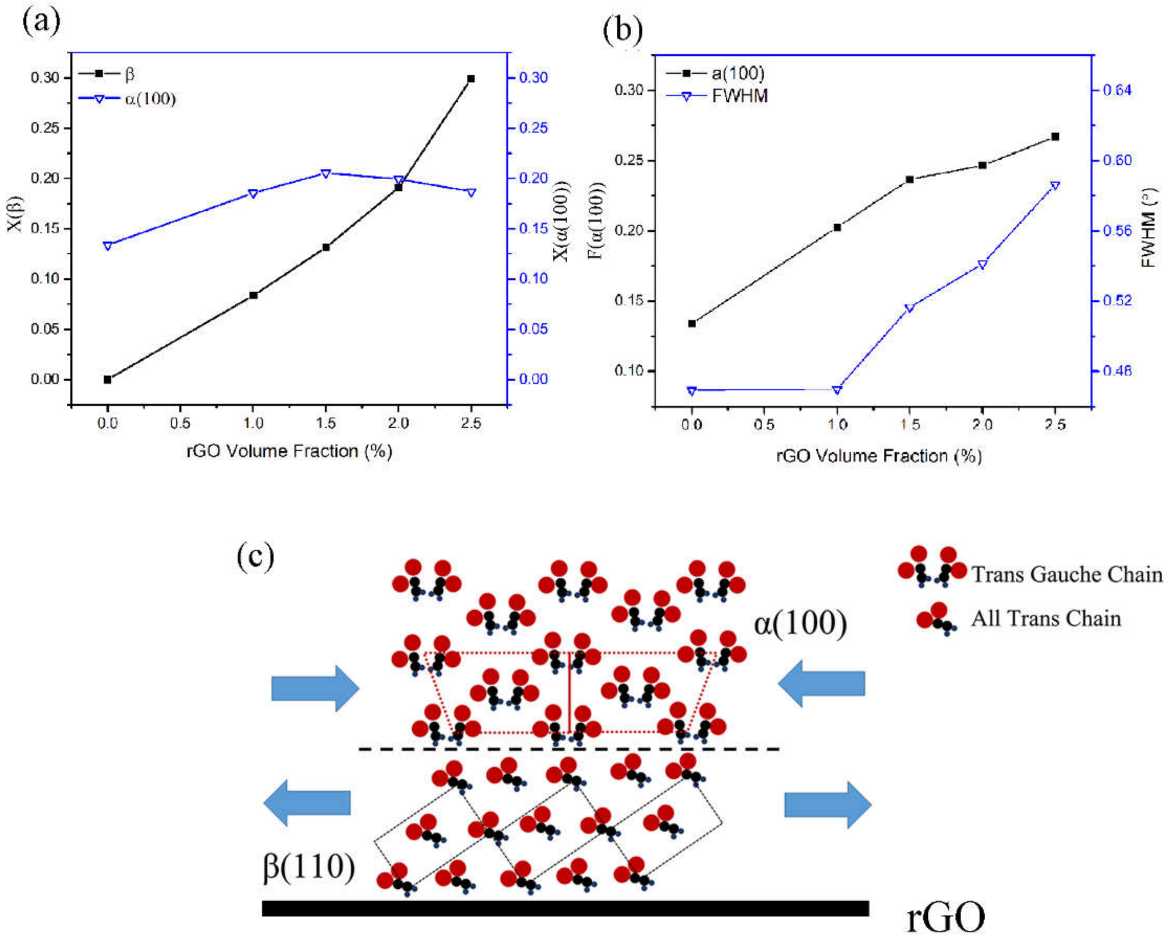

Figure 8.6 (a) content of β(110)/(200) and α(100) in the crystalline forms, (b) content of α(100) in the α phase and its FWHM changes with respect to the rGO volume fraction, and (c) illustration of the β(110)/α(100) stack structure in the nanocomposite sample.

8.4 Morphology and Local Piezoelectric Response of the rGO/PVDF Nanocomposites

In this section, we will study the morphology and local piezoelectric response of the rGO/PVDF nanocomposites. An atomic force microscopy (AFM) (NTEGRA Prima, NT-MDT Spectrum Instruments, Russia) with piezo-force microscopy (PFM) module was used for the measurements. Details can be found in Chapter 5. The AC voltage applied to the tip is 5V at 100Hz. The butterfly loops were measured by applied a -30V to 30V DC voltage sweep to the samples.

Figure 8.7(a) and (b) show the morphology of a pure PVDF and a 1.0-rGO@200. As seen, the nanocomposite exhibits a rougher surface compared to pure PVDF indicating an agglomerated nucleation of PVDF polymer at the existence of rGO. We show each agglomerate is packaged by α phase as evidenced by the covering spherulites composed of folded TGT$\bar{G}$ chains.[130] Meanwhile, we used piezo-force microscope (PFM) to probe the electromechanical response for both samples. We applied a sweep voltage of -30V to 30V onto selected points and captured the displacement loop, the results are plotted in Figure 8.7(e), (f), and (g). As for nanocomposite, we found the electromechanical response to be capacitive on top of the spherulites shell while ferroelectric at the valley between individual agglomerates. This can be supported by the hysteresis characteristics on the nanocomposite amplitude-voltage loop due to saturation of the molecular dipole. As for the pure PVDF, its amplitude-voltage loop is also linear, which is analogous to the spherulites shell of the nanocomposites. The PFM results demonstrate that the β phase is locally heterogeneous in the nanocomposite. This result supports the microstructure model in Figure 8.7(c). On top of the spherulites, a thick α phase shell may predominantly contribute a capacitive response, while this shell is thinned at the valley exposing more β phase to contribute a ferroelectric response.

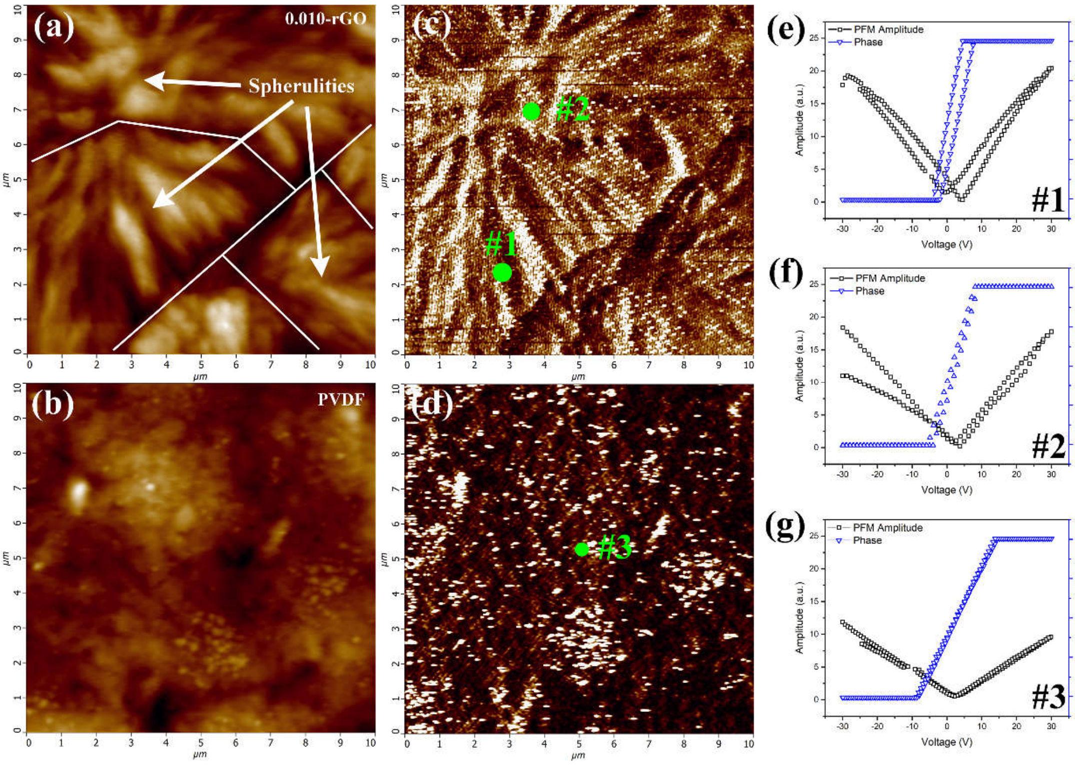

Figure 8.7 AFM images for (a) 1.0-rGO@200 and (b) pure PVDF indicate the nanocomposite possess rougher surface of agglomerated spherulites, PFM images for (c) 1.0-rGO@200 and (d) pure PVDF show cross-talk signal from morphology fluctuation, therefore we applied a -30V to 30V DC sweep to individual points to test the local electromechanical response, which are plotted in (e) to (g)

8.5 Formation Mechanism of β Phase in the rGO/PVDF Nanocomposites

In this section, we will discuss the formation mechanism of β phase in the rGO/PVDF nanocomposites. Our experimental data in the above sections can establish a direct relation between β phase formation and rGO content, which suggests a priory nucleation of β phase in the nanocomposites. Besides, the β phase was only observed in the nanocomposites reduced above the melting point, suggesting a melting-recrystallization manner of the β phase formation mechanism. Concerning the removal of hydrophilic groups in rGO upon heating the nanocomposites, it is unlikely to attribute the β phase formation to the hydrogen bonds between rGO hydrophilic groups and TTTT chains.

One way to assess the formation mechanism of β phase formation from melt is from the perspective of the system Gibbs free energy change. For a homogeneous nucleation, the change of system Gibbs free energy ΔG is:

$$\Delta G = \Delta G_U U + \Delta E_S \tag{8.5.1}$$

where ΔG_U is the difference of Gibbs free energy per volume U between the solid and melt, and ΔE_S is the different of surface energy between the solid and melt.[131,132] Equation (8.5.1) well describes the nucleation of α phase in the pure PVDF. With the addition of an extrinsic inclusion, the nucleation becomes heterogeneous due to the catalyse effect of inclusion surface. The free Gibbs energy change for heterogenous nucleation ΔG(θ) can be described as:

$$\Delta G(\theta) = \Delta G f(\theta) \tag{8.5.2}$$

where $0 \le \theta \le \pi$ is the wetting angle.[133] When $\theta = \pi$, equation (8.5.2) becomes equation (8.5.1) and the nucleation is homogeneous. Comparing equation (8.5.1) and (8.5.2), it can be indicated that the inclusions, such as rGO in this case, can accelerate the nucleation. This, however, does not necessarily result in the nucleation of the thermodynamically instable β phase. Modification of equation (8.5.2) concerning the equalization between inclusion Fermi level and melt electrochemical potential has been reported in many literatures, which added an energy saving ψ to volume free energy change as:[134-136]

$$\Delta G(\theta) = ((\Delta G_U U - \psi) + \Delta E_S) f(\theta) \tag{8.5.3}$$

Herein, we claim this equalization should exist in the contact of rGO and melt-PVDF due to their differences in compositions. The Fermi level-electrochemical potential equalization can result in rGO surface to be charged, either positively or negatively depending on the relative position of its Fermi level, which will induce a screening phenomenon in the melt-PVDF. According to this, there are good reasons to assume an electrical double layer (EDL) structure in the melt-PVDF composed to screen the rGO surface charge. This is illustrated in detail in Figure 8.5.1 (b). As illustrated, the Helmholtz layer is constructed by a layer of tightly bonded TTTT molecules with its built-in field counter-balances the electrostatic field of the rGO surface charge. After the Helmholtz layer is the diffusion layer constructed by loosely absorbed TTTT molecules, the rGO-PVDF interaction in this area is weaker than that in the Helmholtz layer as the Stern potential is far smaller than the surface potential. The melt-PVDF in the EDL can nucleate to the β phase on cooling the melt, which could be an explanation of the growth of β phase on the rGO surface from the PVDF melt. According to the discussion in Chapter 6, the rGO surface charge σ due to Fermi level equalization can be defined as:

$$\sigma = \sigma_0 (\exp(\frac{\psi}{kT}) - 1) \tag{8.5.4}$$

where σ_0 is the electron density of rGO. Regarding a fully flexible chain in the melt and the polarization density p as the effective charge density of a TTTT chain, we can give the criterion for TTTT chain absorption on the rGO surface as:

$$\sigma \geq p \tag{8.5.5}$$

This means the energy saving due to Fermi level equalization should be sufficiently large to induce the TTTT transition, otherwise the PVDF will remain TGT $\bar{G}$ conformation and nucleate to α phase. The β phase formation mechanism also indicate a unique molecular dipole configuration on the rGO surface. As rGO is a planar particle and is uniformly charged, the molecular dipole perpendicular to the rGO surface should exhibit a dipole orientation mirrored by the rGO plane. This means the one rGO particle with its nearby polar PVDF chains can construct a micron bimorph device, making the nanocomposite self-polarized. This finding indicates the potential of using self-polarized rGO/PVDF nanocomposites with symmetrical dipole configuration as an actuator or sensor device. The direct piezoelectric response of the rGO/PVDF nanocomposite is illustrated in detail in Figure 8.8 (c). When the nanocomposite undergoes an upward/downward bending moment M, the PVDF dipoles on the top/bottom of the rGO sheet will be stretched while those on the bottom/top will be compressed. This dipole polarization/depolarization process will induce a potential difference between the top and bottom surfaces of the rGO sheet, which is the mechanism of piezoelectricity for the rGO/PVDF nanocomposite.

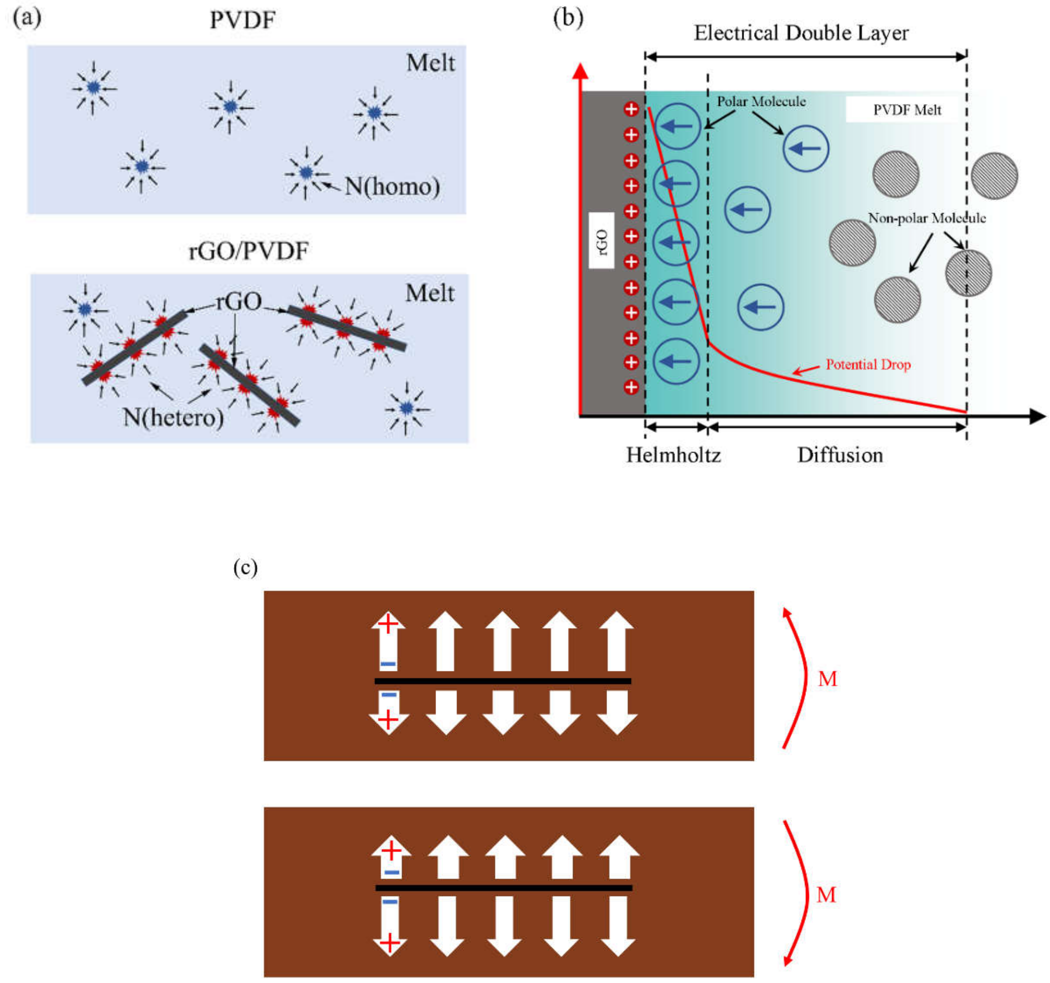
(a)
PVDF
Melt
N(homo)
rGO/PVDF
Melt
rGO
N(hetero)
(b)
Electrical Double Layer
Polar Molecule
PVDF Melt
Non-polar Molecule
rGO
Potential Drop
Helmholtz
Diffusion
(c)
M
M

Figure 8.8 (a) Comparison of the homogeneous nucleation (N(homo)) in pure PVDF and heterogeneous nucleation (N(hetero)) in the nanocomposite, (b) β phase formation due to TTTT molecule absorption and packaging at the rGO surface forming electrical double layer structure in the PVDF melt, assuming rGO is positively charged, the built-in field of the PVDF dipole (indicated as an arrow) will counter-balance the static field of the rGO surface charge and (c) illustration of symmetrical PVDF dipole (white arrow) on the rGO surface (black line) surface forming a self-bimorph in the nanocomposite

8.6 Summary

In this chapter, we studied the molecular and crystal structure of the rGO/PVDF nanocomposites. The findings of this chapter can be listed as the followings:

(1) The ATR-IR spectra indicate the existence of TTTT PVDF chains confirm the formation of β phase in the rGO/PVDF nanocomposites in the melting-recrystallization procedure.

(2) X-ray diffraction shows a direct relation between β phase content and rGO volume fraction. The volume fraction of up to 0.30 for β phase is obtained in 2.5-rGO@200. The formation of β phase also induces a(100)-orientation. This is explained by an α/β stack model suggesting the β phase is packaged by an α crystal shell.

(3) The AFM image clearly shows the spherulites structure dominate the nanocomposite surface morphology, demonstrating the α phase shell. The PFM image shows an inhomogeneous distribution of β phase at the valley of spherulites for the nanocomposite sample. This inhomogeneity is explained as a thinner α shell at the valley causes an exposure of the underneath β phase.

(4) A β phase formation mechanism is proposed based on the experimental data. We suggest the equalization of rGO Fermi level and melt-PVDF electrochemical potential charges the rGO surface constructing an electrical double layer (EDL) in the melt. A tightly bonded layer of TTTT chains can therefore compose the Helmholtz layer in the EDL forms the β phase on cooling the nanocomposites. Besides, we also suggest the electrical dipole of the β phase exhibit a mirrored orientation with respect to the rGO plane, this would result in a self-polarized bimorph behaviour.

Chapter 9 rGO/PVDF Nanocomposite Related Devices

9.1 Introduction

In the last chapter, we showed the formation and self-alignment of the β phase in rGO/PVDF nanocomposites, which made them piezoelectric without additional treatment. Therefore, it will be interesting to know how these nanocomposites will perform in smart devices. In this chapter, we report the fabrication and characterisation of two prototype devices, an actuator and a flexible energy harvester, to study the piezoelectric properties of the nanocomposites. This chapter is structured in the following way.

The first part of this chapter is focused on the piezoelectric responses of the actuators. We start from the device design and assembly procedure, followed by introducing the set-up of the measuring system. The piezoelectric properties of the as-assembled device were measured and compared with a commercial PVDF membrane. The unique self-bimorph characteristics of the nanocomposites are discussed. The other part of this chapter is about a flexible energy harvester, which is also assembled with the nanocomposites. The configuration of the measurement as well as the device fabrication is reported. The energy output characteristics was measured and discussed.

9.2 Actuator Assembly and Measurement Configuration

Piezoelectric materials can generate a strain response to an applied electric field, hence can be assembled in an actuator for bending or vibration control applications. In this section, the advantages and drawbacks of using rGO/PVDF nanocomposites in actuator applications are evaluated.

Figure 9.1(a) shows the structure and mechanism of a bi-clamped actuator (BCA) device with a polarized piezoelectric component. The ferroelectric domain is defined as pointing downwards. The vibration of this BCA with an applied electric field E can be attributed to the transverse piezoelectric effect defined as:

$$S_{31} = -d_{31}E \tag{9.2.1}$$

where S_{31} is the transverse strain and d_{31} is the transverse piezoelectric constant.[8,137] If a positive electric field, defined as that in the same direction as the polarization, is applied to the BCA, the device should generate a negative S_{31} to compensate for the increase in S_{33}. In the bi-clamped condition as shown in the figure, the S_{31} of the upper surface is higher than that of the lower. This causes a negative curvature to the beam due to surface tension. In terms of the device, a downward bending should be expected and vice versa under a negative electric field. In this research, two BCAs were fabricated, one with a commercial polarized PVDF film (Pizotech Arkema, France) with thickness of 114 μm, and the other with a 1.5-rGO@200 nanocomposite with thickness of 80μm. While the commercial PVDF film possess an Au electrode, the 1.5-rGO@200 was sputtered with Cr/Au electrode. Both samples were cut with a sharp knife to a 1 cm × 0.5 cm rectangular tape. The BCA device is fabricated by gluing each end (~0.2 cm) of the tapes on a glass substrate by a super glue (406, Loctite, France) and wiring the front and back electrodes. The BCA device was then fixed on the testing stage. The sputtering method was stated in detail in chapter 5. To measure this strain response of a BCA device, we designed the testing method as shown in Figure 9.1(b). The measurement equipments contain an oscilloscope (Picoscope 3206, Pico Technologies, UK), a function generator (RS component, UK), a voltage amplifier (OEM MODEL

PA05039, Agilent Technologies, USA), a modular laser vibrometer (OFV2570, Polytec, Germany), a positioning system consisting of two motorized translation stages for the x and y axes (models 8TM173-20-50, 8TM173-20, STANDA, Italy). Briefly, the function generator was connected to the voltage amplifier to deliver a parodic voltage signal to the BCA. The monitor head of the laser vibrometer was hanged above the BCA and the laser beam was focused on the centre of the BCA. The monitor head was connected to its controller, and the collected displacement signal is delivered from the controller to the oscilloscope. Both the applied voltage and displacement signals were monitored by the Picoscope monitoring software program (Pico Technologies, UK).

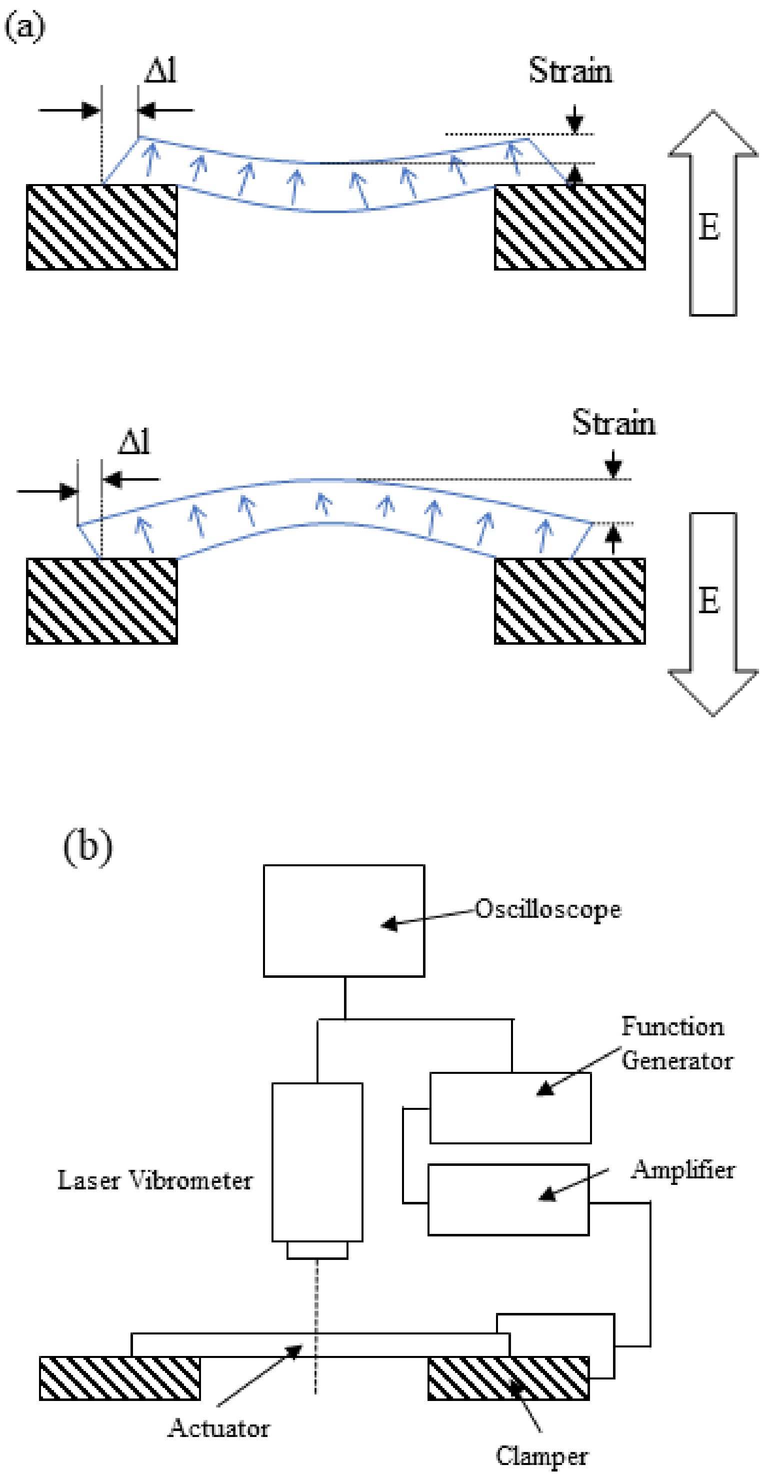
(a)
Δl
Strain
E
Δl
Strain
E
(b)
Oscilloscope
Function Generator
Amplifier
Laser Vibrometer
Actuator
Clamper

Figure 9.1 (a) Vibration regime of a bi-clamped actuator device with respect to the electric field and (b) the vibration measurement configuration

9.3 Vibrational Characteristics of the Nanocomposite

Figure 9.2(a) and (b) compares the vibrational characteristics of BCAs fabricated with the nanocomposites and a commercial polarized PVDF film. As seen, the PVDF-BCA behaves as a single morph as illustrated in Figure 9.2(a), with a downward bending with forward electric field and vice versa. The maximum centre displacement of the PVDF-BCA measured at 100V/mm 20kHz was measured to be 3nm. While for the 1.5-rGO@200-BCA, the centre displacements were found to be in-phase under forward and reverse electric field. This is a bimorph behaviour demonstrating the intrinsic symmetrical domain configuration at the rGO surface as discussed in Chapter 8. The maximum centre displacement of the 1.5-rGO@200-BCA was measured to be 0.6 nm, corresponding to 20% that of the commercial PVDF. Thus, we have demonstrated the concept of a self-bimorph actuator utilizing the symmetrical dipole orientation on the rGO surface. By testing the prototype devices, we have shown it is possible to use the self-polarized piezoelectric composite as an alternative to the bulk counterparts where electrical polarization may be difficult.

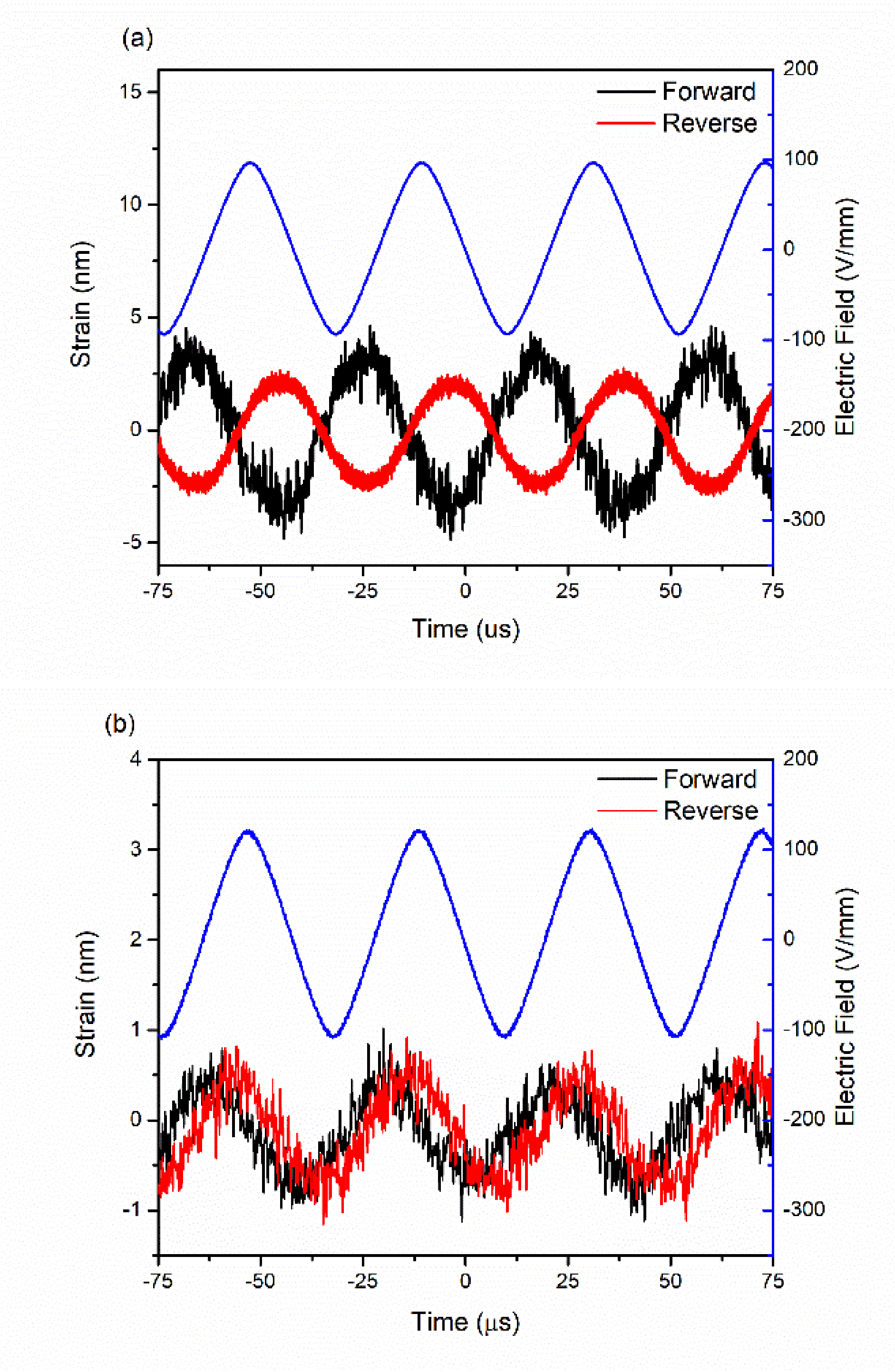

Figure 9.2 Strain responses of BCAs assembled with (a) commercial PVDF film and (b) 0.015-rGO@200 nanocomposite operating at 100V/mm 20kHz

It can be indicated from the strain response that the performance of 1.5-rGO@200-BCA is inferior to that of the commercial PVDF-BCA in terms of the maximum device displacement. This can be attributed to the limitations of the rGO/PVDF composites in actuating applications. To begin with, the β phase content of 0.015-rGO@200 was found to be only 0.12 and is embedded in the non-active α phase. The α phase shell induces a substrate effect causing damping to the β phase vibration. The effort of increasing β content was also found to be inefficient as an increase in the rGO volume fraction introduces higher leakage to the nanocomposites and the device is very vulnerable to the electric field. It was also found that device fabrication was only successful for nanocomposites with 1.0 vol.% and 1.5 vol.% rGO, and only that with 1.5 vol.% could generate a measurable strain. Another drawback is the randomness in rGO orientation. As the bending of the nanocomposite actuator device is amplified by those of individual internal PVDF/rGO/PVDF bimorphs, the random rGO orientation may reduce the effective strain in preferred directions. In addition, the XRD results presented in Chapter 8 indicate a high content of amorphous phase in the nanocomposites. The amorphous phase forms a soft polymer environment which not only absorbs the vibration but also may introduce higher leakage to the nanocomposites. Therefore, we suggest that significant optimisation of the rGO/PVDF nanocomposites could be carried out resulting in high crystallinity and well-oriented rGO particles that may generate an improved strain response in actuator applications.

9.4 Energy Harvester Assembly and Measurement Configuration

It is always demanding to scavenge energy from the environment to fight against the energy crisis. This relies on the energy transfer from one form to another and storage afterwards, which is possible by utilizing the unique nature of functional materials. Piezoelectric material is one kind of these functional materials that could transfer the vibrational energy into electrical energy, which can be used as a "battery-less" solution for self-powered sensor networks.[138-141] In this section, we report the fabrication and characterization of vibrational energy harvesters utilizing the piezoelectric response. Figure 9.3(a) shows the structure of the energy harvester, which is composed of a nanocomposite, wires, and insulating package. The nanocomposites with a thickness of 80μm were cut into a 1 cm × 1 cm square and were sputtered with Cr/Au electrode on both surfaces. To wire the nanocomposites, two sections of cupper tape were cut and connected on the nanocomposite by silver paste. The wires were then soldered to the cupper tapes. After that, all elements were plastic-packaged to a device. Figure 9.3(b) shows the graph of the vibration measurement configuration. One end of the energy harvester was mechanically clamped by a metal cap that fixed on an electromagnetic shaker (Gearing & Watson Electronics, UK) head and the other end is free to vibrate with respect to the shaker vibration due to resonance. This will induce a bending stress to the nanocomposites, which was monitored by a laser vibrometer (M5L/2, MEL, Germany) and an accelerometer (4370, Brüel & Kjær, Denmark). Simultaneously, the nanocomposite can react to the bending stress and generate a voltage difference between electrodes. Both the bending signal and electrode signal was collected by an oscilloscope (Pico 3206, Pico Technologies, UK) and monitored by the Picoscope software on the computer. The input impedance of the oscilloscope is 1MΩ and the maximum sampling rate of 1MS/s.

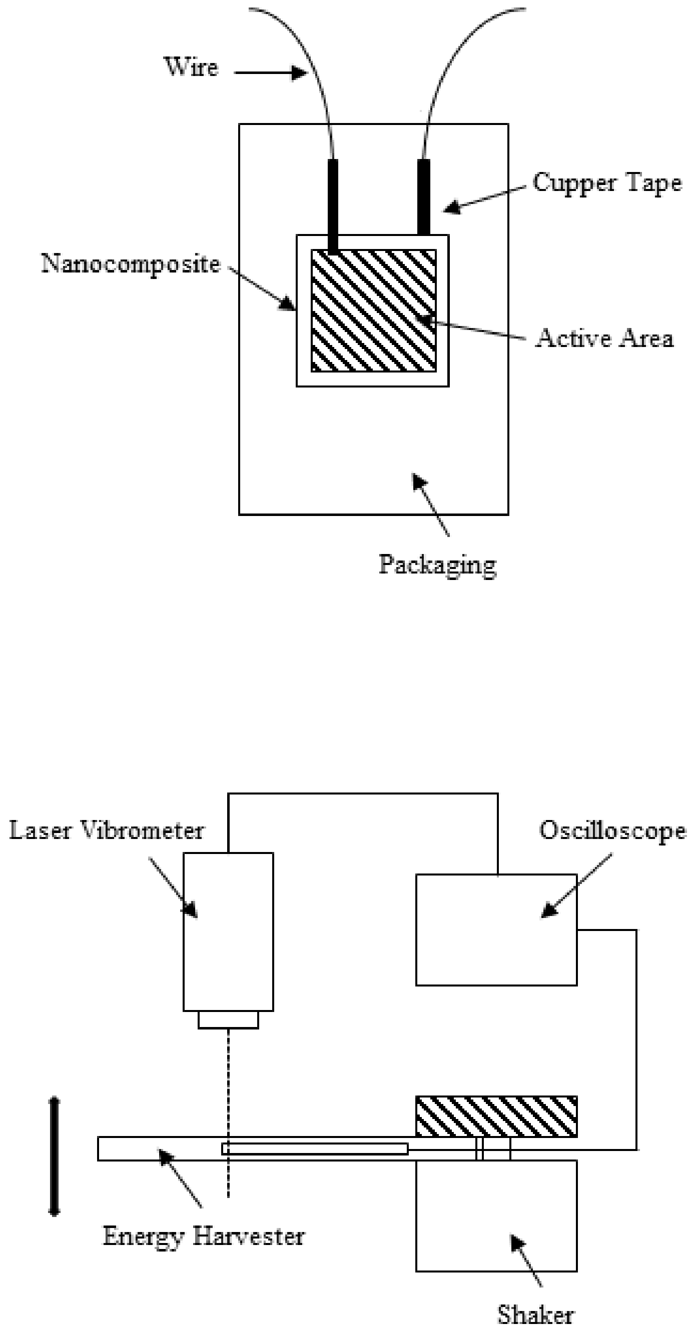
Wire
Cupper Tape
Nanocomposite
Active Area
Packaging
Laser Vibrometer
Oscilloscope
Energy Harvester
Shaker

Figure 9.3 (a) Structure of a cantilever type energy harvester with rGO/PVDF nanocomposite and (b) the voltage output measurement configuration

Before measuring the energy harvester, it is important to verify that the output voltage signal is contributed by the piezoelectric response rather than the cross talk of the electromagnetic interference (EMI), and the contact potential change.[142-144] Figure 9.4 shows the voltage output of an energy harvester with 1.5-rGO@200. The harvester is driven by finger tapping with the electromagnetic shaker being switched off. The open circuit voltage at both (a) forward and (b) reverse connection with the oscilloscope was measured. As polarity of the piezoelectric response is defined by that of the ferroelectric domain, an opposite polarity can be observed when switching the connection manner.[142] Thus, we define the upper side of the device after mounting on the shaker head as positive and the other as negative. As can be seen in Figure 9.4, the damping effect induces a free oscillation in the device, and a voltage output is captured with respect to this oscillation. The damping ratio of the device can be defined as the natural logarithm of the ratio of any two successive amplitudes in the free oscillations:

$$\delta = \ln(\frac{x_{n-1}}{x_n}) \cong 2\pi\varsigma \tag{9.4.1}$$

where δ is the logarithmic decrement, x is the amplitude and ς is the damping ratio, which was calculated to be 0.015 for the device under test.[145,146] An analogous damping phenomenon was also found in the voltage output, which can be directly associated to that of the free oscillation. This indicates that the voltage response is piezoelectric. More importantly, the polarity of output voltage signal is switchable by switching the polarity of the connection. As seen in Figure 9.4(a) and (b), under the same strain cycle, a downwards voltage peak was captured under an upward bending strain in the forward connection while the opposite manner is observed in the reverse connection. The contrasting output characteristics between forward and reverse connection can be associated to the polarity of the ferroelectric domain. Combining these evidences, the voltage output of the device can be predominantly attribute to the piezoelectric response of the nanocomposites.

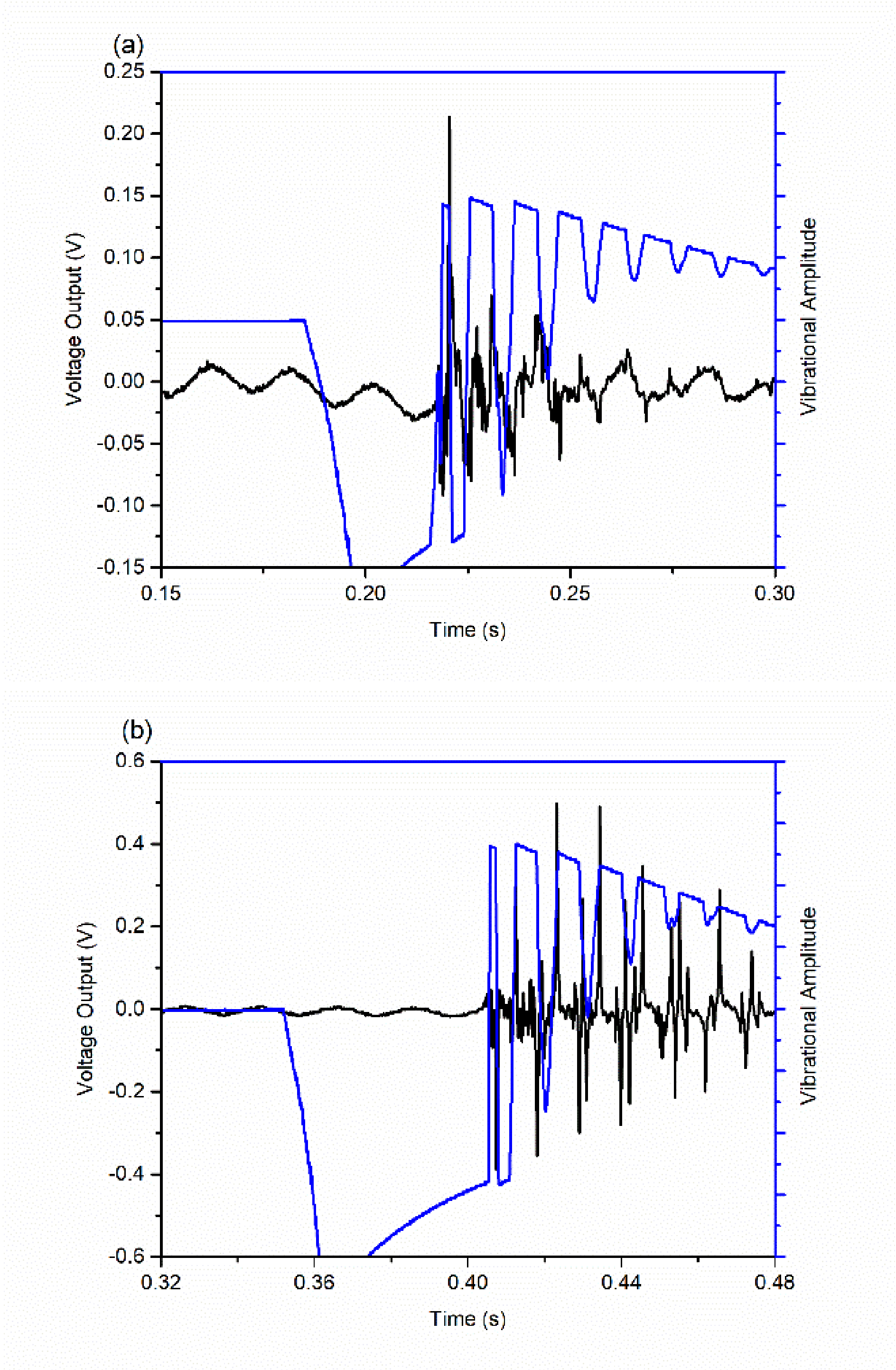

Figure 9.4 Voltage output of a single-end-clamped energy harvester driven by finger tapping under (a) forward connection and (b) reverse connection

The energy harvester is an electromechanical coupled device in which the mechanical energy should be efficiently delivered to the active piezoelectric component to maximize the voltage output. As a single-end-clamped cantilever energy harvester, the shape of the device can affect the output power.[143,147-149] It has been reported that by using a trapezoidal shape, the device performance can be improved.[147-149] In this research, we optimized the devices by reducing the cantilever free edge width. The results are shown in Figure 9.5. As seen, by reducing the width ratio of free-edge to clamped-edge from 1 to 0, the peak output voltage increases from 0.13V to 0.80V. This could be attributed to the nanocomposite being bended more efficiently. Therefore, the triangular cantilever was chosen as the optimized shape for devices fabricated in this research.

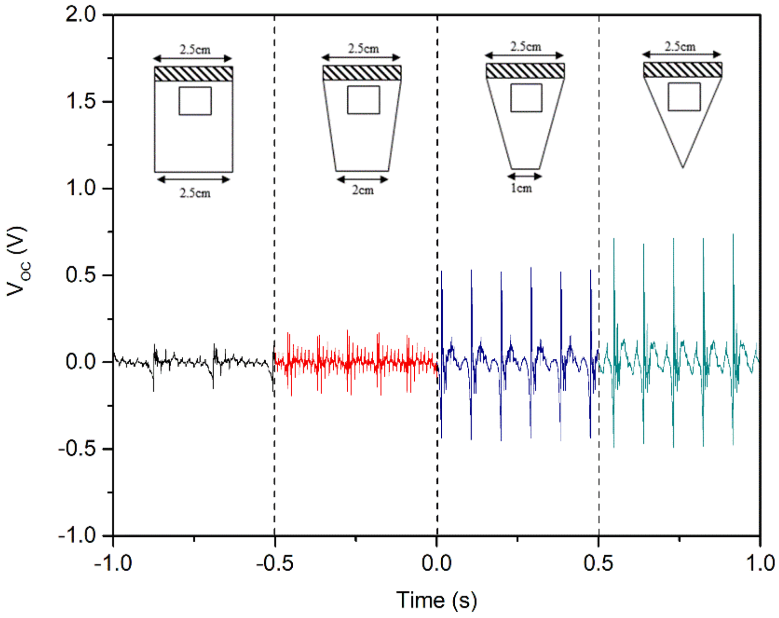

Figure 9.5 Relation between cantilever shape and the voltage output for the energy harvester with 1.5-rGO@200

9.5 Output Characteristics of the Energy Harvesters

To further increase the bending stress of the triangular cantilever energy harvester (TCEH), a hexagonal stainless-steel nut weighting 0.6 g with a diameter of 5 mm were fixed at the free edge as a load mass. Figure 9.6(a) shows the peak voltage output vs. load mass plots of the TCEH with 1.5-rGO@200 (simplified as 1.5-rGO-TCEH) driven by the electromagnetic shaker at 10 Hz. The peak open circuit voltage V_{OC} was 0.80 V without load mass, which was increased to 1.79 V with a load mass of 1.2 g. However, further increasing the load mass does not always increase the output voltage, as the V_{OC} dropped to 1.61 V at the load mass of 1.8g and further to 0.75 V at 2.4 g. Hence, the 1.2 g mass was applied to all other devices involved for further testing.

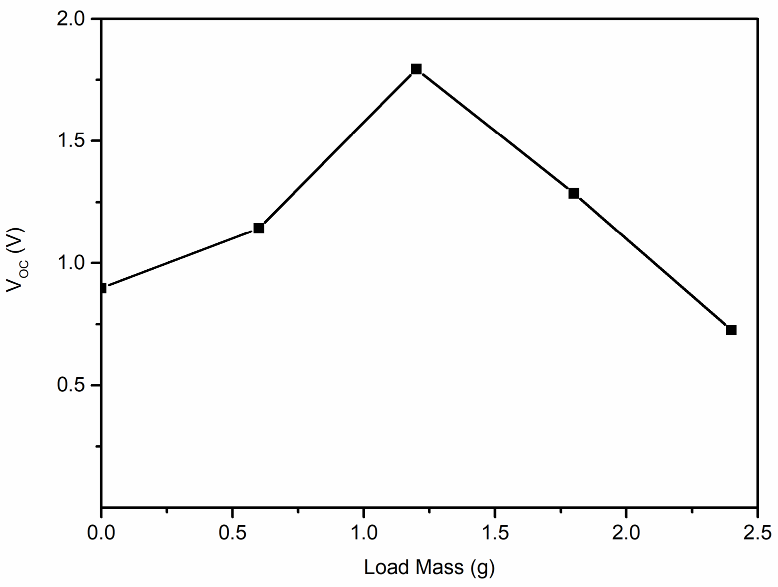

Figure 9.6 Open circuit voltage output vs. load mass for 1.5-rGO-TCEH

Table 9.5.1 shows output characteristics of the TCEHs assembled with nanocomposites of different rGO volume fraction. These devices were fabricated with the method state in section 9.4, with the dimension as shown in Figure 9.4.3. The devices were driven by the electromagnetic shaker at 10Hz with a 1.2 g mass fixed at the free end of the device. As seen, the V_{OC} of 1.0-rGO-TCEH is 2.357 V, which is the maximum value among the devices involved. This means that a higher rGO volume fraction does not lead to a higher V_{OC} to the device. As reported, the piezoelectric material is a capacitive voltage source, and the voltage across the capacitor geometry can be affected by its leakage behaviour.[139,144,150] It has been shown in the previous chapters that the reduced tunnelling distance with increasing rGO volume fraction introduces a higher leakage in high rGO content nanocomposites. This could be the reason for the decreased voltage output in high rGO content devices. The power output of these TCEHs have been measured with the existence of a resistive load. Three load resistors R_L with resistance of 10 kΩ, 100 kΩ, and 1MΩ were connected to the device, and the voltage across the R_L were captured. The output power P to the resistive load is calculated from:

$$P = \frac{V^2}{R_L} \tag{9.5.1}$$

For instance, the V_L across a 1MΩ resistor is 1.434 V for 1.0-rGO-TCEH and results is a power density of 0.182 mW/cm^3. The power output can be modified by the choice of R_L. According to the impedance matching theory, the output power maximizes when the R_L matches with the impedance of the device. For devices with rGO volume fraction between 1.0 vol.% and 2.0 vol.%, the maximum output power is observed when connected to a 1MΩ while that with 2.5 vol.% rGO is observed for a 100 kΩ load. This demonstrates the impact of load resistance on the power output. Meanwhile, we also measured the output energy density over a period of a voltage cycle. The energy density J per peak voltage circle can be defined as:

$$J = \int_{t_1}^{t_2} P(t)dt$$

where t_1 and t_2 are the start and end time of an individual voltage cycle respectively and P(t) is the instantaneous power density. As seen in Table 9.5.1, the maximum energy density was found to be 0.055 μJ/cm^3 for 1.0-rGO-TCEH when connected to a 1MΩ load. The energy output behaviour also indicates the internal screening effect. This appears as a decreased time span Δt per voltage cycle with increasing rGO volume fraction. The Δt was found to be 0.60ms, 0.40ms, 0.20ms, and 0.16ms for nanocomposite devices with 1.0 vol.%, 1.5 vol.%, 2.0 vol.% and 2.5 vol.% rGO, respectively. Both the power output and energy output show the impact of internal screening phenomena hindering the device performance. This effect is illustrated in Figure 9.5.2. The defects and impurities can be regarded as free charge carriers which are mobile in an electric field. A stress applied on the piezoelectric material can induce a dipole moment, and accordingly a built-in electric field is generated. This built-in electric field promotes the internal motion of free carriers, which neutralized the trapped charge. Hence, the effect of the strain induced dipole moment is screened, and the macroscopic behaviour observed is a short time span as well as a low peak voltage response. In terms of the device with high rGO volume fraction, the carrier travelling distance is sufficiently reduced. This may increase the screening rate and thus causes weaker output behaviour. These results reveal a paradox in the composite related energy harvester device. The output performance is strongly dependent on the quality of heterostructure of the inclusion/matrix interface, which highlights inclusions with superb conductance.[142] But a highly conductive inclusion in turn causes significant internal screening and results in high leakage. The effect needs to be addressed in the future works for composite related energy harvester devices.

Table 9.5.1 Output Characteristics of TCEHs assembled with pure PVDF and rGO/PVDF nanocomposites

Device	V_{OC} (V)	Load Resistance (Ω)	Peak Output Voltage (V)	Power Density (mW/cm^3)	Energy Density (μJ/cm^3)
1.0-rGO-TCEH	2.357	10k	0.035	0.011	0.003
		100k	0.403	0.141	0.042
		1M	1.434	0.182	0.055
1.5-rGO-TCEH	1.79	10k	0.025	0.005	0.001
		100k	0.246	0.054	0.011
		1M	1.154	0.117	0.024
2.0-rGO-TCEH	0.262	10k	0.018	0.003	0.0003
		100k	0.081	0.006	0.0006
		1M	0.393	0.014	0.0014
2.5-rGO-TCEH	0.178	10k	0.004	0.002	-
		100k	0.034	0.012	0.002
		1M	0.064	0.004	-

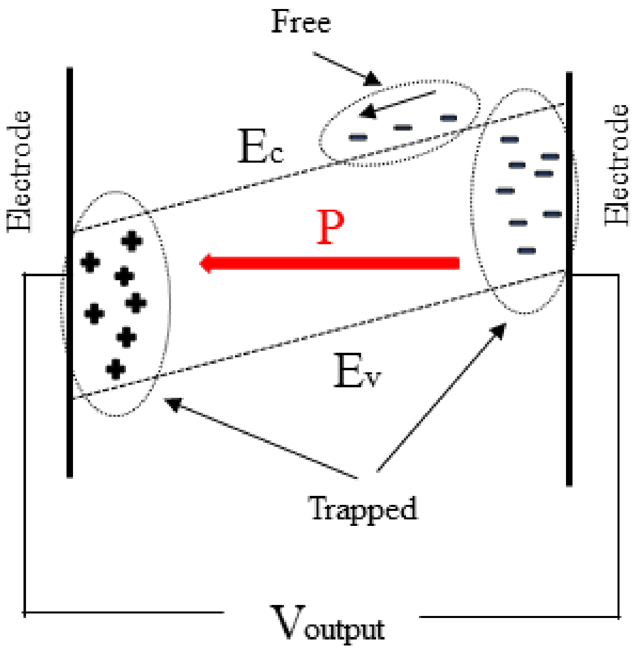

Figure 9.7 Illustration of the internal screening effect in a capacitive device.

9.6 Summary

In this chapter, we have evaluated the piezoelectric performance of the rGO/PVDF nanocomposites by incorporating them into both actuator and energy harvester devices. The findings in this chapter can be summarized as the follows:

(1) We have designed and tested a bi-clamped actuator with a 1.5-rGO@200, which exhibits a bimorph behaviour in contrast to the unimorph behaviour of that with a commercial PVDF film. This supports that the molecular dipole is symmetrical to the rGO plane forming micron bimorph structure. The major limitation of actuator devices based on self-polarized composites is that they are more vulnerable to the electric field compared to bulk materials. This limits the efforts of improving the actuating performance by increasing the rGO volume fraction.

(2) We have designed and tested a series of cantilever type energy harvesters with rGO/PVDF nanocomposites. We show the strategy of using a triangular device shape to enhance the output performance of the energy harvester device. A 1.0-rGO device can deliver a power density of 0.182 mW/cm^3 and energy density of 0.055 μJ/cm^3 to a 1MΩ load, which is the best among the devices fabricated. The nanocomposite devices are hindered by the internal screening effect induced by reduced carrier tunnelling distance at higher rGO volume fractions. This results in a decrease in both power and energy output in devices with high rGO volume fractions.

Chapter 10 Conclusion and future work

10.1 Conclusion

This project is a systematic study on the dielectric and piezoelectric properties of the rGO/PVDF nanocomposites, particularly, the effect of rGO/PVDF heterostructure on the device performances. These nanocomposites were fabricated via an in-situ thermal reduction method, with graphite-oxide (GO) particles as the starting inclusion material to avoid agglomeration. The GO particles were thermally reduced in-situ in the PVDF polymer to recover their electrical conductivity.

To start, an ideal conductor/insulator model was used to study the dielectric behaviour of the rGO/PVDF nanocomposites. This studied is based on the understanding that the inclusion particles can effectively expand the system electrode area of a composite. With the Schottky diode theory, we found the improved dielectric response in a composite over its matrix could be attributed to the formation of inclusion/matrix heterostructures providing more charge blocking sites. This explains why nano-sized, conductive inclusion particles can lead to a significant enhancement in the composite dielectric response. Besides, we also found a carrier recombination induced pseudo-leakage on charging a composite, which results in an exponentially decay in the capacitor energy efficiency. The possibility of carrier recombination increases in the same sense as the dielectric response, indicating that composites with large dielectric permittivity is more likely to exhibit a high leakage.

The model proposed in this research has been supported by the dielectric properties observed in the rGO/PVDF nanocomposites. To start, the addition of rGO improved the dielectric permittivity of the PVDF polymer. The maximum dielectric permittivity observed in this research is 380 (1 kHz) for 2.5-rGO@200, compared to that of 11 (1 kHz) for the pure PVDF. Simultaneously, the rGO particles were also well dispersed in the PVDF polymer. This is supported by the small value and weak dependence of the nanocomposite tanδ on the rGO content. As expected, nanocomposite with such a large dielectric permittivity failed to generate a large discharge energy density due to high leakage. The maximum discharge energy density for nanocomposite samples was merely 0.09 J/cm^3 (1.0-rGO@200, 30 MV/m, 10Hz), which is limited by their weak dielectric strength as well as small energy efficiency. By studying the charging characteristics of the samples, we demonstrated the predominant contribution of charge carrier recombination phenomena to the system leakage. We also showed the most efficient way to improve the nanocomposite discharge energy density is to increase the effective series resistance of the rGO/PVDF heterostructures. This was accomplished by utilizing the temperature tuneable nature of rGO. The energy efficiency for the 1.5-rGO@160 is 0.65 (50MV/m, 10Hz), resulting in a discharge energy density of 0.67 J/cm^3 that is 3 times that of the pure PVDF at the same condition. Furthermore, we established an explicit relation between dielectric permittivity and energy efficiency for PVDF composites. This relation can be used to evaluate the discharge energy density for PVDF composites, which fits well with the experimental data.

The structural change in the PVDF polymer induced by the addition of rGO particles was also studied. Comparison of the molecular and crystalline structure between pure PVDF and the rGO/PVDF nanocomposites was carried out by measuring their IR spectra and XRD patterns. Contrary to the predominant non-polar α phase structure observed in 200 °C annealed PVDF samples, up to 0.32 of the β phase was observed in the 200 °C reduced nanocomposites. We showed the as-cast PVDF and nanocomposites exhibit the same γ phase dominated structure, which may be attributed to the effect of polar DMF solvents. Variations start to emerge in samples annealed above melting temperature. This demonstrates that the β phase in the nanocomposites forms from a melting-recrystallization procedure, which is also accompanied by the removal of hydrophilic groups on rGO. Combining observation from the XRD and AFM/PFM, we show evidences of the β phase crystals grow on the surface of rGO and are covered by the α phase. The formation of the β phase is explained by an electrochemical interaction model. The rGO surface is charged due to Fermi level equalization with PVDF melt, which absorbs TTTT chains to construct the electrical double layer to screen the surface charge.

The β phase formation mechanism indicate that the rGO/PVDF nanocomposite reduced at 200°C is (i) piezoelectric and (ii) self-polarized, and electrochemical interaction between TTTT chains and the rGO particle may also suggest a mirrored molecular dipole by the rGO plane. Two types of piezoelectric devices, namely an actuator and a generator were fabricated with the 200°C reduced nanocomposites. The actuator device is designed in the way of a bi-clamped cantilever to evaluate the unique mirrored molecular dipole configuration. Compared to that assembled with a commercial PVDF film, the actuator with 1.5-rGO@200 exhibited a bimorph behaviour when switching the polarity of the wire connection. This supports the mirrored molecular dipole as suggested by the β phase formation mechanism. As for the generator, the maximum open circuit voltage was 2.357V for a device assembled with 1.0-rGO@200, with the maximum output power density and energy density of 0.182 mW/cm^3, and 0.055 μJ/cm^3, respectively, delivered to a 1MΩ load. Simultaneously, we showed that the addition of rGO accelerates the internal screening in the nanocomposite device. This is evidenced by the shorter time span per output cycle observed with increasing rGO volume fraction. The internal screening causes reduced power and energy output for devices with higher rGO volume fractions, which needs to be addressed for further optimizing the device energy harvesting performances.

10.2 Future work

Flexible, lightweight ferroelectric materials have a broad prospective in the next-generation electronic devices such as bendable screens, self-powered sensor networks, wearable equipment, and inflatable aerospace structures. In this research, we demonstrate that rGO/PVDF composites have the potential to be used in high power capacitor, sensor, and actuator applications.

In terms of the capacitors, we would suggest using nano-sized, semi-conductive inclusion particles as alternatives to the partially reduced rGO to increase the temperature stability of the composite dielectric behaviour. Meanwhile, it would also be a good option to use a high permittivity matrix material such as poly(vinylidene fluoride-co-hexafluoropropylene), and poly(vinylidene fluoride-trifluoroethylene-chlorofluoroethylene) to further improve the energy storage performance. In the device perspective, the nanocomposite films can be laminated to fabricate a multi-layer capacitor (MLCC) device. They can be a lightweight and more accessible alternative to the ferroelectric ceramics as the co-sintering is not needed in fabricating a nanocomposite MLCC.

In terms of the piezoelectric energy harvesters and actuators, the device structure optimization to increase the electro-mechanical coupling may overwhelm the effect of property-increase in the active materials. However, we still suggest an improved orientation of rGO particles to the electric field direction may improve the device piezoelectric response. This calls for more advanced processing routes to fabricate the rGO/PVDF nanocomposites.

Reference

[1] V. E. Henrich and P. A. Cox, *The surface science of metal oxides* (Cambridge university press, 1996).

[2] A. Mandelis and C. Christofides, *Physics, chemistry and technology of solid state gas sensor devices* (John Wiley & Sons, 1993), Vol. 174.

[3] L. H. Dawson, Physical Review **29**, 532 (1927).

[4] J. Curie and P. Curie, Journal de Physique Théorique et Appliquée **1**, 245 (1882).

[5] G. Lippmann, Journal de Physique Théorique et Appliquée **10**, 381 (1881).

[6] B. Jaffe, *Piezoelectric ceramics* (Elsevier, 2012), Vol. 3.

[7] Z. L. Wang, Journal of Physics: Condensed Matter **16**, R829 (2004).

[8] ANSI/IEEE Std 176-1987, 0_1 (1988).

[9] A. Erturk and D. J. Inman, in *Piezoelectric Energy Harvesting* (John Wiley & Sons, Ltd, 2011), pp. 343.

[10] S. E. Lyshevski, *Nano-and micro-electromechanical systems: fundamentals of nano-and microengineering* (CRC press, 2005), Vol. 8.

[11] M. R. Kermani, M. Moallem, and R. V. Patel, *Applied vibration suppression using piezoelectric materials* (Nova Publishers, 2008).

[12] A. A. Marino, *Modern bioelectricity* (CRC Press, 1988).

[13] M. E. Lines and A. M. Glass, *Principles and applications of ferroelectrics and related materials* (Oxford university press, 1977).

[14] M. Vijaya, *Piezoelectric materials and devices: Applications in engineering and medical sciences* (CRC Press, 2012).

[15] B. Wul and I. Goldman, Compt. rend. Acad. sci. URSS **46**, 139 (1945).

[16] G. Kwei, A. Lawson, S. Billinge, and S. Cheong, The Journal of Physical Chemistry **97**, 2368 (1993).

[17] R. V. Latham, British Journal of Applied Physics **18**, 1383 (1967).

[18] M. Stewart, M. Cain, and D. Hall, *Ferroelectric hysteresis measurement and analysis* (National Physical Laboratory Teddington, 1999).

[19] H. YAN, F. INAM, G. VIOLA, H. NING, H. ZHANG, Q. JIANG, T. ZENG, Z. GAO, and M. J. REECE, Journal of Advanced Dielectrics **01**, 107 (2011).

[20] J. F. Scott, Journal of Physics: Condensed Matter **20**, 021001 (2008).

[21] T. Wentink, L. J. Willwerth, and J. P. Phaneuf, Journal of Polymer Science **55**, 551 (1961).

[22] A. Liquori, in *Journal of Polymer Science: Polymer Symposia* (Wiley Online Library, 1966), pp. 209.

[23] G. Cortili and G. Zerbi, Spectrochimica Acta Part A: Molecular Spectroscopy **23**, 285 (1967).

[24] G. Cortili and G. Zerbi, Spectrochimica Acta Part A: Molecular Spectroscopy **23**, 2216 (1967).

[25] M. Li, H. J. Wondergem, M. J. Spijkman, K. Asadi, I. Katsouras, P. W. Blom, and D. M. de Leeuw, Nature materials **12**, 433 (2013).

[26] J. B. Lando, H. G. Olf, and A. Peterlin, Journal of Polymer Science Part A-1: Polymer Chemistry **4**, 941 (1966).

[27] R. Hasegawa, Y. Takahashi, Y. Chatani, and H. Tadokoro, Polym J **3**, 600 (1972).

[28] V. Ranjan, L. Yu, M. B. Nardelli, and J. Bernholc, Physical review letters **99**, 047801 (2007).

[29] M. A. Bachmann, W. L. Gordon, J. L. Koenig, and J. B. Lando, Journal of Applied Physics **50**, 6106 (1979).

[30] S. Weinhold, M. H. Litt, and J. B. Lando, Macromolecules **13**, 1178 (1980).

[31] Y. Takahashi and H. Tadokoro, Macromolecules **13**, 1317 (1980).

[32] K. Tashiro, M. Kobayashi, and H. Tadokoro, Macromolecules **14**, 1757 (1981).

[33] T. Furukawa, Phase Transitions **18**, 143 (1989).

[34] C.-h. Du, B.-K. Zhu, and Y.-Y. Xu, Journal of Applied Polymer Science **104**, 2254 (2007).

[35] Y. Wang, M. Cakmak, and J. L. White, Journal of applied polymer science **30**, 2615 (1985).

[36] G. T. Davis, J. E. McKinney, M. G. Broadhurst, and S. C. Roth, Journal of Applied Physics **49**, 4998 (1978).

[37] R. G. Kepler and R. A. Anderson, Journal of Applied Physics **49**, 1232 (1978).

[38] Y. Takahashi, Y. Nakagawa, H. Miyaji, and K. Asai, Journal of Polymer Science Part C: Polymer Letters **25**, 153 (1987).

[39] Y. Song, Y. Shen, H. Liu, Y. Lin, M. Li, and C.-W. Nan, Journal of Materials Chemistry **22**, 16491 (2012).

[40] L. Gao, J. He, J. Hu, and Y. Li, The Journal of Physical Chemistry C **118**, 831 (2014).

[41] D. Chun-gang, W. N. Mei, J. R. Hardy, S. Ducharme, C. Jaewu, and P. A. Dowben, EPL (Europhysics Letters) **61**, 81 (2003).

[42] Prateek, V. K. Thakur, and R. K. Gupta, Chemical reviews **116**, 4260 (2016).

[43] S. Maji, P. K. Sarkar, L. Aggarwal, S. K. Ghosh, D. Mandal, G. Sheet, and S. Acharya, Physical chemistry chemical physics : PCCP **17**, 8159 (2015).

[44] D. Shah, P. Maiti, E. Gunn, D. F. Schmidt, D. D. Jiang, C. A. Batt, and E. P. Giannelis, Advanced Materials **16**, 1173 (2004).

[45] A. Javadi, Y. Xiao, W. Xu, and S. Gong, Journal of Materials Chemistry **22**, 830 (2012).

[46] M. Li, C. Gao, H. Hu, and Z. Zhao, Carbon **65**, 371 (2013).

[47] Y. Mao, S. Mao, Z.-G. Ye, Z. Xie, and L. Zheng, Journal of Applied Physics **108**, 014102 (2010).

[48] K. Yang, X. Huang, Y. Huang, L. Xie, and P. Jiang, Chemistry of Materials **25**, 2327 (2013).

[49] H. Luo, D. Zhang, C. Jiang, X. Yuan, C. Chen, and K. Zhou, ACS Applied Materials & Interfaces **7**, 8061 (2015).

[50] N. Levi, R. Czerw, S. Xing, P. Iyer, and D. L. Carroll, Nano letters **4**, 1267 (2004).

[51] F. He, S. Lau, H. L. Chan, and J. Fan, Advanced Materials **21**, 710 (2009).

[52] R. K. Layek, S. Samanta, D. P. Chatterjee, and A. K. Nandi, Polymer **51**, 5846 (2010).

[53] D. Wang, Y. Bao, J. W. Zha, J. Zhao, Z. M. Dang, and G. H. Hu, ACS Appl Mater Interfaces **4**, 6273 (2012).

[54] K. Yang, X. Huang, L. Fang, J. He, and P. Jiang, Nanoscale **6**, 14740 (2014).

[55] J. I. Paredes, S. Villar-Rodil, A. Martínez-Alonso, and J. M. D. Tascón, Langmuir **24**, 10560 (2008).

[56] L. Cui, X. Lu, D. Chao, H. Liu, Y. Li, and C. Wang, physica status solidi (a) **208**, 459 (2011).

[57] H. Tang, G. J. Ehlert, Y. Lin, and H. A. Sodano, Nano letters **12**, 84 (2012).

[58] P. Arunachalam, in *Polymer-based Nanocomposites for Energy and Environmental Applications*, edited by M. M. Khan (Woodhead Publishing, 2018), pp. 185.

[59] K. Lichtenecker, Physikalische Zeitschrift **27**, 115 (1926).

[60] M. Garnet, Philos. Trans. R. Soc. London, Ser. A **205**, 237 (1906).

[61] T. C. Choy, *Effective medium theory: principles and applications* (Oxford University Press, 2015), Vol. 165.

[62] V. D. Bruggeman, Annalen der physik **416**, 636 (1935).

[63] T. J. Lewis, Dielectrics and Electrical Insulation, IEEE Transactions on **1**, 812 (1994).

[64] R. Armstrong and B. Horrocks, Solid State Ionics **94**, 181 (1997).

[65] T. Tanaka, M. Kozako, N. Fuse, and Y. Ohki, IEEE transactions on dielectrics and electrical insulation **12**, 669 (2005).

[66] J. I. Roscow, C. R. Bowen, and D. P. Almond, ACS Energy Letters **2**, 2264 (2017).

[67] P. Martins, C. M. Costa, M. Benelmekki, G. Botelho, and S. Lanceros-Mendez, CrystEngComm **14**, 2807 (2012).

[68] D. Mandal, K. J. Kim, and J. S. Lee, Langmuir : the ACS journal of surfaces and colloids **28**, 10310 (2012).

[69] M. M. Alam, A. Sultana, D. Sarkar, and D. Mandal, Nanotechnology **28**, 365401 (2017).

[70] R. Tian, Q. Xu, C. Lu, X. Duan, and R. G. Xiong, Chemical communications **53**, 7933 (2017).

[71] S. Yu, W. Zheng, W. Yu, Y. Zhang, Q. Jiang, and Z. Zhao, Macromolecules **42**, 8870 (2009).

[72] J. Wang, H. Li, J. Liu, Y. Duan, S. Jiang, and S. Yan, Journal of the American Chemical Society **125**, 1496 (2003).

[73] D. C. Bassett and A. Keller, Philosophical Magazine **6**, 345 (1961).

[74] D. C. Bassett, Philosophical Magazine **6**, 1053 (1961).

[75] N. Taniguchi and A. Kawaguchi, Macromolecules **38**, 4761 (2005).

[76] S. Manna and A. K. Nandi, The Journal of Physical Chemistry C **111**, 14670 (2007).

[77] K. Ke, P. Pötschke, D. Jehnichen, D. Fischer, and B. Voit, Polymer **55**, 611 (2014).

[78] M. J. Baker, C. S. Hughes, and K. A. Hollywood, in *Biophotonics: Vibrational Spectroscopic Diagnostics* (Morgan & Claypool Publishers, 2016), pp. 2.

[79] R. Proksch, Journal of Applied Physics **118**, 072011 (2015).

[80] A. Labuda and R. Proksch, Applied Physics Letters **106**, 253103 (2015).

[81] A. Di Bartolomeo, Physics Reports **606**, 1 (2016).

[82] E. Fermi, Rendiconti Lincei **145** (1926).

[83] P. A. M. Dirac, Proc. R. Soc. Lond. A **112**, 661 (1926).

[84] C. Kittel, *Introduction to solid state physics* (Wiley, 2005).

[85] R. T. Tung, Materials Science and Engineering: R: Reports **35**, 1 (2001).

[86] S. M. Sze and K. K. Ng, *Physics of semiconductor devices* (John wiley & sons, 2006).

[87] S. Grover and G. Moddel, IEEE Journal of Photovoltaics **1**, 78 (2011).

[88] M. Nagae, Japanese Journal of Applied Physics **11**, 1611 (1972).

[89] K. Szot, W. Speier, G. Bihlmayer, and R. Waser, Nature materials **5**, 312 (2006).

[90] J. Y. Li, C. Huang, and Q. Zhang, Applied Physics Letters **84**, 3124 (2004).

[91] J. Y. Li, L. Zhang, and S. Ducharme, Applied Physics Letters **90**, 132901 (2007).

[92] Z. M. Dang, J. K. Yuan, S. H. Yao, and R. J. Liao, Adv Mater **25**, 6334 (2013).

[93] H. Liu, Y. Shen, Y. Song, C. W. Nan, Y. Lin, and X. Yang, Adv Mater **23**, 5104 (2011).

[94] Z. M. Dang, L. Wang, Y. Yin, Q. Zhang, and Q. Q. Lei, Advanced Materials **19**, 852 (2007).

[95] H.-K. Jeong *et al.*, Journal of the American Chemical Society **130**, 1362 (2008).

[96] H.-K. Jeong, Y. P. Lee, M. H. Jin, E. S. Kim, J. J. Bae, and Y. H. Lee, Chemical Physics Letters **470**, 255 (2009).

[97] M. Acik, G. Lee, C. Mattevi, M. Chhowalla, K. Cho, and Y. J. Chabal, Nature materials **9**, 840 (2010).

[98] M. Acik, C. Mattevi, C. Gong, G. Lee, K. Cho, M. Chhowalla, and Y. J. Chabal, ACS Nano **4**, 5861 (2010).

[99] A. Bagri, C. Mattevi, M. Acik, Y. J. Chabal, M. Chhowalla, and V. B. Shenoy, Nature chemistry **2**, 581 (2010).

[100] C.-E. Cheng, C.-Y. Lin, C.-H. Shan, S.-Y. Tsai, K.-W. Lin, C.-S. Chang, and F. Shih-Sen Chien, Journal of Applied Physics **114**, 014503 (2013).

[101] C. Brabec, U. Scherf, and V. Dyakonov, *Organic photovoltaics: materials, device physics, and manufacturing technologies* (John Wiley & Sons, 2011).

[102] J.-H. Im, J. Chung, S.-J. Kim, and N.-G. Park, Nanoscale research letters **7**, 353 (2012).

[103] N. Jalali, PhD thesis, Queen Mary University of London, UK (2015)

[104] S. Kochowski and K. Nitsch, Thin Solid Films **415**, 133 (2002).

[105] S. H. Huh, *Thermal reduction of graphene oxide* (INTECH Open Access Publisher, 2011).

[106] O. C. Compton, B. Jain, D. A. Dikin, A. Abouimrane, K. Amine, and S. T. Nguyen, ACS Nano **5**, 4380 (2011).

[107] H. F. Liang, C. T. G. Smith, C. A. Mills, and S. R. P. Silva, J. Mater. Chem. C **3**, 12484 (2015).

[108] A. Mathkar, D. Tozier, P. Cox, P. Ong, C. Galande, K. Balakrishnan, A. Leela Mohana Reddy, and P. M. Ajayan, The journal of physical chemistry letters **3**, 986 (2012).

[109] L. Sygellou, G. Paterakis, C. Galiotis, and D. Tasis, The Journal of Physical Chemistry C **120**, 281 (2016).

[110] I. Jung, D. A. Dikin, R. D. Piner, and R. S. Ruoff, Nano letters **8**, 4283 (2008).

[111] Q. Zhang, H. Li, M. Poh, F. Xia, Z.-Y. Cheng, H. Xu, and C. Huang, Nature **419**, 284 (2002).

[112] L. Wang and Z.-M. Dang, Applied Physics Letters **87**, 042903 (2005).

[113] Q. Chen, P. Du, L. Jin, W. Weng, and G. Han, Applied Physics Letters **91**, 022912 (2007).

[114] C.-W. Nan, Progress in Materials Science **37**, 1 (1993).

[115] V. Ranjan, M. B. Nardelli, and J. Bernholc, Physical review letters **108**, 087802 (2012).

[116] D. Mandal, K. Henkel, and D. Schmeisser, The Journal of Physical Chemistry B **115**, 10567 (2011).

[117] J. C. Li, C. L. Wang, W. L. Zhong, P. L. Zhang, Q. H. Wang, and J. F. Webb, Applied Physics Letters **81**, 2223 (2002).

[118] S. Weinhold, M. Litt, and J. Lando, Macromolecules **13**, 1178 (1980).

[119] M. Kobayashi, K. Tashiro, and H. Tadokoro, Macromolecules **8**, 158 (1975).

[120] K. Tashiro, H. Tadokoro, and M. Kobayashi, Ferroelectrics **32**, 167 (1981).

[121] L. Ruan, X. Yao, Y. Chang, L. Zhou, G. Qin, and X. Zhang, Polymers **10**, 228 (2018).

[122] P. Martins, A. C. Lopes, and S. Lanceros-Mendez, Progress in Polymer Science **39**, 683 (2014).

[123] J. Gregorio, Rinaldo and M. Cestari, Journal of Polymer Science Part B: Polymer Physics **32**, 859 (1994).

[124] R. Gregorio, Journal of Applied Polymer Science **100**, 3272 (2006).

[125] R. Imamura, A. Silva, and R. Gregorio Jr, Journal of applied polymer science **110**, 3242 (2008).

[126] A. J. Lovinger, D. D. Davis, R. E. Cais, and J. M. Kometani, Macromolecules **19**, 1491 (1986).

[127] M. Li, I. Katsouras, C. Piliego, G. Glasser, I. Lieberwirth, P. W. M. Blom, and D. M. de Leeuw, Journal of Materials Chemistry C **1**, 7695 (2013).

[128] Y. Takahashi, Y. Nakagawa, H. Miyaji, and K. Asai, Journal of Polymer Science Part C: Polymer Letters **25**, 153 (1987).

[129] C. L. Liang, Z. H. Mai, Q. Xie, R. Y. Bao, W. Yang, B. H. Xie, and M. B. Yang, The journal of physical chemistry. B **118**, 9104 (2014).

[130] A. Keller, Philosophical Magazine **2**, 1171 (1957).

[131] D. Turnbull, The Journal of Chemical Physics **20**, 411 (1952).

[132] K. F. Kelton, in *Solid State Physics*, edited by H. Ehrenreich, and D. Turnbull (Academic Press, 1991), pp. 75.

[133] D. Turnbull, The Journal of Chemical Physics **18**, 198 (1950).

[134] R. F. Tournier, Physica B: Condensed Matter **392**, 79 (2007).

[135] R. Tournier, (Iron Steel Institute Japan, 2006).

[136] R. F. Tournier, Science and technology of advanced materials **10**, 014607 (2009).

[137] T. Jordan, N. Ounaies, ICASE Report No. 2001-28.

[138] K. I. Park *et al.*, Adv Mater **24**, 2999 (2012).

[139] J. Briscoe, M. Stewart, M. Vopson, M. Cain, P. M. Weaver, and S. Dunn, Advanced Energy Materials **2**, 1261 (2012).

[140] C. K. Jeong, K.-I. Park, J. Ryu, G.-T. Hwang, and K. J. Lee, Advanced Functional Materials **24**, 2620 (2014).

[141] S. Lee *et al.*, Advanced Functional Materials **23**, 2445 (2013).

[142] R. Yang, Y. Qin, C. Li, L. Dai, and Z. L. Wang, Applied Physics Letters **94**, 022905 (2009).

[143] C. R. Bowen, H. A. Kim, P. M. Weaver, and S. Dunn, Energy & Environmental Science **7**, 25 (2014).

[144] N. Jalali, P. Woolliams, M. Stewart, P. M. Weaver, M. G. Cain, S. Dunn, and J. Briscoe, Journal of Materials Chemistry A **2**, 10945 (2014).

[145] X. Chen, S. Xu, N. Yao, and Y. Shi, Nano letters **10**, 2133 (2010).

[146] J. Park, M. Kim, Y. Lee, H. S. Lee, and H. Ko, Science advances **1**, e1500661 (2015).

[147] M. I. Friswell and S. Adhikari, Journal of Applied Physics **108**, 014901 (2010).

[148] J. M. Dietl and E. Garcia, Journal of Intelligent Material Systems and Structures **21**, 633 (2010).

[149] D. Benasciutti, L. Moro, S. Zelenika, and E. Brusa, Microsystem Technologies **16**, 657 (2009).

[150] J. Liu, P. Fei, J. Song, X. Wang, C. Lao, R. Tummala, and Z. L. Wang, Nano letters **8**, 328 (2008).

Publications

Y Zhang, Y Wang, TW Button, Local Polarization Transits Polar Molecular Chain in rGO/PVDF Nanocomposite for High Power Density Nanogenerator, to be submitted

Y Zhang, TW Button, Origin of Leakage for High Dielectric Permittivity Composite Capacitors, to be submitted

Y Zhang, Y Wang, S Qi, S Dunn, H Dong, TW Button, Enhanced Discharge Energy Density in the rGO/PVDF Nanocomposites: the Role of Heterointerface, *Applied Physics Letters* 112, 202904, 2018

Y Jiang, Z Qiu, R McPhillips, C Meggs, S Mahboob, H Wang, R Duncan, D Rodriguez-Sanmartin, **Y Zhang**, G Schiavone, R Eisma, M Desmulliez, S Eljamel, S Cochran, TW Button, C Demore, *IEEE Transactions of Ultrasonics, Ferroelectrics and Frequency Control* 63 (2), 2016

L Luo, C Chen, H Luo, **Y Zhang**, K Zhou, D Zhang, The Effects of Precursors on the Morphology and Microstructure of Potassium Sodium Niobate Nanorods Synthesized by Molten Salt Synthesis, *CrystEngComm* 17, 8710-8719, 2015

Y Zhang, Y Jiang, X Lin, R Xie, K Zhou, TW Button, D Zhang, Fine-Scaled Piezoelectric Ceramic/Polymer 2-2 Composites for High-Frequency Transducer, *Journal of the American Ceramic Society* 97 (4), 1060-1064, 2014